CONTROLLING SEMICONDUCTOR NANOWIRE CRYSTAL STRUCTURES VIA SURFACE CHEMISTRY

A Dissertation
Presented to
The Academic Faculty

by

Nae Chul Shin

In Partial Fulfillment
of the Requirements for the Degree
Doctor of Philosophy in the
School of Chemical & Biomolecular Engineering

Georgia Institute of Technology
December 2013

CONTROLLING SEMICONDUCTOR NANOWIRE CRYSTAL STRUCTURES VIA SURFACE CHEMISTRY

Approved by:

Dr. Michael A. Filler, Advisor
School of Chemical & Biomolecular Engineering
Georgia Institute of Technology

Dr. Dennis W. Hess
School of Chemical & Biomolecular Engineering
Georgia Institute of Technology

Dr. Christopher W. Jones
School of Chemical & Biomolecular Engineering
Georgia Institute of Technology

Dr. Mei-Yin Chou
School of Physics
Georgia Institute of Technology

Dr. Kenneth Brown
School of Chemistry and Biochemistry
Georgia Institute of Technology

Date Approved: October 24th, 2013

To my parents,

ACKNOWLEDGEMENTS

First, I would like to thank my advisor, Dr. Michael Filler, for his steady and persistent support and guidance over last 5 years. He always has been my role model as a scientist and researcher. I also want to thank to my PhD thesis committee members: Dr. Kenneth Brown, Dr. Mei-Yin Chou, Dr. Dennis W. Hess, and Dr. Christopher W. Jones for their helpful comments on my thesis.

Thanks to Dr. Miaofang Chi, and Dr. Jane Y. Howe at ShaRE facility in Oak Ridge National Laboratory, for their help on TEM instrument and Dr. Ye Xu at Louisiana State University, for valuable discussions. I also would like to thank the current and former Filler group members: Dr. Li-Wei Chou, Ildar Musin, Saujan Sivaram, Florencia Rusli, Ho Yee Hui, and Dmitriy Boyuk, for their help in researches.

I want to thank all the people and friends whom I met in Atlanta, Jason Bentley, Sung Gu Kang and Sonam Sherpa, for helping and sharing good times as classmates. I am also thankful to the former and current members of Korean ChBE Association of Georgia Tech including Jeong Woo Han, Kwanghun Chung, Hyea Kim, Hyewon Lee, Kyung Hee Oh, and the members of Sugarloaf Korean Baptist Church, and also to my friends in Korea: Youngjin Jang and Hyeyun Jung.

I am grateful to my parents for their endless supports and prayers. Without them, I could not have made my life here. Finally, I would like to thank God for letting me start and continue my PhD research, under His guidance.

TABLE OF CONTENTS

Page

LIST OF TABLES

LIST OF FIGURES

SUMMARY

Semiconductor nanowires are a promising building block for various applications in optics, electronics, or thermoelectrics, due to their controllable properties via structure engineering. In spite of the successful demonstrations of controlling semiconductor nanowire structures (e.g. multiply kinking superstructure or twinning superlattice) over past decade, fundamental understanding of mechanisms during the nanowire growth has remained unclear. In the vapor-liquid-solid (VLS) growth method using vapor phase chemical molecules as the reaction sources, it is expected that the role of surface chemistry is important for the overall nanowire growth behavior.

In this thesis, we suggest a new route to control the structure of semiconductor nanowires using surface chemistry. Specifically, in Au-catalyzed Si nanowire growth using hydride species (Si_2H_6) as growth precursors, we measure that the surface hydrogen existing on the nanowires sidewalls affects the growth morphology actively. Firstly, we show the spectroscopic evidence of atomic hydrogen bonded to sidewall surface of Si nanowires in real-time during growth and correlate their relative change with different growth orientations. By introducing additional atomic hydrogen during the <111>-oriented nanowire growth with intrinsically low hydrogen concentration, we observe that the growth orientation changes to <112> orientation due to the surface hydrogen increase.

We also show that the transient change in the nanowire growth conditions can rationally induce the planar defects in Si nanowires. We modify the growth temperature and pressure for short amount of time to induce the significant change in the surface hydrogen, and confirm transverse twin boundaries or angled stacking faults nucleate

when the growth conditions change. This result suggests the rational introduction of planar defects is possible in user-programmable manner, and the possibility of engineering defect superstructure in Si nanowires.

We also demonstrate the formation of multiple, consecutive transverse twin boundaries (TBs) in <111> oriented Si nanowires. The spacing between each TB is governed by the diameter-dependent sidewall facet morphology. This result suggest that the fabrication of defect superstructures (i.e. twinning superlattice) which is frequently observed in group III-V nanowire system is also possible in group IV nanowires.

Finally, we combine real-time *in situ* infrared spectroscopy with high-resolution electron microscopy to show the critical role of surface hydrogen and twin boundary (TB) propagation during the <111>/<112> kinking of Si nanowires. We also identify the mechanism by which high fidelity superstructures are possible. In particular, the presence of a continuous TB at <112> → <112> kinks, and the pinning of the nucleation site that likely accompanies it, reduces the number of degenerate directions available to the nanowire. Our findings provide important insight into the vapor-liquid-solid technique and identify new possibilities for systematically controlling nanowire kinking.

Overall, this thesis highlights the crucial role of surface hydrogen impacting VLS Si nanowire growth and suggests a new route to control nanowire structures using surface chemistry in general.

CHAPTER 1

INTRODUCTION

Recent advances in nanotechnology have demonstrated numerous applications of manipulating material properties via nanoscale structure control. Especially in 1-dimensional (1D) nanowire systems, scientists and engineers have achieved a high degree of ability to control the shape, crystal phase, and compositions over the last decade. Notably, designing structures of nanowires is directly related to the manipulation of physical properties for various applications such as optoelectronics,[1, 2] light absorption,[3, 4] and thermoelectric devices.[5, 6] Due to this clear dependence of properties on the nanowire structures, various researches have been seeking to control these structures during synthesis, and several promising results showing rational controls are available in the literature.[7-10]

1.1. Semiconductor Nanowire Growth

In the 1960s, Wagner and Ellis showed that 1D structures of Si crystals can be synthesized from a vapor phase source using metal impurity as the catalyst,[11] and this method has been named vapor-liquid-solid (VLS) growth. A schematic illustration of the VLS growth process is shown in Figure 1.1. In this growth mechanism, the vapor phase precursor molecules such as hydride (e.g. SiH_4 or Si_2H_6) or chloride (e.g. $SiCl_4$) are used as the source of growth. They are transferred to the substrate surface where the metal catalysts (e.g. Au or Al) exist and decompose. Continuous supply of vapor phase precursor molecules induces the supersaturation of the catalyst, and nucleation of the crystal phase occurs at the interface between the solid substrate and liquid alloy. Once the nucleation occurs, the bilayer addition process is continued from the nucleation point along the interface between the catalytic alloy and the solid-phase. As long as the catalyst droplet is maintained in supersaturation state by the introduction of precursor molecules to form the nucleus, the growth continues such that a nanowire grows out from the substrate. Therefore, nanowire growth is a non-equilibrium process dependent on the precursor molecule transport and catalytic activity of the alloy droplet.

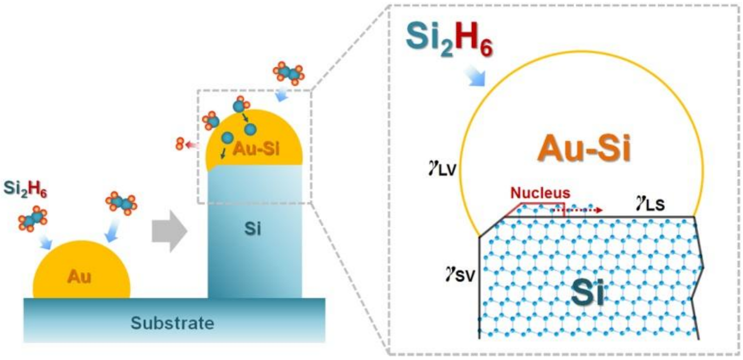

Figure 1.1: A schematic illustration of VLS growth mechanism of Si nanowire.

Gold is the most popular metal in VLS growth of Si nanowires because it is generally known that it forms a deep eutectic with Si[12] in the phase diagram. Although the melting points of pure Au and Si are 1064 °C and 1410 °C each, once they are at eutectic composition, the Au-Si alloy melts at 363 °C with 19 % of atomic composition of Si. This enables the epitaxial growth of nanowires at relatively low temperature conditions with hydride precursors.

Since the nanowire growth can be continued as long as the alloy droplet maintains its catalytic activity in the VLS method, the length of nanowires can be modulated by changing growth time.[13] Also the axial growth rate can be varied according to the change in the process pressure, temperature, catalyst size, and the density of nanowires on the substrate.[14-17]

1.2. Common Observations in Nanowire Growth

Various interesting phenomena have been observed from semiconductor nanowire growth catalyzed by Au. Since the nanowire growth is dominated by the kinetics at the triple-phase line (TPL) of the Au catalyst and nanowire sidewall facet near the growth front, the overall morphology and crystal structure of nanowires are determined at this region.

There have been several reports about the diameter-dependent growth rate of semiconductor nanowires.[15, 18-21] In a range of growth conditions, nanowires with smaller diameter ($\leq$ 50 nm) have exhibited relatively slower growth rates than larger nanowires (> 100nm) and this phenomenon has been considered due to the Gibbs-Thompson effect,[12, 22] in which the supersaturation of catalyst droplet directly affects the growth rate.[23] However, several results showing different growth behavior also have been reported in other systems. Especially when the precursor (SiH_4 or Si_2H_6) pressures are sufficiently low such that the Au catalyst can diffuse onto the nanowire surface, the diameter-independent growth rate is observed.[16] In addition, when the influx of Si precursor to the catalyst is rapid such that the supersaturation leading to the lift-off of the droplet (thus, the growth of nanowire) occurs early, reversed growth rate, where smaller diameter nanowires show higher growth rate, has been reported.[24] Despite this inconsistency in the observations on growth rate which is system specific, traditional models for the nanowire growth have emphasized the change in the supersaturation of catalyst droplet,[25] without considering the surface energy change in the solid-vapor interface facets.

A nanowire is composed of sidewall facets with multiple orientations, and for single crystalline nanowires, the orientations of sidewall facets are different depending on the growth orientations.[15] For example, <111> oriented Si nanowires generally show {112} sidewalls which are sub-faceted into {111} and {113} planes.[26] However, when nanowires grow along <112> orientation, {111}, {113}, and {110} surfaces compose the sidewall facets[27] and <110> oriented nanowires exhibit {111} and {110} sidewall facets. Under specific growth conditions, nanowires tend to have the lowest-free-energy configuration at certain diameters, which determines the sidewall facet orientations. Experimental observations over the last decade have suggested that there is a relationship between the nanowire diameter and particular growth orientations.[28, 29] As nanowire diameter decreases, the sidewall facets with lower energy are favored, resulting in specific growth directions depending on the diameter. For example, as demonstrated by Wu *et al*,[19] a majority of nanowires with sub 10 nm diameters grow in <110> directions, whereas those with diameters between 10 and 20 nm are oriented in <112> directions. Therefore, this difference in growth directions is explained by the difference in the sidewall surface energy. For the Si crystal system, the surface energies are different between each facet orientation,[30-32] as shown in Table 1.1.

Table 1.1: Surface energies of major (*hkl*) facets of Si.[30] Copyright 1993 by The American Physical Society.

Facet	Energy (J m^{-2})
(111)	1.23
(100)	1.36
(311)	1.38
(110)	1.43

As mentioned above, since the nanowire growth is continued from the bilayer addition process at TPL, microscopic observations at the growth front of nanowires have provided some insights on growth kinetics. Recently, with the aid of *in situ* transmission electron microscopy (TEM), several research groups have observed the periodic change in the growth front facet morphology by forming a truncated facet at the edge of TPL.[33-35] In this process, the truncated facets exhibit oscillatory behavior synchronized with the step flows[36] of bilayer addition, as shown in Figure 1.2. These findings indicate the growth kinetics must be considered by the balance between the cyclic change of chemical potential in the catalyst droplet and the surface tension of droplet, and also importantly, the newly formed facets' surface energy.

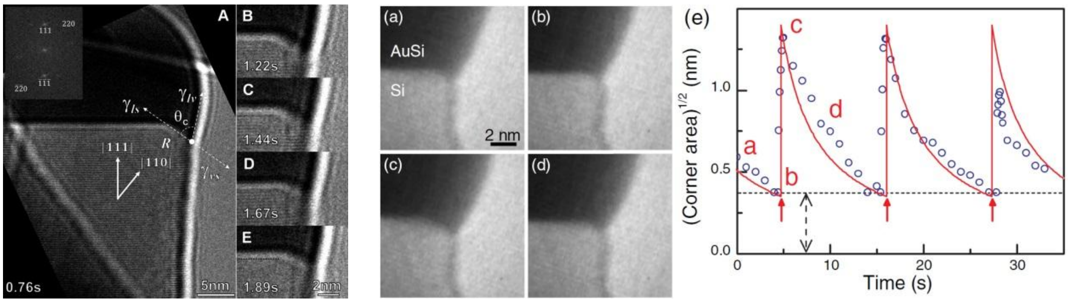

(a) (b)

Figure 1.2: *In situ* bright-field TEM observations of truncated facets formation at the edge of TPL measured from (a) Ge[34] and (b) Si nanowire.[35] (a) Reprinted with permission from Gamalski *et al.*[34] Copyright 2011 American Chemical Society. (b) Copyright 2011 by The American Physical Society.

Another common observation in the semiconductor nanowire system is growth orientation change, which is called kinking.[37-41] This is distinct behavior from the diameter-dependent growth orientations mentioned above, because kinking is a kinetically induced process. Madras *et al.* reported that Au catalyzed Si <111> nanowires can kink into <112> as temperature decreases from 500 °C to 400 °C, or pressure increases from 0.2 mTorr to 0.7 mTorr.[37] This kinking is related to the state of the sidewall surface. Since Au atoms are mobile and readily diffuse on the {112} surface of the Si lattice in the temperature range of VLS growth,[42, 43] <111> nanowires vertically grown from Si (111) substrate exhibits {112} sidewalls decorated with Au atoms diffused from the catalyst at the top. However, when the nanowire kinks to <112> orientation, it has been confirmed that the degree of wetting of Au on nanowire sidewalls is reduced.[44, 45] The change in the Au mobility on the nanowire sidewalls has been thought of as related to the pressure of precursor molecules. Nevertheless, the fundamental understanding in regard to the chemical species from the precursor decomposition which can affect the Au wetting behavior on the nanowire sidewalls has remained unclear.

Recently, Dayeh *et al.* showed that the similar <112> kinking of the Si segment grown from <111> oriented Ge nanowire in Si/Ge heterostructure, and found that there exist {111} planar defects parallel to the <112> kinking orientation.[39] Actually, this morphology of planar defects propagating parallel to the <112> growth orientation has been generally observed from nanowires with various material systems,[46-51] as shown in Figure 1.3. Although defect formation has been interpreted as due to the change in the supersaturation of the catalyst droplet, because of the experimental challenge in measurement,[52] the details of nanowire growth mechanisms with the existence of planar defects have remained elusive.

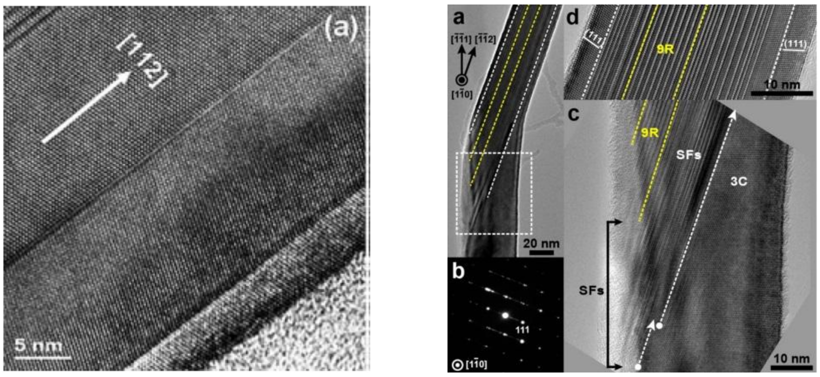

(a) (b)

Figure 1.3: TEM images showing <112> oriented (a) Si[48] and (b) Ge[51] nanowires with parallel planar defects. (a), adapted from Su *et al.*[48] with permission from The Royal Society of Chemistry. (b) Reprinted with permission from Jeon et al.[51] Copyright 2013 American Chemical Society.

1.3. Structure Engineering of Semiconductor Nanowires

In parallel with the advances in elucidation of the growth mechanism, there have been various attempts to control the morphology and crystal structure of nanowires.

First, by modulating the growth conditions, kinking superstructures of Si nanowire composed of multiple segments have been fabricated.[53] Using this knowledge, the same research group has demonstrated the applications of this structure in three-dimensional (3D) bioprobes.[54-56] Several other approaches have been employed to achieve similar kinking superstructures by using shape guided method[57], selective chemical etching,[58] or surface chemisty[40]. Nevertheless, it still remains challenging to achieve well-defined multiple kinking superstructures in a controllable manner.

Phase engineering of zinc blende (ZB)/ wurtzite (WZ) crystals[59] or defect superstructures composed of periodically spaced multiple transverse planar defects[7, 9] have also drawn the attention of nanowire researchers. Since physical properties such as band structures are affected by the crystal phase/structure, having control over planar defect formation in nanowires promises opportunities to tune their optical and electronic properties.[60] Interestingly, this defect engineering is more frequently demonstrated in III-V nanowire systems (e.g. InP, InAs, GaP, GaAS, etc) rather than group IV (Si or Ge) nanowires where few studies have demonstrated a limited range of defect engineering.[47, 61, 62] A few examples of nanowire superstructures obtained from these structure engineering approaches are shown in Figure 1.4.

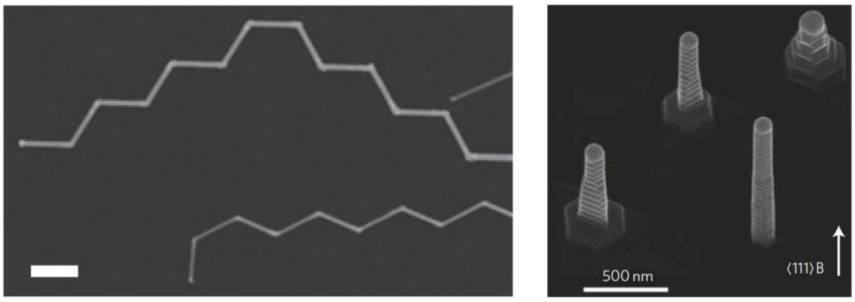

(a) (b)

Figure 1.4: Examples of structure engineering of nanowires. (a) Kinking superstructures composed of multiple Si <112> oriented segments.[53] (b) InAs nanowires exhibiting twinning superlattice.[9] (a) Adapted by permission from Macmillan Publishers Ltd: *Nat. Nanotechnol.* Tian *et al*,[53] copyright 2009. (b) Adapted by permission from Macmillan Publishers Ltd: *Nat. Nanotechnol*. Caroff *et al*,[9] copyright 2008.

Another example of nanowire structure engineering is controlling the lateral dimensions (i.e. diameter modulation). When the diameter varies in a nanowire, one can expect the enhancement of light absorption[63] or thermoelectric conversion efficiency.[64] This change in the nanowire diameter has been observed for a variety of material systems (e.g., Ge, GaN, InP, Si/GaP), mostly by changing the volume of catalyst via empirical control of growth parameters.[10, 65-67]

In overall, various attempts to control the structure of nanowires have shown successful demonstrations. Nonetheless, fundamental understanding of the process inducing the structural change regarding surface chemistry has remained unclear. Therefore, it necessitates again understanding the role of surface chemistry on nanowire growth to achieve systematic control, especially in chemical precursor-based growth.

1.4. Energetic Significance of Chemical Surface Termination

In colloidal nanocrystal systems, the crystal growth is significantly affected by the change of interface energy, which is kinetically controlled by selective adhesion of surfactant molecules on particular facets.[68] Anisotropic rod-shaped nanocrystals can be synthesized by the attachment of organic surfactant molecules to one facet,[69] or even complex shapes can be prepared by controlling relative growth rates of crystal facets with different surface energy.[70, 71] These examples substantiate the role of surface chemistry on crystal growth via termination of exposed facets. Surface functionalization of the crystal surface by vapor phase molecules under a vacuum environment also has been studied extensively.[72, 73] Experimental demonstrations of various types of molecules adsorbed on the semiconductor crystal surfaces in vacuum suggest that it is also possible to control the structure via selective facet passivation in vapor phase reaction.[74-76]

Turning attention to nanowire growth using the VLS method, it is noted that the hydride precursor molecules (i.e. SiH_4, Si_2H_6) decompose to produce atomic hydrogen. In the traditional growth model, hydrogen atoms are considered to desorb from the surface of the catalyst once the precursor molecules are decomposed.[77, 78] However, surface studies on hydrogen desorption kinetics from various substrate surfaces[79, 80] suggest that desorption of hydrogen occurs at generally higher temperatures than the actual growth range in the VLS process. This is important since hydrogen desorption is the rate limiting step of 2-dimensional film growth of Si.[81, 82] Therefore, the role of surface hydrogen on the nanowire sidewalls cannot be underestimated and the new approach considering surface chemistry as the energetic variable of VLS nanowire growth is needed.

1.5. Objectives of this Thesis

The objective of this thesis is to suggest a new route to control semiconductor nanowire structure using surface chemistry. Specifically, hydrogen produced from the decomposition of Si_2H_6 is considered to impact the growth kinetics of VLS-grown Si nanowires. As shown in the previous sections, we expect the surface energy change via chemical bonding formation between atomic hydrogen and surface Si atoms is sufficiently significant to impact the growth morphology. To this end, this thesis provides evidence of (1) atomic hydrogen existing on the sidewall surface of nanowires during VLS growth; (2) the active role of extrinsic hydrogen inducing changes in growth kinetics; (3) morphological change of nanowires (i.e., growth orientation change and planar defect formation) according to the difference in the surface hydrogen amount.

Since hydrogen atoms existing on Si surface are relatively short-lived and unstable, their measurement must be achieved in an ultra-high vacuum environment. Notably, conventional structural analysis employing the *in situ* TEM technique is not appropriate for the detection of “light” hydrogen atoms on surface. Therefore, we employ *in situ* IR spectroscopy to detect hydrogen bonding on Si surface. By performing the measurement in real-time, we confirm the increase of surface hydrogen on the sidewall surface during nanowire growth.

The correlation between surface hydrogen coverage and observed morphology change in nanowire growth orientation strongly suggests the active role of hydrogen on the growth kinetics. We developed the method to introduce additional hydrogen to impact the amount of surface hydrogen at the given condition extrinsically, and confirmed the evidence that hydrogen can induce change in the nanowire growth orientation (i.e. kinking).

Changes in the surface hydrogen amount induce the generation of planar defects in nanowires as well as kinking. Since nanowire growth is continued via a bilayer addition process initiated near the sidewall surface, changing the surface hydrogen amount can cause fault stacking at the growth front. We show the correlation between the growth condition change and planar defects positions, and suggest a new approach to engineer the defect superstructure in semiconductor nanowire.

We also find the relationship between surface hydrogen and defect propagation in Si nanowire kinking superstructures. By combining real-time *in situ* infrared spectroscopy with high-resolution electron microscopy, we observe the critical role of surface hydrogen and twin boundary (TB) propagation during the <111>/<112> kinking of Si nanowires. Our findings provide important insight into the vapor-liquid-solid technique and identify new possibilities for systematically controlling nanowire kinking.

1.6. Thesis Outline

Experimental details of the system used in this thesis are presented in Chapter 2. A custom-built ultra-high vacuum (UHV) chamber equipped with an *in situ* Fourier Transform Infrared (FTIR) spectrometer is used for the growth of Si nanowires coupled with the surface chemistry measurement.

In Chapter 3, the results of real-time *in situ* IR spectroscopic measurement on the surface hydrogen of Si nanowire sidewalls grown at different temperature and pressure conditions are presented. By comparing the spectra obtained from the planar substrates of specific crystal orientation, we identify the orientations of nanowire sidewalls and find the correlation of growth direction change (or kinking) and amount of surface hydrogen. Especially, by introducing extrinsic hydrogen, we confirm their important role on nanowire kinking.

The change of surface hydrogen during nanowire growth can also introduce planar defects. In Chapter 4, we show the rational introduction of planar defects into the Si nanowires by changing growth conditions during growth. Rapid modulation of growth temperature and pressure can promote transient change in the amount of surface hydrogen on the solid-vapor interface at the growth front. This process increases the probability of nucleation of planar defects- transverse twin boundaries (TB) and angled stacking faults (SF) from the nanowire surface, which enables controlled placement of planar defects at user-defined positions in the nanowires.

Chapter 5 presents the formation of consecutive formations of transverse TBs in the Si nanowires by controlling growth conditions, changing the method presented in

Chapter 4. A geometric model based on the sidewall facet morphology is provided to explain the diameter-dependent position of secondary TB.

In Chapter 6, the interplay between surface hydrogen and defect propagation in Si nanowire kinking superstructures is presented. A detailed understanding of the interplay between surface termination, defect propagation, and kinking would constitute an important step toward the *ab initio* synthesis of distinct types of high fidelity kinking superstructures.

Finally, Chapter 7 provides the overall conclusions with suggestions for the future work regarding the surface chemistry based structure controls.

1.7. References

1. Gradecak, S.; Qian, F.; Li, Y.; Park, H. G.; Lieber, C. M. *Appl. Phys. Lett.* **2005,** *87*, 173111.
2. Nguyen, H. P. T.; Zhang, S.; Cui, K.; Han, X.; Fathololoumi, S.; Couillard, M.; Botton, G. A.; Mi, Z. *Nano Lett.* **2011,** *11*, 1919-1924.
3. Borgstrom, M. T.; Zwiller, V.; Muller, E.; Imamoglu, A. *Nano Lett.* **2005,** *5*, 1439-1443.
4. Kelzenberg, M. D.; Turner-Evans, D. B.; Kayes, B. M.; Filler, M. A.; Putnam, M. C.; Lewis, N. S.; Atwater, H. A. *Nano Lett.* **2008,** *8*, 710-714.
5. Hochbaum, A. I.; Chen, R. K.; Delgado, R. D.; Liang, W. J.; Garnett, E. C.; Najarian, M.; Majumdar, A.; Yang, P. D. *Nature* **2008,** *451*, 163-168.
6. Boukai, A. I.; Bunimovich, Y.; Tahir-Kheli, J.; Yu, J. K.; Goddard, W. A.; Heath, J. R. *Nature* **2008,** *451*, 168-171.
7. Algra, R. E.; Verheijen, M. A.; Borgstrom, M. T.; Feiner, L. F.; Immink, G.; van Enckevort, W. J. P.; Vlieg, E.; Bakkers, E. *Nature* **2008,** 456, 369-372.
8. Tian, B.; Xie, P.; Kempa, T. J.; Bell, D. C.; Lieber, C. M. *Nat. Nanotechnol.* **2009,** *4*, 824-829.
9. Caroff, P.; Dick, K. A.; Johansson, J.; Messing, M. E.; Deppert, K.; Samuelson, L. *Nat. Nanotechnol.* **2009,** *4*, 50-55.
10. Hocevar, M.; Immink, G.; Verheijen, M.; Akopian, N.; Zwiller, V.; Kouwenhoven, L.; Bakkers, E. *Nat. Commun.* **2012**, *3:1266* doi: 10.1038/ncomms2277
11. Wagner, R. S.; Ellis, W. C. *Appl. Phys. Lett.* **1964,** *4*, 89-90.
12. Schmidt, V.; Wittemann, J. V.; Senz, S.; Gosele, U. *Adv. Mater.* **2009,** *21*, 2681-2702.

13. Park, W. I.; Zheng, G. F.; Jiang, X. C.; Tian, B. Z.; Lieber, C. M. *Nano Lett.* **2008,** *8*, 3004-3009.
14. Borgstrom, M. T.; Immink, G.; Ketelaars, B.; Algra, R.; Bakkers, E. *Nat. Nanotechnol.* **2007,** *2*, 541-544.
15. Dayeh, S. A.; Picraux, S. T. *Nano Lett.* **2010,** *10*, 4032-4039.
16. Kodambaka, S.; Tersoff, J.; Reuter, M. C.; Ross, F. M. *Phys. Rev. Lett.* **2006,** *96*, 096105.
17. Cui, Y.; Lauhon, L. J.; Gudiksen, M. S.; Wang, J. F.; Lieber, C. M. *Appl. Phys. Lett.* **2001,** *78*, 2214-2216.
18. Givargizov, E. I. *J. Cryst. Growth* **1975,** *31*, 20-30.
19. Wu, Y.; Cui, Y.; Huynh, L.; Barrelet, C. J.; Bell, D. C.; Lieber, C. M. *Nano Lett.* **2004,** *4*, 433-436.
20. Zhang, X.; Lew, K. K.; Nimmatoori, P.; Redwing, J. M.; Dickey, E. C. *Nano Lett.* **2007,** *7*, 3241-3245.
21. Schmidt, V.; Senz, S.; Gosele, U. *Phys. Rev. B* **2007,** *75*, 045335.
22. Dubrovskii, V. G.; Sibirev, N. V.; Cirlin, G. E.; Soshnikov, I. P.; Chen, W. H.; Larde, R.; Cadel, E.; Pareige, P.; Xu, T.; Grandidier, B.; Nys, J. P.; Stievenard, D.; Moewe, M.; Chuang, L. C.; Chang-Hasnain, C. *Phys. Rev. B* **2009,** *79*, 205316.
23. Dubrovskii, V. G.; Sibirev, N. V. *Phys. Rev. E* **2004,** *70*, 031604.
24. Schmid, H.; Bjork, M. T.; Knoch, J.; Riel, H.; Riess, W.; Rice, P.; Topuria, T. *J. Appl. Phys.* **2008,** *103*, 024304.
25. Dubrovskii, V. G.; Sibirev, N. V. *J. Cryst. Growth* **2007,** *304*, 504-513.
26. Ross, F. M.; Tersoff, J.; Reuter, M. C. *Phys. Rev. Lett.* **2005,** *95*, 146104.
27. Hyun, Y.-J.; Lugstein, A.; Steinmair, M.; Bertagnolli, E.; Pongratz, P. *Nanotechnology* **2009,** *20*, 125606.
28. Ma, D. D. D.; Lee, C. S.; Au, F. C. K.; Tong, S. Y.; Lee, S. T. *Science* **2003,** *299*, 1874-1877.
29. Schmidt, V.; Senz, S.; Gosele, U. *Nano Lett.* **2005,** *5*, 931-935.
30. Eaglesham, D. J.; White, A. E.; Feldman, L. C.; Moriya, N.; Jacobson, D. C. *Phys. Rev. Lett.* **1993,** *70*, 1643-1646.
31. Hong, S.; Chou, M. Y. *Phys. Rev. B* **1998,** 57, 6262-6265.
32. Hong, S. L. *J. Korean Phys. Soc.* **2000,** 37, 93-98.
33. Oh, S. H.; Chisholm, M. F.; Kauffmann, Y.; Kaplan, W. D.; Luo, W. D.; Ruhle, M.; Scheu, C. *Science* **2010,** *330*, 489-493.
34. Gamalski, A. D.; Ducati, C.; Hofmann, S. *J. Phys. Chem. C* **2011,** *115*, 4413-4417.
35. Wen, C. Y.; Tersoff, J.; Hillerich, K.; Reuter, M. C.; Park, J. H.; Kodambaka, S.; Stach, E. A.; Ross, F. M. *Phys. Rev. Lett.* **2011,** 107, 025503.
36. Wen, C. Y.; Tersoff, J.; Reuter, M. C.; Stach, E. A.; Ross, F. M. *Phys. Rev. Lett.* **2010,** *105*, 195502.
37. Madras, P.; Dailey, E.; Drucker, J. *Nano Lett.* **2009,** *9*, 3826-3830.
38. Dailey, E.; Madras, P.; Drucker, J. *Appl. Phys. Lett.* **2010,** *97*, 143106.
39. Dayeh, S. A.; Wang, J.; Li, N.; Huang, J. Y.; Gin, A. V.; Picraux, S. T. *Nano Lett.* **2011,** *11*, 4200-4206.
40. Musin, I. R.; Filler, M. A. *Nano Lett.* **2012,** *12*, 3363-3368.
41. Shin, N.; Filler, M. A. *Nano Lett.* **2012,** *12*, 2865-2870.

42. Hannon, J. B.; Kodambaka, S.; Ross, F. M.; Tromp, R. M. *Nature* **2006,** *440*, 69-71.
43. Wiethoff, C.; Ross, F. M.; Copel, M.; Hoegen, M. H. V.; Heringdorf, F. *Nano Lett.* **2008,** *8*, 3065-3068.
44. Madras, P.; Dailey, E.; Drucker, J. *Nano Lett.* **2010,** *10*, 1759-1763.
45. Dailey, E.; Madras, P.; Drucker, J. *J. Appl. Phys.* **2010,** *108*, 064320.
46. Davidson, F. M.; Lee, D. C.; Fanfair, D. D.; Korgel, B. A. *J. Phys. Chem. C* **2007,** *111*, 2929-2935.
47. Barth, S.; Boland, J. J.; Holmes, J. D. *Nano Lett.* **2011,** *11*, 1550-1555.
48. Su, Z. X.; Dickinson, C.; Wan, Y. T.; Wang, Z. L.; Wang, Y. W.; Sha, J. A.; Zhou, W. Z. *CrystEngComm* **2010,** 12, 2793-2798.
49. Lopez, F. J.; Givan, U.; Connell, J. G.; Lauhon, L. J. *ACS Nano* **2011,** *5*, 8958-8966.
50. Hemesath, E. R.; Schreiber, D. K.; Kisielowski, C. F.; Petford-Long, A. K.; Lauhon, L. J. *Small* **2012,** *8*, 1717-1724.
51. Jeon, N.; Dayeh, S. A.; Lauhon, L. J. *Nano Lett.* **2013,** *13*, 3947-3952.
52. Tang, W.; Picraux, S. T.; Huang, J. Y.; Gusak, A. M.; Tu, K. N.; Dayeh, S. A. *Nano Lett.* **2013,** *13*, 2748-2753.
53. Tian, B. Z.; Xie, P.; Kempa, T. J.; Bell, D. C.; Lieber, C. M. *Nat. Nanotechnol.* **2009,** *4*, 824-829.
54. Tian, B.; Cohen-Karni, T.; Qing, Q.; Duan, X.; Xie, P.; Lieber, C. M. *Science* **2010,** *329*, 830-834.
55. Jiang, Z.; Qing, Q.; Xie, P.; Gao, R. X.; Lieber, C. M. *Nano Lett.* **2012,** *12*, 1711-1716.
56. Xu, L.; Jiang, Z.; Qing, Q.; Mai, L. Q.; Zhang, Q. J.; Lieber, C. M. *Nano Lett.* **2013,** *13*, 746-751.
57. Pevzner, A.; Engel, Y.; Elnathan, R.; Tsukernik, A.; Barkay, Z.; Patolsky, F. *Nano Lett.* **2012,** *12*, 7-12.
58. Chen, H. A.; Wang, H.; Zhang, X. H.; Lee, C. S.; Lee, S. T. *Nano Lett.* **2010,** *10*, 864-868.
59. Dick, K. A.; Thelander, C.; Samuelson, L.; Caroff, P. *Nano Lett.* **2010,** *10*, 3494-3499.
60. Caroff, P.; Bolinsson, J.; Johansson, J. *IEEE J. Sel. Top. Quant. Electron.* **2011,** *17*, 829-846.
61. Biswas, S.; Singha, A.; Morris, M. A.; Holmes, J. D. *Nano Lett.* **2012,** *12*, 5654-5663.
62. Biswas, S.; O'Regan, C.; Petkov, N.; Morris, M. A.; Holmes, J. D. *Nano Lett.* **2013,** *13*, 4044-4052.
63. Fan, Z. Y.; Kapadia, R.; Leu, P. W.; Zhang, X. B.; Chueh, Y. L.; Takei, K.; Yu, K.; Jamshidi, A.; Rathore, A. A.; Ruebusch, D. J.; Wu, M.; Javey, A. *Nano Lett.* **2010,** *10*, 3823-3827.
64. Zianni, X. *Appl. Phys. Lett.* **2010,** *97*, 233106.
65. Kim, B. S.; Kim, M. J.; Lee, J. C.; Hwang, S. W.; Choi, B. L.; Lee, E. K.; Whang, D. *Nano Lett.* **2012,** *12*, 4007-4012.
66. Oliveira, D. S.; Tizei, L. H. G.; Ugarte, D.; Cotta, M. A. *Nano Lett.* **2013,** *13*, 9-13.

67. Lim, S. K.; Crawford, S.; Haberfehlner, G.; Gradecak, S. *Nano Lett.* **2013,** *13*, 331-336.
68. Yin, Y.; Alivisatos, A. P. *Nature* **2005,** *437*, 664-670.
69. Li, L. S.; Walda, J.; Manna, L.; Alivisatos, A. P. *Nano Lett.* **2002,** 2, 557-560.
70. Manna, L.; Scher, E. C.; Alivisatos, A. P. *J. Am. Chem. Soc.* **2000,** 122, 12700-12706.
71. Jun, Y. W.; Casula, M. F.; Sim, J. H.; Kim, S. Y.; Cheon, J.; Alivisatos, A. P. *J. Am. Chem. Soc.* **2003,** *125*, 15981-15985.
72. Song, J. H.; Sailor, M. J. *J. Am. Chem. Soc.* **1998,** *120*, 2376-2381.
73. Loscutoff, P. W.; Bent, S. F. *Annu. Rev. Phys. Chem.* **2006**, *57*, 467-495.
74. Wolkow, R. A. *Annu. Rev. Phys. Chem.* **1999,** *50*, 413-441.
75. Fink, A.; Huber, R.; Widdra, W. *J. Chem. Phys* **2001,** *115*, 2768-2775.
76. Cho, Y. E.; Maeng, J. Y.; Kim, S.; Hong, S. Y. *J. Am. Chem. Soc.* **2003,** *125*, 7514-7515.
77. Dailey, J. W.; Taraci, J.; Clement, T.; Smith, D. J.; Drucker, J.; Picraux, S. T. *J. Appl. Phys.* **2004,** *96*, 7556-7567.
78. Schmidt, V.; Wittemann, J. V.; Gosele, U. *Chem. Rev.* **2010,** *110*, 361-388.
79. Greenlief, C. M.; Armstrong, M. *J. Vac. Sci. Technol. B* **1995,** 13, 1810-1815.
80. Rauscher, H. *Surf. Sci. Rep.* **2001,** *42*, 207-328.
81. Jasinski, J. M.; Gates, S. M. *Acc. Chem. Res.* **1991,** 24, 9-15.
82. Thibaudau, F.; Albertini, D.; Masson, L.; Salvan, F. *Surf. Sci.* **1997,** *385*, 357-364.

CHAPTER 2

EXPERIMENTAL DETAILS

2.1. Ultra-high vacuum (UHV) chamber

All of the experimental results described in this thesis were obtained from a custom-built ultra-high vacuum (UHV) chamber equipped with a Fourier Transform infrared (FTIR) spectrometer. The system is composed of a 12 inches-diameter spherical main chamber where the nanowire growth is carried out and a load lock chamber for the sample loading/unloading. A top view schematic drawing of the main UHV chamber with FTIR setup is illustrated in Figure 2.1 and perspective view of the overall system and photo are shown in Figure 2.2.

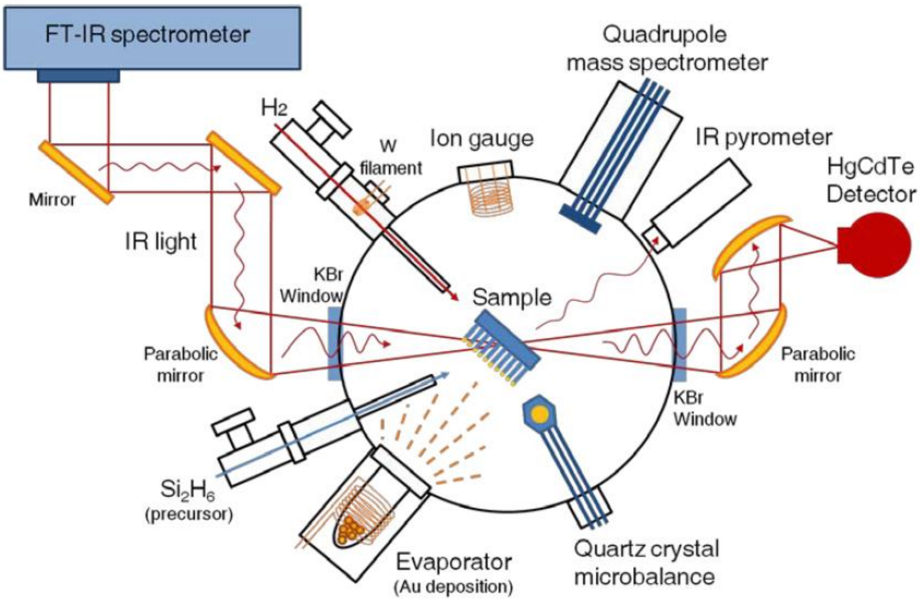

Figure 2.1: A top view schematic diagram of the FTIR-equipped UHV main chamber.

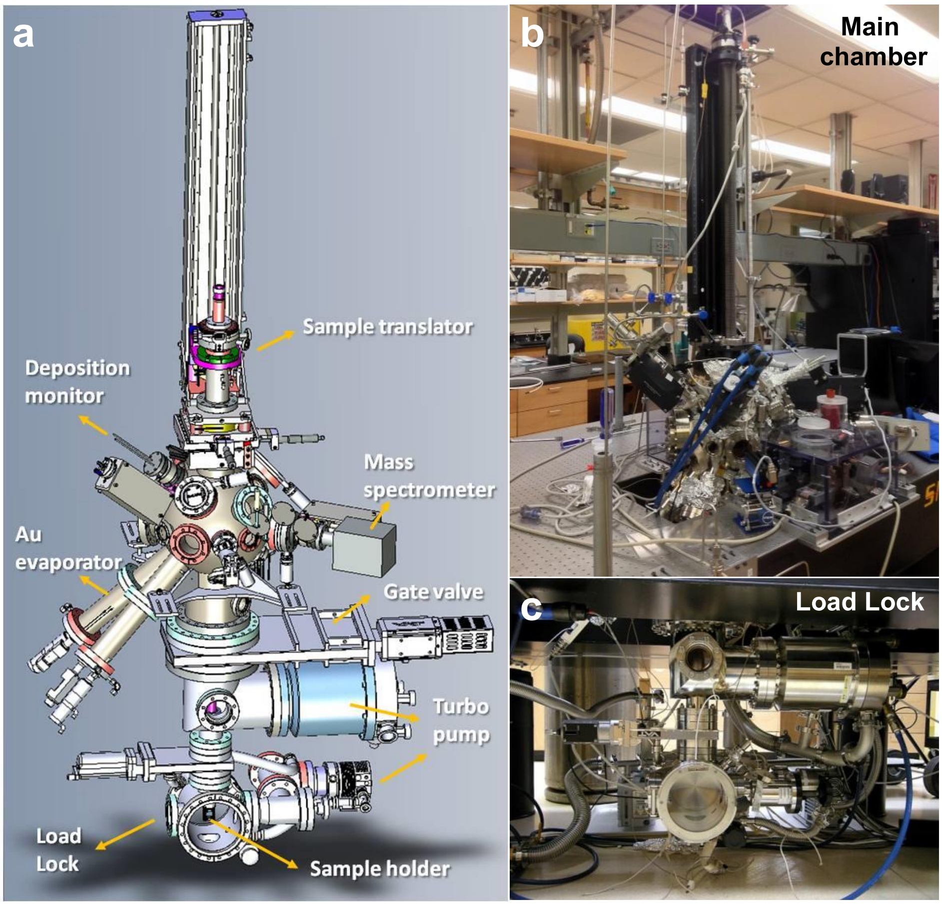

Figure 2.2: (a) A perspective view of UHV chamber system. Photograph of (b) main chamber and (c) load lock assembly.

2.1.1. Vacuum pumps

The vacuum of the main chamber and the load lock is achieved by a "main" 650 L/s magnetic levitation turbomolecular pump (Edwards, STP 603C), and a 60 L/s turbomolecular pump (Edwards, EXT75DX), respectively. An 8" gate valve (VAT, UHV Series 108) is installed between the main UHV chamber and the main turbomolecular pump and the load lock is isolated from the main chamber by a 4" gate valve (VAT, DN100). Both main and load lock turbomolecular pumps are backed by rotary vane (RV) mechanical pumps (Oerlikon Leybold, D16B for main and Edwards, RV8 for load lock).

This configuration of pumps can achieve about 3 × 10^{-10} Torr of overall base pressure in the UHV chamber after 48 – 72 hours bakeout.

2.1.2. Sample holder

A sample holder is used to load the sample substrate into the main UHV chamber. It is designed for the experimental procedure including pre-heating, metal film deposition, nanowire growth, and transmission IR measurements. Figure 2.3 shows the drawing of the sample holder design. Molybdenum (Mo) is used as the material to heat the Si substrate above 1200 °C. The sample substrate cut by 5 ~ 10 mm (height) × 24 mm (width) is placed on the base plate and the position is fixed by 2 Mo clips at sides with Mo screws. Since the sample substrate is heated via direct resistive heating by flowing current, 2 ceramic tube spacers are connecting the two base plates to prevent the electric short from the metal thin film deposition on the sample holder.

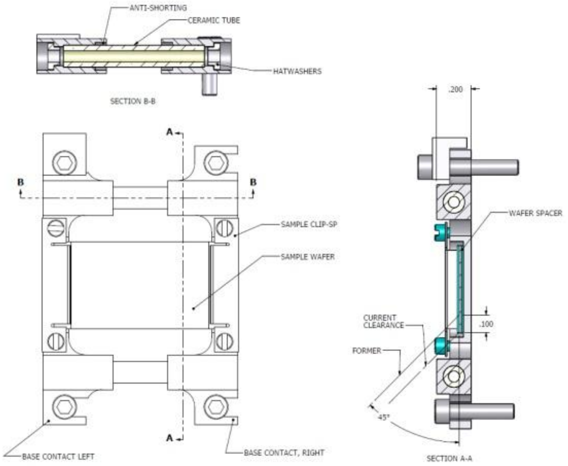

Figure 2.3: Schematic drawing of the sample holder for the nanowire growth.

2.1.3. Load lock and sample translation

The load lock is designed to transfer the sample into the main UHV chamber without venting. In this system, a Z-translator with 36 inches travel length (McAllister Technical Services, ZA4536) mounted on top of the main chamber is transferred down to the load lock chamber through a gate valve, where the space between the translator wall and the gate valve is sealed by two Viton quad seals and differentially pumped by a load lock turbomolecular pump. This enables the venting of the load lock chamber for the sample holder loading. Venting is carried out via an all-metal angle valve (VAT, DN 16) by flowing nitrogen gas, and the sample holder is loaded to the sample translator in atmospheric pressure.

After the sample holder is loaded, the load lock is roughly pumped down by a rotary vane pump (Edwards, RV 12), by opening a small right-angle valve (Kurt J. Lesker). The rough pumping is maintained for approximately 5 minutes until the pressure of about 1×10^{-2} Torr is achieved. Then, the valve is closed and the big right-angle valve (Kurt J. Lesker) connecting the load lock chamber and small turbomolecular pump is opened such that the load lock chamber is further pumped down to about 10^{-7} Torr for the next 15~20 minutes.

Once the appropriate level of pressure is confirmed by a load lock ionization gauge, the Z-translator is raised into the main chamber. The translator is manipulated by a DC motor assembly and controlled remotely. During the initial movement of the translator, it is possible for the main chamber pressure to increase temporarily due to the pressure difference between the main chamber and load lock. Therefore, it is recommended to wait for a sufficient amount of time until the load lock pressure reaches approximately 10^{-7} Torr and the 4” gate valve should be closed as the sample holder assembly is completely out of the gate valve region to minimize further pressure increase in the main chamber. Then, the sample holder is moved to the center of main chamber by raising the translator.

The position of sample holder in the main chamber can be adjusted not only in Z, but also in X, Y, and Θ (rotating) direction. It is essential to position the sample with high precision due to the IR measurement. The motion in X and Y direction is achieved by the XY manipulator (McAllister Technical Services, MC2000), and the rotation by a two-stage differentially-pumped rotary platform (McAllister Technical Services, DPRF275).

2.1.4. Sample heating and cooling

The sample loaded in the main chamber can be heated by the direct heating method. In this method, electric current is directly pumped to the Mo sample holder and conducted through the sample substrate. According to the sample’s intrinsic resistivity and dimension (width, length, and thickness), the available temperature range via resistive heating can be varied. Two different DC power supplies (MKS, SVTA) are used for current flowing. Since the resistance of the semiconductor substrate is highly dependent on the temperature, the power input must be sufficiently large such that the current can flow through the substrate at room temperature during the initial heating. Once the sample is heated and the resistance drops, then the power supply is switched to the other one (SVTA), and the input current is adjusted to the increased value. As the temperature rises, the resistivity of the substrate decreases and rapidly drops at extrinsic regime. Therefore, it is required to take care to prevent the sample from melting. A photograph of sample during the resistive heating is shown in Figure 2.4.

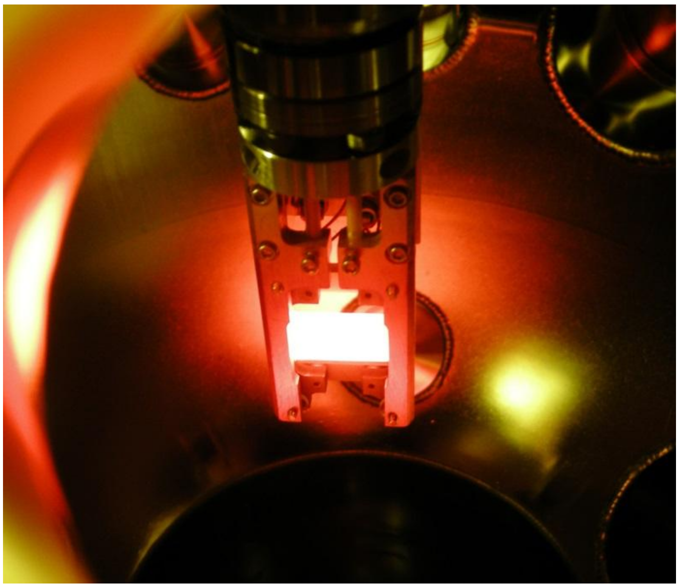

Figure 2.4: Sample substrate during the resistive heating.

Cooling of the sample is achieved by a cold finger attached to the Z-manipulator. By filling liquid nitrogen inside of the finger, the heat from the sample holder is thermally conducted and the sample is cooled down accordingly.

2.1.5. Temperature measurement

Sample temperature is measured by two different methods. First, a thermocouple directly connected to the back plate of the sample holder is used to measure around room temperature range. However, as the sample temperature increases by resistive heating, the response of the thermocouple is slower than the actual temperature change due to the delay in conduction. This necessitates the use of an infrared pyrometer (Mikron) for accurate measurement at the higher temperature range. The pyrometer has a measurable range of temperature between 250 °C and 1350 °C at 100% emissivity setting. Temperature is calibrated by the temperature-programmed desorption (TPD) measurement of atomic hydrogen-saturated Si(100) surface using a quadrupole mass spectrometer (Hiden, HAL/3F 301 RC). Based on the substrate type (i.e. Si or Ge), this emissivity setting can be varied.

2.1.6. Pressure measurement

Two nude UHV ionization gauges (Duniway Stockroom) with a measurable pressure range between 2×10^{-11} Torr and 1×10^{-3} Torr are attached in the main chamber and load lock, respectively. Since the nanowire growth is carried out in various ranges of precursor pressure between 5×10^{-5} Torr and 2×10^{-2} Torr, the ion gauge is usually turned off during the precursor gas flow for the nanowire growth to prevent filament damage. For high pressure growth above 1×10^{-3} Torr, a capacitance manometer (MKS, 627D) is used to measure chamber pressure more accurately.

Pressure of the process lines filled with precursor gases and the exhaust lines of turbomolecular pumps backed by RV mechanical pumps are measured by convection gauges (Kurt J. Lesker, Duniway Stockroom, measuring range – 0.1 mTorr to 1,000 Torr).

2.1.7. Gas delivery, pressure control and hydrogen doser

For the nanowire growth via chemical vapor deposition (CVD) process, pyrophoric precursor gases (Si_2H_6, Ge_2H_6) are used. Therefore, the storage of the precursor cylinders, delivery of gases, and exhaust line connections must consider the potential risk of safety. In figure 2.5, a schematic diagram of gas delivery to the system is shown.

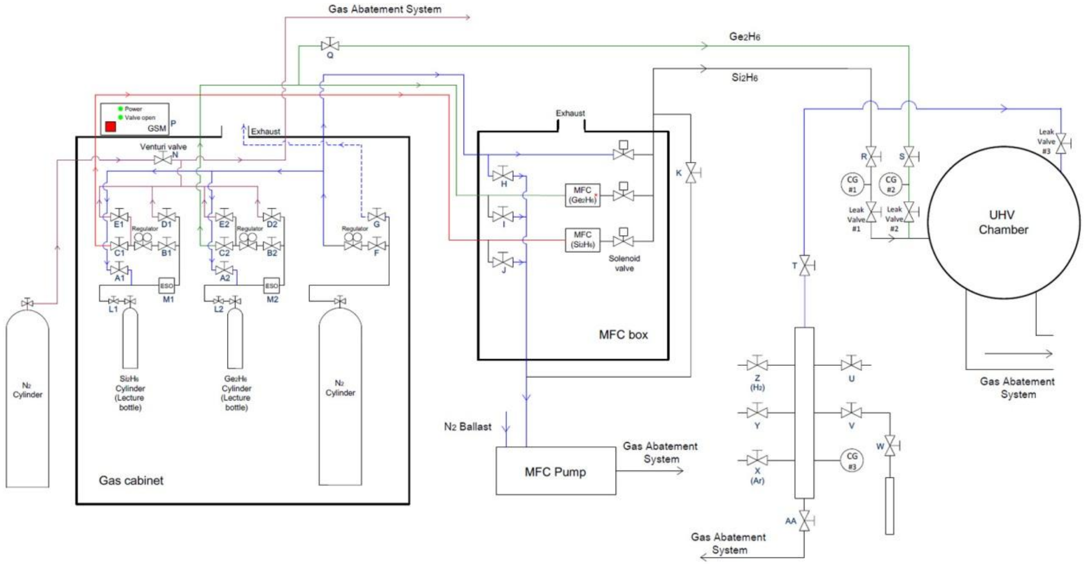

Figure 2.5: Schematic diagram of precursor gas delivery system.

Both Si_2H_6 and Ge_2H_6 cylinders are stored in the gas cabinet and the emergency shut-off (ESO) valves coupled with the gas sensors (Honeywell) are connected to the gas delivery lines such that the flow is automatically shut down when the concentration of gases in the laboratory reaches a certain level. The gases from the outlet of the regulators are delivered to a mass-flow controller (MKS) to control the filling rate of the process lines connected to the main chamber. Finally, the precursor molecules in the process lines are introduced into the chamber via a precision leak valve (Duniway Stockroom, VLVE-1000) coupled with the capillary doser components. The total length of doser is 12.9” and it is directly attached to a *Z*- translator with 4” travel length (McAllister Technical Services). By manipulating the translator, the distance from the doser tip to the sample substrate can be adjusted during the experiment to change the local pressure nearby the sample substrate. For the high pressure growth above 1×10^{-3} Torr, the 8” gate valve between chamber and turbomolecular pump is partially closed while precursor gas is introduced through the leak valve. A controller (VAT, PM5) is used to adjust the degree of closing remotely and it is possible to control the gate valve based on the pressure reading of capacitance manometer to obtain constant pressure.

Unreacted precursor molecules are exhausted from the chamber and sent to a gas abatement system (CSK, CTW600) operated at 800 °C under continuous flow of a water and air environment such that the exhaust gases are completely reacted before being sent to the building ventilation system.

In addition to the delivery of main precursor molecules, other compounds can also be introduced to the chamber via an additional gas manifold. A photograph of the manifold lines is shown in Figure 2.6.

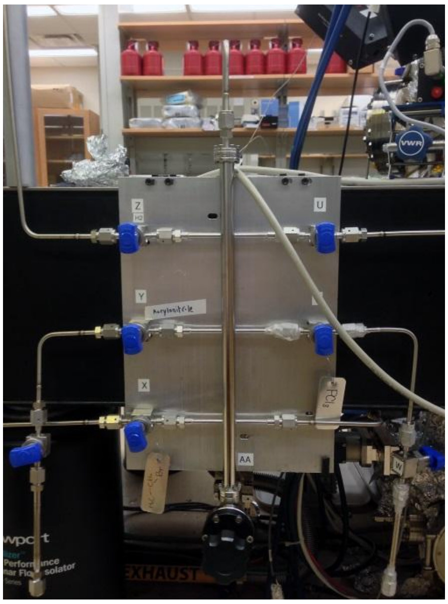

Figure 2.6: Photograph of the gas manifold lines.

Various types of molecular compounds stored in the custom-made stainless steel container (inner volume: 5 mL) are connected to the manifold lines with 2 VCR valves (Swagelok) for purification by multiple cycles of freeze-pump thaw. In usual conditions, the manifold line is evacuated by a RV mechanical pump (Edwards, RV12F) to maintain the base pressure of 10^{-3} Torr. When the compounds are introduced to the system, a right angle valve (Kurt J. Lesker) connecting to the pump is closed to isolate the section filled with molecules.

It is also possible to flow high purity hydrogen gas (Airgas, 99.9999%) through the manifold lines. Molecular hydrogen gas is introduced to the chamber through a separate leak valve (Duniway Stockroom). It is connected to a separate doser (inner diameter: 9.53 mm). This doser is coupled with a W filament (Ted Pella, 99.95%), and resistively heated by electric current to crack the molecular hydrogen from the leak valve. A schematic drawing of the hydrogen doser is depicted in Figure 2.7.

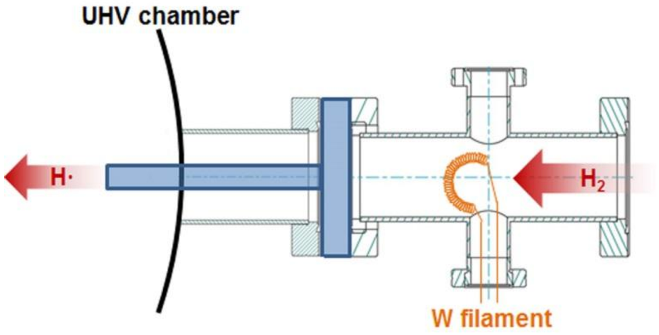

Figure 2.7: Schematic drawing of the hydrogen doser component.

2.2. Sample preparation

For all of the nanowire growths conducted in this research, <111> – oriented Si wafers (El-Cat, FZ, double-side polished, 40–60 Ω-cm, 500 μm thickness) were used and cut by 5 mm (height) × 24 mm (width) for loading on the sample holder.

2.2.1. Native oxide removal

Before the sample substrate is loaded into the chamber, native oxide layers with 2~3 nm thickness are removed by a wet chemical cleaning process. The substrate is immersed in 1M concentration of ammonium fluoride (NH_4F) solution (J.T. Baker) for 5 minutes. Then, the residual solution on the substrate surface is rinsed by deionized water for 30 seconds, followed by nitrogen blowing to remove water. Through this process, the substrate surface is terminated by monohydrides. However, since the termination is temporary under atmospheric pressure, it is desired to transfer the wet-etched substrate into the load lock as immediately as possible.

2.2.2. Flash cleaning

Once the sample is loaded in the load lock and transferred into the main UHV chamber, it is cleaned *in situ* by resistive heating. First, the substrate is pre-annealed for 1 hour at 700 °C to remove any surface desorbed species. Then, it is directly heated to 1200 °C to "flash" for 10 seconds. During this process, oxygen impurities existing in the bulk substrate is diffused out of the surface.[1] The sample is then cooled down to the room temperature at a cooling rate of approximately 2 °C/s. This slow cooling enables the formation of atomically clean, flat Si (111) surface.

2.2.3. Thin film deposition of metal catalyst

To grow nanowires via vapor-liquid-solid (VLS) method from the substrate, it is required to use metals forming eutectic with Si as the growth catalyst. There are various methods for metal deposition onto the substrate, such as colloidal particle solution deposition, thin film deposition via thermal evaporation, or e-beam evaporation. In our system, we employ the thermal (for Au) and e-beam evaporation (for Al) methods to enable *in situ* film deposition onto the vacuum-prepared, clean substrate.

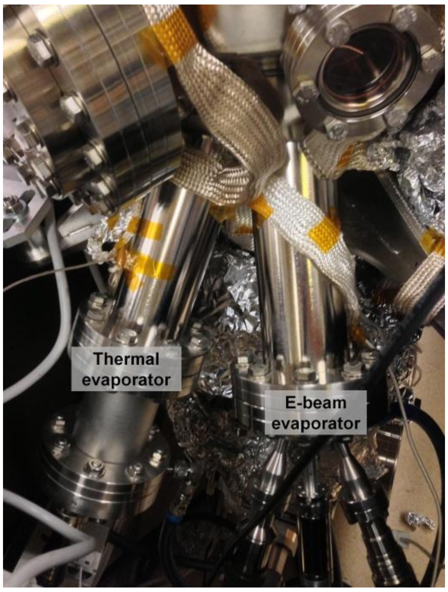

Figure 2.8: Photographs of thermal and e-beam evaporators attached to the main chamber.

2.2.3.1. Thermal evaporation

Thermal evaporation of Au is performed using a hot lip effusion cell (SVT Associates, HL-16). A boron nitride crucible (volume: 40 cc) containing high purity Au shots (ESPI Metals, 99.9999%) is heated above the melting point of Au (1064 °C), and the deposition is initiated at 1310 °C by opening the manual shutter. While the deposition takes place, Au thickness is determined by a UHV-compatible quartz crystal microbalance (QCM) monitor (MKS Instruments). When the desired thickness is achieved, the shutter is closed and the effusion cell is slowly cooled down to the room temperature at the rate of 0.3 °C/s.

2.2.3.2. E-beam evaporation

Aluminum is deposited from an E-beam evaporator (Mantis Deposition, Quad-EV-C). Since Al wets the normal crucible, an alumina crucible with PBN liner should be used to contain Al shots (ESPI Metals, 99.9995%). Similar to Au evaporation, the deposition amount is monitored by QCM, but the flux monitor installed in the evaporator also provides the information of deposition amount. By adjusting the current flowing through the filament and the crucible, approximately 1 nm thick Al film is deposited in 2 minutes at the flux of 5.0 nA.

2.3. Sample characterization

2.3.1. Infrared (IR) spectroscopy

Infrared (IR) spectroscopy is employed for the detection of surface adsorbates on the semiconductor substrates.[2] Group IV semiconductor materials such as Si or Ge are transparent to the infrared light, and there are two techniques generally used for the semiconductor surface studies.

First, multiple internal reflection (MIR) is used by reflecting incident IR light multiple times in high refractive index semiconductor crystal. This enables the detailed analysis of surface adsorbates with enhanced sensitivity by multiple interrogation of substrate surface.[2,3] However, due to the long optical path length, specific spectrum of IR is absorbed to the substrate. For Si, the absorption of spectrum up to 1500cm^{-1} occurs by multiphonon bands.[4] This makes it challenging to analyze the characteristic vibrational modes existing in the region. Moreover, in MIR, the waves used for the detection of adsorbates are evanescent, which the intensity decays exponentially in vacuum.[2] In this research, nanowires grow out from the substrate with different surface geometry. Therefore, the amplitude of evanescent wave becomes different between the positions of the nanowire sidewalls as the growth continues. In addition, since nanowires have differently oriented sidewalls from the original substrate, their geometry likely modify the evanescent wave generation.

Therefore, transmission geometry is employed by transmitting IR light to the substrate only once to minimize the substrate lattice phonon absorption.[5] Figure 2.9 shows the examples of IR absorption spectra measured in two different geometries.

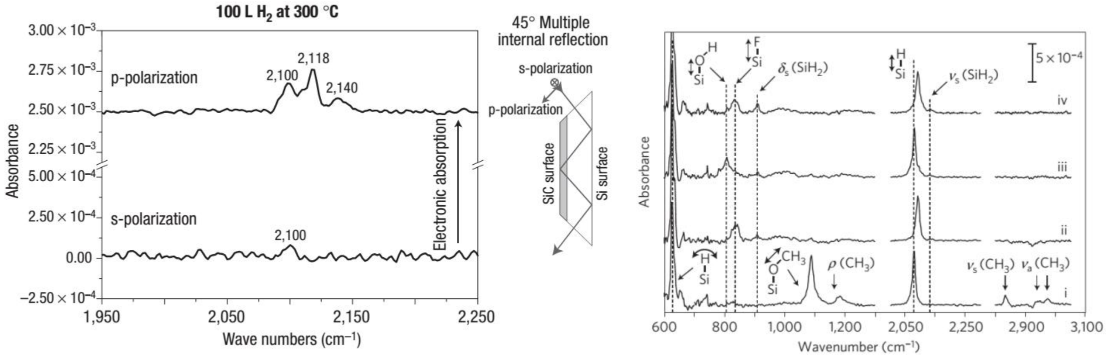

(a) (b)

Figure 2.9: Examples of infrared absorption spectra. (a) Multiple internal reflection (MIR) spectroscopy measured from H terminated Si(100) surface.[6] (b) Transmission infrared absorption spectra measured from Si(111) surface terminated by H, F, OH groups.[7] (a) Adapted by permission from Macmillan Publishers Ltd: *Nat. Mater.* Derycke *et al*,[6] copyright 2003. (b) Adapted by permission from Macmillan Publishers Ltd: *Nat. Mater*. Michalak *et al*,[7] copyright 2010.

In our system, *in situ* transmission IR measurements of surface hydrogen vibrational modes are accomplished with a Bruker Vertex 70 spectrometer coupled to the UHV chamber system described above. IR light generated from a Globar source passes through a KBr beam-splitter, and exits the spectrometer as unpolarized. The beam is reflected by 2 flat Au-coated mirrors, and then focused by a 90° off-axis Au-coated parabolic mirror with the effective focal length of 10”. The focused light enters the chamber through a differentially-pumped KBr chamber window, and transmitted through a sample substrate. After transmission, the beam exists through the other KBr window at opposite side, and the second 90° off-axis Au-coated parabolic mirror (EFL: 10”) collimates the beam, then the beam is again focused by a third 90° off-axis parabolic mirror (EFL: 3”) onto a liquid nitrogen-cooled mercury-cadmium-telluride (MCT) detector (Figure 2.10b). This provides access to the mid-IR spectral region (4000 – 600

cm^{-1}). The IR beam path is enclosed by plastic boxes and cylinders which are continuously purged by dry air which is filtered by a FT-IR purge gas generator (Parker Balston), to minimize the unwanted absorption from water (H_2O) and carbon dioxide (CO_2) in the atmospheric environment of the IR beam path.

Real-time measurement is achieved by starting a background single scan acquisition while nanowires grow at desired constant temperature and pressure. Then, a sample scan is measured and ratioed to the background to obtain absorbance spectra. The number of scans varies according to the growth conditions.

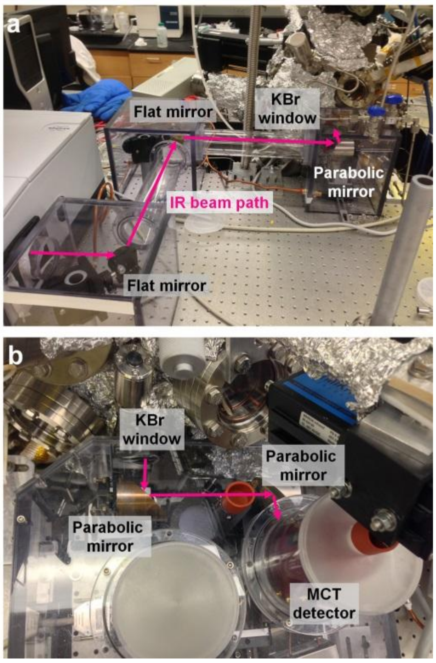

Figure 2.10: Photographs of IR measurement setup showing IR beam path.

2.3.2. Electron microscopy

Scanning electron microscopy (SEM) and transmission electron microscopy (TEM) were used to identify the structure of nanowires such as growth orientations, sidewall facet morphology, planar defects, etc. In TEM measurement, dark-field imaging as well as bright-field is used to identify the Au atoms existing on the surface of nanowire sidewalls. An aberration-corrected high angle annular dark-field scanning transmission electron microscopy (HAADF-STEM) imaging is used to confirm the bilayer stacking structure and identify the spacing between each planar defect.

In this work, a Zeiss Ultra 60 field emission SEM (FE-SEM) and a Leo 1550 FE-SEM are used for SEM analysis. For bright/dark-field TEM analysis, FEI Tecnai F20, Hitachi HF-3300, and JEOL 100 CX II are used. HAADF-STEM images are obtained from FEI Titan S 80-300.

2.4. References

1. Hannon, J. B.; Kodambaka, S.; Ross, F. M.; Tromp, R. M. *Nature* **2006,** *440*, 69-71.
2. Chabal, Y. J. *Surf. Sci. Rep.* **1988,** *8*, 211-357.
3. Higashi, G. S.; Chabal, Y. J. ; Trucks, G. W.; Raghavachari, K. *Appl. Phys. Lett.* **1989,** *56*, 656-658.
4. Queeney, K. T.; Fukidome, H.; Chaban, E. E.; Chabal, Y. J. *J. Phys. Chem. B* **2001,** *105*, 3903-3907.
5. Webb, L. J.; Rivillon, S.; Michalak, D. J.; Chabal, Y. J.; Lewis, N. S. *J. Phys. Chem. B* **2006,** *110,* 7349-7356.
6. Derycke, V.; Soukiassian, P. G.; Amy, F.; Chabal, Y. J.; D'angelo, M. D.; Enriquez, H. B.; Silly, M. G. *Nat. Mater.* **2003,** *2*, 253-258.
7. Michalak, D. J.; Amy, S. R.; Aureau, D.; Dai, M.; Estève, A.; Chabal Y. J. *Nat. Mater.* **2010,** 9, 266-271.

CHAPTER 3

CONTROLLING SILICON NANOWIRE GROWTH DIRECTION VIA SURFACE CHEMISTRY

3.1. Overview[†]

This chapter describes the demonstration of *in situ* chemical investigation of vapor–liquid–solid Si nanowire growth and the important role of transient surface chemistry near the triple-phase line is investigated. Real-time infrared spectroscopy measurements coupled with postgrowth electron microscopy demonstrate that covalently bonded hydrogen atoms are responsible for the ⟨111⟩ to ⟨112⟩ growth orientation transition commonly observed during Si nanowire growth. These results provide insight into the root cause of well-known nanowire growth phenomenon and open a new route to rationally engineer the crystal structure of these nanoscale semiconductors.

3.2. Introduction and background

Semiconductor nanowires (NWs) are promising building blocks for advanced energy conversion, quantum computation, and photonic devices.[1-3] Similar to other nanomaterials, their physical properties are intimately connected to their structure, which must be controlled with remarkable precision. Despite gaining important insight into the vapor-liquid-solid (VLS) growth process in recent years,[4-6] the clarification of several

---

[†] Reprinted with permission from Shin, N.; Filler, M.A. *Nano Lett*. **2012**, *12*, 2865-2870. Copyright 2012 American Chemical Society.

fundamental questions is still required for robust *ab initio* structure engineering. In particular, the mechanism that underlies changes to NW growth direction, which is commonly referred to as "kinking" and was initially reported by Wagner and Doherty over 40 years ago,[7] continues to be debated. Robust control of this process promises novel nanoscale superstructures[8] as well as devices with previously unattainable function.[9] The transition from <111> to <112> oriented growth commonly observed in the classic Si/Au semiconductor NW/catalyst system has been extensively studied both experimentally[10-13] and theoretically.[14-16] Prior experimental reports demonstrate the temperature and pressure dependence of this behavior, which is often ascribed to changes in catalyst supersaturation and/or defect plane introduction. On the other hand, early experimental studies[7] as well as recent theoretical modeling[15,16] indicate that local surface energy changes, caused by temperature perturbations or other means, can also drive kinking.

Except for studies of NWs with *in situ* transmission electron microscopy (TEM),[17-19] much of the progress to date has been achieved through empirical tuning of process parameters and postgrowth characterization. Unfortunately, *ex situ* analyses preclude the detection of the short-lived or unstable chemical bonds present during, and responsible for key aspects of, NW growth. To our knowledge, there exists no direct measurement of the atomic-scale chemistry that dictates interface energetics in these systems. To this end, we show how *in situ* transmission infrared (IR) spectroscopy can uncover previously unknown details regarding solid-vapor interface bonding for Au-catalyzed Si NWs. As opposed to post-growth IR characterization of HF-etched Si

NWs,[20] the real-time measurements described here can access transient surface chemistry and, in doing so, reveal a common thread that underlies kink formation.

Group IV and III-V semiconductor NW growth protocols predominantly rely upon hydride (e.g. Si_2H_6, PH_3) and metalorganic (e.g. $In(CH_3)_3$) precursors to deliver atoms to the catalyst tip. Importantly, the substituents (e.g. –H or $–CH_3$) delivered with each precursor molecule can strongly influence surface adsorption, decomposition, and desorption events. For example, the removal of H atoms delivered with each hydride species is the rate-limiting step during Si epitaxy and necessitates substrate temperatures at or above 500 – 550 °C to ensure that H_2 desorption is sufficiently fast.[21] As 1-D Si NW growth occurs at temperatures as much as 150 °C lower than 2-D films, non-negligible quantities of hydrogen should be expected near the triple-phase line (i.e. where the vapor, liquid, and solid meet) and, as we show here, can strongly influence multiple aspects of VLS growth.

3.3. Experimental methods

3.3.1. Nanowire growth

A detailed description of our custom-built ultrahigh vacuum system and sample preparation procedures are described in Chapter 2. Si NWs are grown using 100% Si_2H_6 (Voltaix, 99.998%) as a precursor and Au as the catalyst. A 2 nm gold film is initially evaporated on a vacuum-prepared (i.e. clean) Si(111) substrate from an effusion cell (SVT Associates). To increase the local pressure, Si_2H_6 is delivered to the substrate surface though a variable leak valve (Duniway Stockroom) coupled to a stainless steel direct doser (inner diameter: 6.35 mm) with the tip placed 1 cm from the center of the substrate. All NWs are grown with a two-step process that includes an (1) incubation and (2) elongation step. During the incubation step, the temperature is maintained at 590 °C for 15 min with Si_2H_6 pressure of 1×10^{-5} Torr for all samples. NW elongation is then carried out at 1×10^{-4} Torr with temperatures between 415 – 550 °C for 120 min or at 1×10^{-3} Torr with temperatures between 450 – 600 °C for 20 min. This procedure maintains NW areal densities and diameters at 0.98 ± 0.06 μm^{-2} and 151 ± 20 nm, respectively, as shown in Figure 3.1 and 3.2.

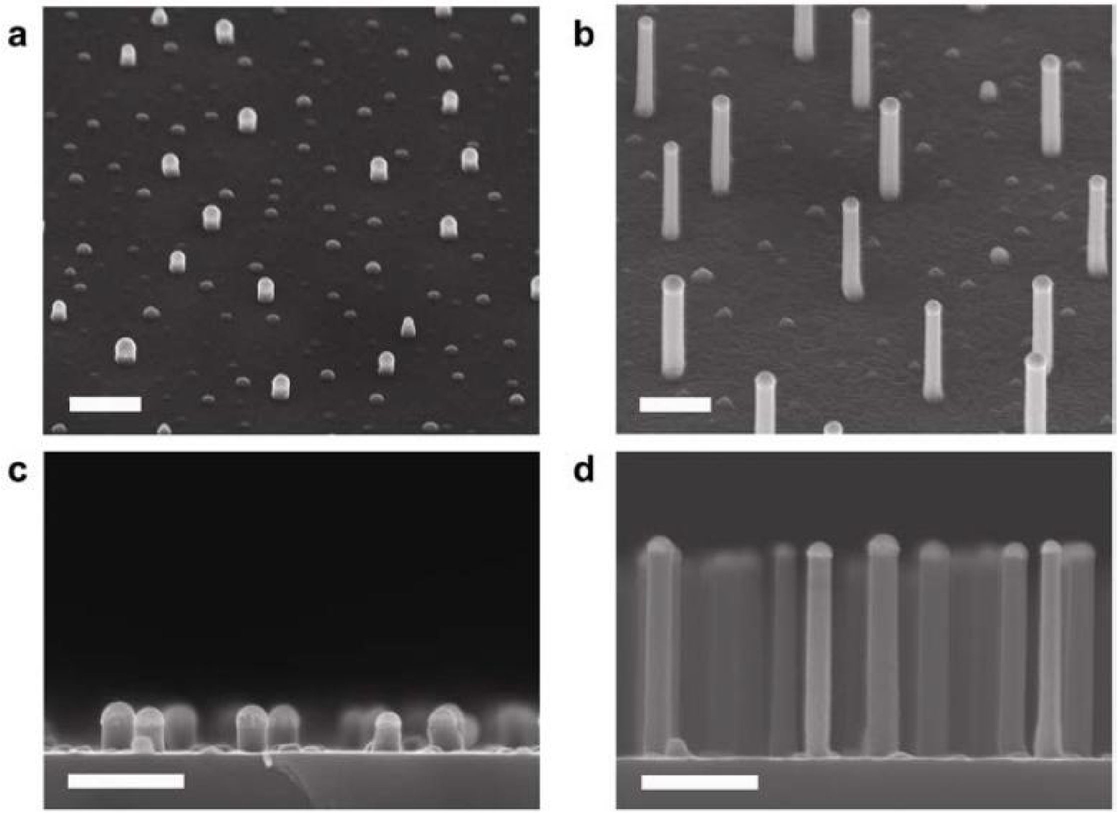

Figure 3.1: Two-step "incubation" and "elongation" growth procedure. (a, c) SEM images of Si NWs immediately after the incubation step at 590 °C and 1×10^{-5} Torr Si_2H_6 for 15 min. All Si NWs undergo the identical incubation procedure. (b, d) SEM images of Si NWs following the subsequent elongation step at 490 °C and 5×10^{-5} Torr Si_2H_6 for 120 min. The temperature and pressure of each elongation step is varied as labeled in each main figure and described in the text. Scale bars: 600 nm.

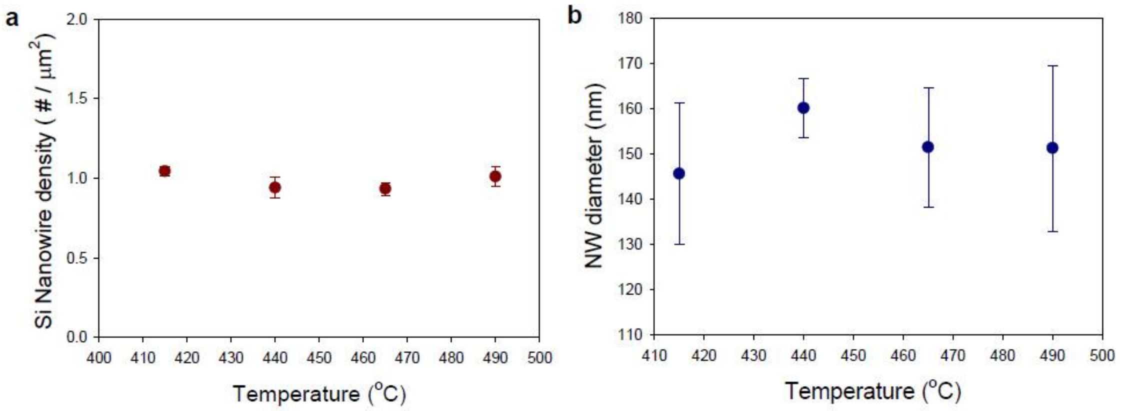

Figure 3.2: Two-step growth maintains Si NW density and diameter. (a) Number density of Si NWs grown via the two-step incubation and elongation procedure described in Figure 3.1. (b) Diameter distribution of Si NWs grown with the same incubation and elongation conditions as (a). In the cases shown here, the Si_2H_6 pressure during the elongation step was 1×10^{-4} Torr.

H_2 (AirGas, 99.9999%) can be introduced, when necessary, through a separate variable leak valve (Duniway Stockroom) and stainless steel directed doser (inner diameter: 9.53 mm) combination. The distance from the tip to the sample surface is 4 cm. A W filament (Ted Pella, 99.95 %) situated between the vacuum side of the H_2 leak valve and inlet to the directed doser enable H atom generation while minimizing the delivery of cracked Si_2H_6 species to the substrate.

3.3.2. IR measurements

For the real-time measurements described here, the incident angle of the IR light on the substrate surface is set to 58 °. All spectra, except those acquired at 1×10^{-3} Torr Si_2H_6, consist of 4000 scans acquired at a resolution of 4 cm^{-1} using Blackman-Harris apodization. Due to the speed of NW growth at 1×10^{-3} Torr Si_2H_6, 1200 scans were used for these experiments. Baseline correction is accomplished via a standard concave rubberband procedure with two iterations and peak areas are determined by integrating over a range ± 4 cm^{-1} around the peak maximum. It is important to note that all IR measurements during the NW growth are recorded while the sample is maintained at the elongation temperature as indicated in each figure. Both the background and sample scans occur during the elongation step, such that ν(Si–H) vibrations originating from the substrate do not change during the NW growth. Spectra from different temperatures and pressures are acquired in distinct experiments, each utilizing a new substrate. For Si_2H_6 and atomic H adsorption studies on planar substrates, both the temperature and pressure are maintained as indicated throughout the sample scan, with a clean substrate at the same temperature serving as the IR background.

3.3.3. SEM and TEM analysis

A Zeiss Ultra 60 field emission SEM, FEI Tecnai F20 TEM, and JEOL 100 CX II TEM are used to structurally characterize the Si NWs. Samples are imaged with SEM without further preparation. For TEM imaging, substrates are ultrasonicated post-growth in methanol for 3 min followed by dispersion of the NW-containing solvent on lacey carbon grids (Ted Pella).

3.4. Results and discussion

We initially verify the previously reported transition from <111> to <112> oriented growth as a function of elongation pressure and temperature (Figure 3.3).[10]

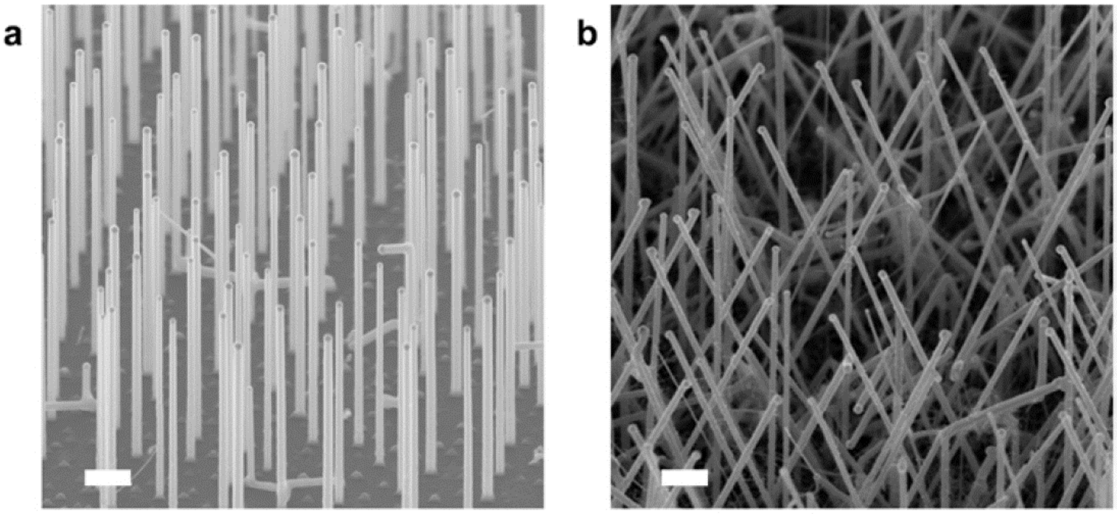

Figure 3.3: SEM images of <111> and <112> oriented Si NWs. (a) <111> Si NWs grown at 490 °C and 1 × 10^{-4} Torr Si_2H_6 for 120 min. Scale bar, 1 μm. (b) <112> Si NWs grown at 490 °C and 1 × 10^{-3} Torr Si_2H_6 for 20 min. Scale bar: 1 μm.

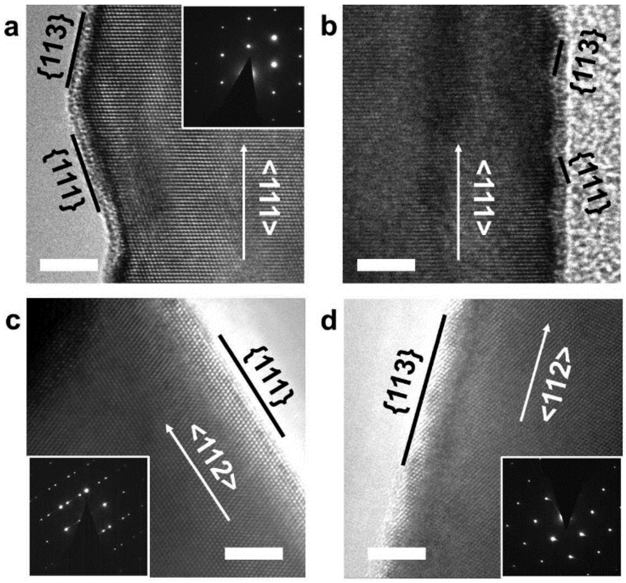

Figure 3.4: HRTEM images of different growth directions and sidewall orientations for Si NWs. (a, b) Bright-field image of a <111> Si NW grown at 490 °C and 1 × 10^{-4} Torr Si_2H_6 for 120 min. The SAED pattern inset shows that {112} oriented sidewalls exhibit {111} and {113} subfaceting. (c) Bright-field image of a <112> Si NW grown at 415 °C and 1 × 10^{-4} Torr Si_2H_6 for 120 min. The SAED pattern inset confirms a {111} sidewall assignment and also indicates that a twin plane is present. (d) Bright-field image of a <112> Si NW grown at 440 °C and 1 × 10^{-3} Torr Si_2H_6 for 20 min. A {113} sidewall assignment is possible via the SAED pattern inset. All images and diffraction patterns are measured along the [110] zone axis. Scale bars: 5 nm.

Figure 3.4 shows *ex situ* high-resolution transmission electron microscopy (HRTEM) images and selected area electron diffraction (SAED) patterns from representative <111> and <112> oriented Si NWs. Figure 3.4a shows that <111> oriented NWs exhibit {112} sidewalls that are sub-faceted into periodic {111} and {113} surfaces. The large {111} and {113} sub-facets result from modulation of the triple-phase line (Figure 3.4a), as previously shown,[22] whereas the smaller sub-facets on the opposite side of the NW are likely due to Si coarsening in the presence of Au after the growth front has passed (Figure 3.4b).[23] Figures 3.4c and 3.4d show that <112> oriented NWs are bounded by {111} and {113} sidewalls without sub-faceting. Similar to prior reports,[13] twinning boundaries are sometimes (Figure 3.4c), but not always (Figure 3.4d), observed in our <112> oriented NWs.

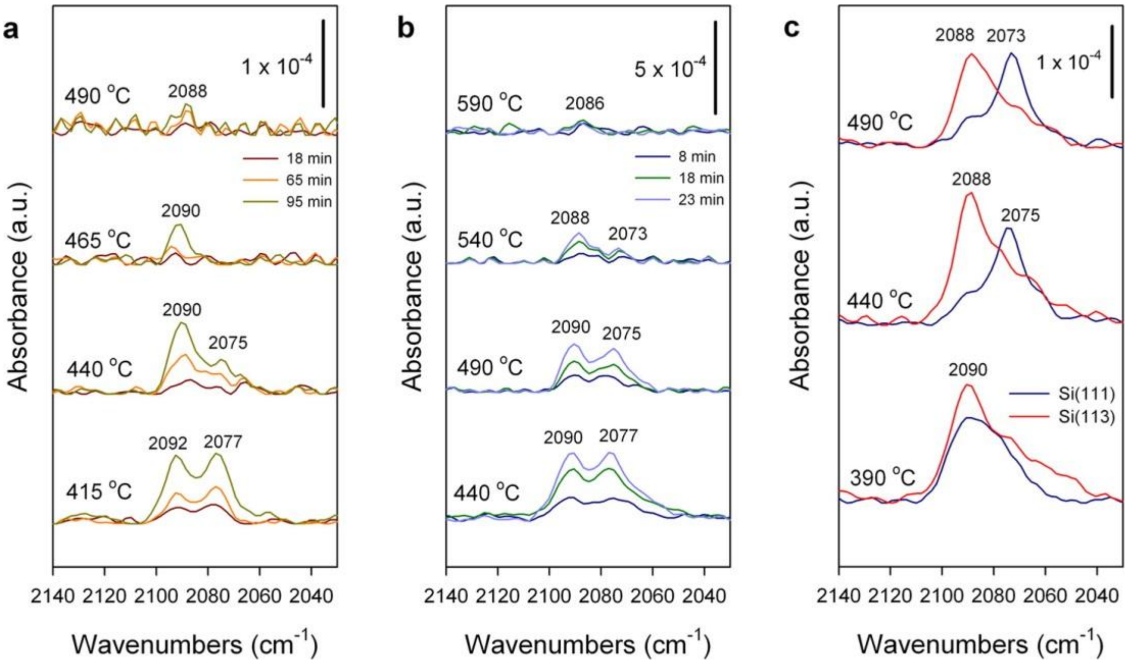

Figure 3.5: *In situ* IR spectra of the ν(Si–H) stretching region. (a) Time-dependent (18, 65, and 95 min) IR spectra measured during Si NW growth at 1 × 10^{-4} Torr Si_2H_6 and temperatures as indicated. (b) Time-dependent (8, 18, 23 min) IR spectra measured during growth at 1 × 10^{-3} Torr Si_2H_6 and temperatures as

indicated. (c) IR spectra measured during 1 × 10^{-4} Torr Si_2H_6 exposure to planar, vacuum-prepared Si(111) (blue) and Si(113) (red) substrates maintained at the indicated temperatures.

Time– and temperature dependent IR spectra recorded at elongation pressures of 1 × 10^{-4} and 1 × 10^{-3} Torr are shown in Figures 3.5a and 3.5b, respectively. Two characteristic absorption bands appear near 2075 and 2090 cm^{-1} and increase in intensity as the temperature of the elongation step is reduced. We attribute these features to monohydride ν(Si–H) stretching vibrations resulting from covalently-bonded surface hydrogen.[24,25] It is important to note that the observed surface hydrogen must originate from the Si_2H_6 precursor itself since no carrier gas (e.g. H_2) is utilized. Experimental design combined with a series of additional control experiments confirm that the observed spectral features result from hydrogen adsorbed on the NW *sidewall* rather than the Si(111) substrate. Foremost, continuous exposure of Si_2H_6 to an already saturated Si(111) substrate at relevant temperatures and pressures does not induce spectral changes as a function of time (Figure 3.6).

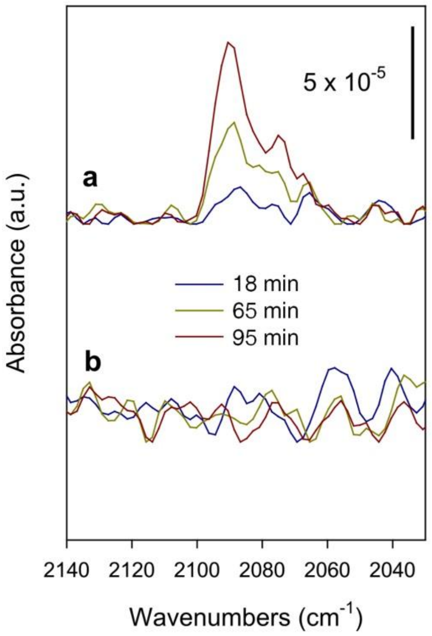

Figure 3.6: Spectral features result from the Si NWs rather than the Si(111) substrate. (a) Time-dependent IR spectra of Si NWs grown with 1 × 10^{-4} Torr Si_2H_6 at 440 °C. Spectra are ratioed to a background recorded immediately following initiation of the elongation step. (b) Time-dependent IR spectra of an Au-free Si(111) substrate exposed to Si_2H_6 at the same temperature and pressure as (a). Spectra are ratioed to a background recorded shortly after exposure to the precursor. These featureless spectra confirm that the contribution from the substrate is constant during real-time growth measurements and that the observed signal results from the Si NWs.

By acquiring background spectra at the temperature and pressure of the elongation step, we can ensure that substrate termination remains constant during NW growth and its spectral contribution negligible. An examination of integrated peak area as a function of NW length yields additional support. Figure 3.7a exhibits time dependent IR spectra for a series of <111> oriented NW growths and the SEM images in Figure 3.7b show the corresponding NW lengths at the end of each experiment. Similar to Figure 3.5, the intensity of the ν(Si–H) bands increases as a function of time. A comparison of the integrated peak area of the 2090 cm^{-1} mode with NW length, as shown in Figure 3.7c, reveals a strong correlation between the observed ν(Si–H) modes and NW length, which further supports the conclusion that these modes originate from the NW sidewall.

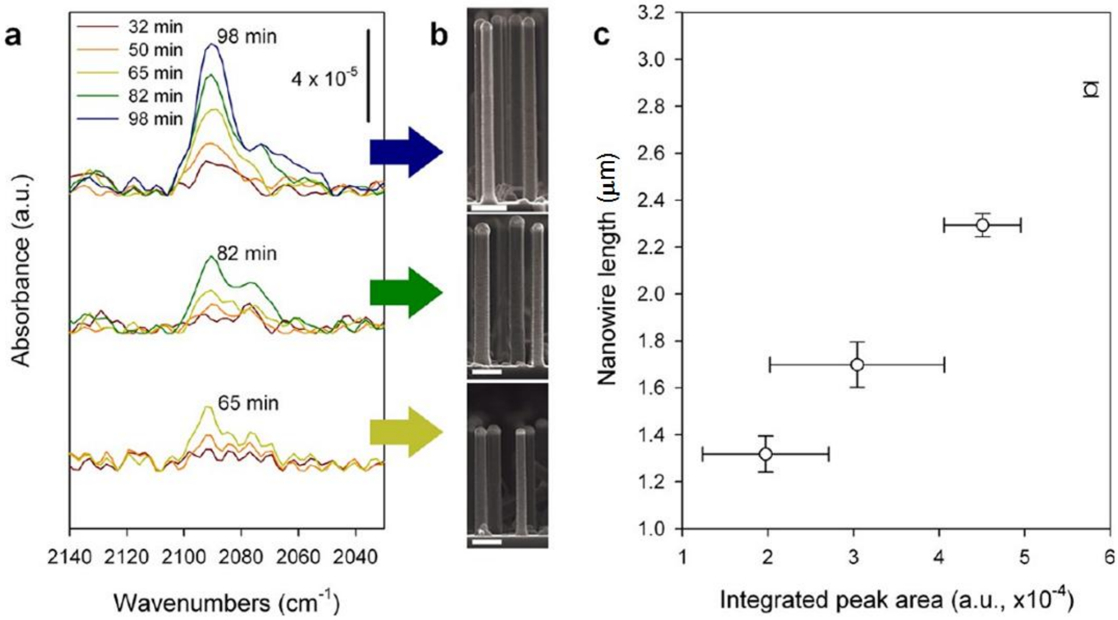

Figure 3.7: Correlation of ν(Si–H) stretching modes to Si NW length. (a) Time-dependent IR spectra recorded for Si NWs grown at 1 × 10^{-4} Torr Si_2H_6 and 440 °C for a total of 65, 82, and 98 min. (b) Cross-sectional SEM images showing the final length of NWs corresponding to spectra in (a). Scale bars: 500 nm. (c) Si NW length plotted as a function of 2090 cm^{-1} peak area. Peak integration is performed between 2086 and 2094 cm^{-1} for all samples.

A series of Si_2H_6 adsorption experiments on planar substrates enable the specific NW sidewall associated with each IR absorption band in Figure 3.5a and 3.5b to be identified. While several studies of Si_2H_6 adsorption on Si surfaces under ultrahigh vacuum conditions exist,[26,27] the ability of surface structure and chemistry to change significantly at higher pressures[28] motivates new experiments at conditions relevant for Si NW growth. As described above and previously observed by others,[12,22] the sidewalls of <111> (Figure 3.4a and 3.4b) and <112> (Figure 3.4c and 3.4d) oriented Si NWs are largely comprised of {111} and {113} surfaces. Figure 3.7 shows IR spectra acquired during exposure of 1 × 10^{-4} Torr Si_2H_6 to vacuum-prepared (i.e. clean) Si(111) and

Si(113) surfaces. Adsorption on Si(113) reveals a strong ν(Si–H) mode near 2090 cm^{-1} and a weaker shoulder near 2073 cm^{-1} for all temperatures. A small temperature-dependent redshift, similar to Figure 3.5a and 3.5b, is also observed. The coincidence of the 2090 cm^{-1} mode on the NW with that from planar Si(113) supports its assignment to hydrogen present on {113} sidewall facets during NW growth. The adsorption of Si_2H_6 on Si(111) reveals a more complex temperature dependence. While a peak near 2090 cm^{-1} appears at 390 °C, the mode near 2073 cm^{-1} becomes more prevalent at 440 °C and 490 °C. There is a strong correspondence between the 2073 cm^{-1} peak on the Si(111) substrate and that seen during NW growth. Thus, we conclude that hydrogen is also present on {111} sidewall facets as the NW elongates. It is important to note that the temperature dependence on the absorption features from Si(111) suggests that there is a non-negligible activation barrier to complete Si_2H_6 decomposition.[29] Given the presence of mobile Au atoms on the NW sidewall, it is initially surprising that no discernible difference exists between the ν(Si–H) modes observed during NW growth and during adsorption on Au-free surfaces. However, mixed monolayers of Au/H are known to phase separate[30] and suggest we are observing vibrations from the interior of H dominated phases. Although this data supports the assignment of each absorbance band, 2090 and 2073 cm^{-1}, to hydrogen adsorbed on a specific NW sidewall facet, {113} and {111}, respectively, a more detailed understanding of the atomic-level bonding configuration (e.g. 1 × 1 vs 2 × 1, etc.) requires additional investigation and is beyond the scope of this work.

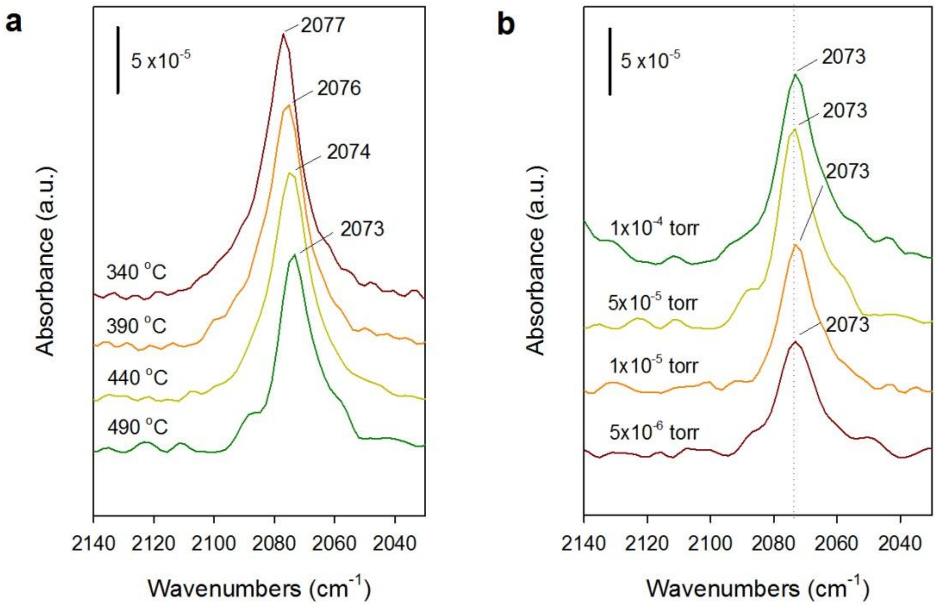

Figure 3.8: Deconvolution of hydrogen coverage and substrate temperature effects. (a) ν(Si–H) stretching modes recorded during a saturation exposure of atomic hydrogen to a vacuum-prepared Si(111) substrate held at 340, 390, 440, or 490 °C for 15 min. (b) ν(Si–H) stretching modes recorded during exposure of a vacuum-prepared Si(111) substrate to 5×10^{-6} , 1×10^{-5} , 5×10^{-5} , and 1×10^{-4} Torr H_2 with the W filament on for 15 min with the substrate temperature maintained at 490 °C. The dotted line is a guide to show that the peak position is constant.

While the behavior of both ν(Si–H) bands in Figures 3.5a and 3.5b suggest that hydrogen coverage on the NW sidewall is inversely proportional to temperature, a series of control experiments are required to confirm this initial conclusion. Figure 3.8a shows a temperature dependent study of the dynamic equilibrium between hydrogen atom adsorption/desorption on vacuum-prepared planar Si(111). A continuous saturation exposure of hydrogen atoms across the temperature range of interest for Si NW growth reveals that ν(Si–H) peak position undergoes a small red-shift, but peak area does not change appreciably. This behavior indicates that not all of the intensity is quenched via high temperature processes such as adsorbate–phonon coupling.[25] On the other hand, the pressure dependent spectra in Figure 3.8b show that peak position remains constant while intensity increases at constant temperature. We can therefore conclude that the decrease in ν(Si–H) peak intensity during Si NW growth (Figure 3.5a and 3.5b) predominantly results from hydrogen desorption, likely in the form of H_2, as the temperature is increased. We attribute the red-shift to temperature related effects that are not important to the conclusions of the present work.

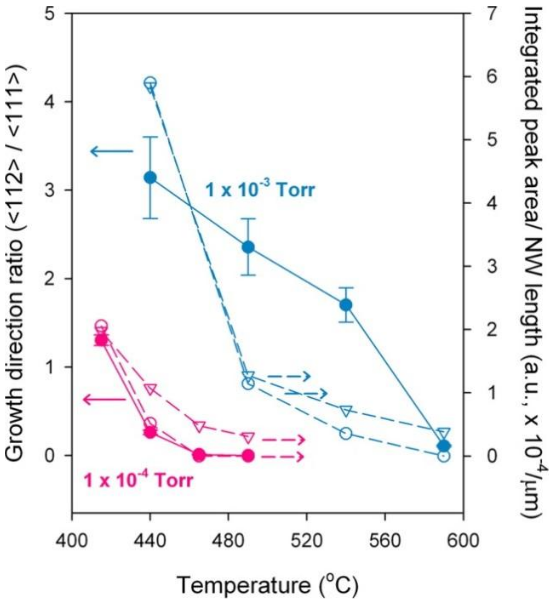

Figure 3.9: Correlation of Si NW growth direction and ν(Si–H) peak intensity. <112> to <111> growth direction ratio and integrated ν(Si–H) peak area per unit of Si NW length as a function of elongation step temperature and pressure (1×10^{-4} or 1×10^{-3} Torr Si_2H_6). The growth direction ratio is shown with solid circles, while the open triangles and circles correspond to the integrated area of the absorbance bands centered near 2090 and 2075 cm^{-1}, respectively. Growth direction ratio statistics are derived from SEM images of NWs in 3 different 5 μm × 5 μm areas (5000× magnification). An average of 234 NWs are included for each temperature/pressure condition. The error bars show one standard deviation on either side of the mean.

Importantly, we observe a strong correlation between hydrogen coverage and the ratio of <112> to <111> oriented NWs. The <112>/<111> growth direction ratio and the integrated ν(Si–H) peak intensities per unit of NW length, a quantity proportional to hydrogen coverage, are plotted as a function of substrate temperature in Figure 3.9. <111> oriented NWs grow when there is little or no surface hydrogen, whereas <112> oriented NWs begin to appear as the quantity of adsorbed hydrogen increases. While the correlation is stronger at 1 × 10^{-4} Torr, the same general trend is observed at 1 × 10^{-3} Torr. A basic understanding of adsorption and desorption phenomena explains this result. At low pressures and high temperatures, the rate of Si_2H_6 impingement and H_2 desorption are slow and fast, respectively. Hydrogen coverage on the NW sidewall is reduced under these situations and a dark-field TEM image shown in Figure 3.10b indicates that Au readily diffuses from the catalyst tip, as previously observed.[11,23,31] At higher pressures and lower temperatures, the coverage of hydrogen increases because the impingement rate of Si_2H_6 is fast and H_2 desorption is slow. Dark-field imaging indicates that Au wetting of the NW sidewall is distinct in this situation (Figure 3.10d). While prior studies suggest that hydrogen in acting as an Au diffusion barrier,[30] additional experiments are required to fully understand the H/Au relationship in this system. Although Lugstein *et al.* show that a <112> oriented growth yield of nearly 100 % is possible,[32] our process window likely precludes a similar observation. More specifically, we cannot generate a sufficiently high hydrogen concentration because the design of our pumping system limits operation to pressures at or below 1 × 10^{-3} Torr, and NW growth becomes exceedingly unstable at substrate temperatures below 400 °C.

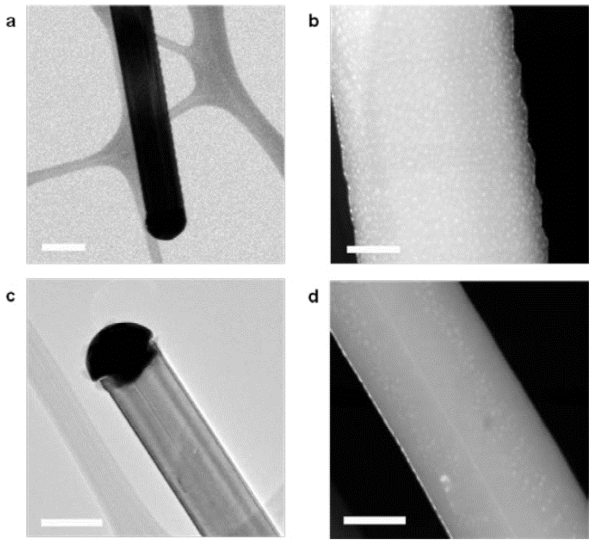

Figure 3.10: Au sidewall coverage as a function of growth direction. (a) Bright-field TEM image of a <111> Si NW grown with 1 × 10^{-4} Torr Si_2H_6 at 490 °C for 120 min. Scale bar: 200 nm. (b) Dark-field STEM image of the NW shown in (a). Au nanoparticles are observed on all sidewalls. Scale bar: 40 nm. (**c**) Bright-field TEM image of a <112> Si NW grown with 1 × 10^{-4} Torr Si_2H_6 at 415 °C for 120 min. Scale bar: 100 nm. (**d**) Dark-field STEM image of the same <112> NW as in (c). Sidewalls are only partially covered by Au nanoparticles. Scale bar: 50 nm. All TEM images are along the [110] zone-axis.

To definitively prove that hydrogen is responsible for these morphological changes, we performed a series of *in situ* atomic hydrogen dosing experiments during Si NW growth. Figures 3.11a and 3.11b show NWs grown at conditions that yield a <111> orientation (400 °C, 5 × 10^{-5} Torr Si_2H_6) after 60 and 150 min, respectively. Figure 3.11c shows a NW where molecular hydrogen (5 × 10^{-4} Torr H_2) was added to the Si_2H_6 environment (5 × 10^{-5} Torr Si_2H_6) between 60 and 150 min. No changes to growth rate or direction are observed in this situation. Figure 3.11d shows a NW grown at the same temperature, but at half of the pressure (2.5 × 10^{-5} Torr Si_2H_6) between 60 and 150 min. We note that the growth rate under these reduced pressure conditions is 2.7 nm/min (0.4 Å/sec), approximately one bilayer per 7 seconds. Another control experiment confirms that any Si_2H_6 reaching the hot W filament does not influence the NW growth rate or direction (Figure 3.12).

However, as shown in Figure 3.11e, a very different result is observed when atomic hydrogen, created by cracking H_2 (5×10^{-4} Torr H_2) on a hot W filament, is delivered to the sample between 60 and 150 min. A clear kink away from <111> oriented growth is observed upon the addition of hydrogen atoms for 88% of the NWs (Figure 3.13). Although the growth rate in this situation is 3.3 nm/min (0.5 Å/sec), a value substantially lower than other reports,[10,13] data in Figure 3.11d confirms that reduced growth rates are not solely responsible for kinking.

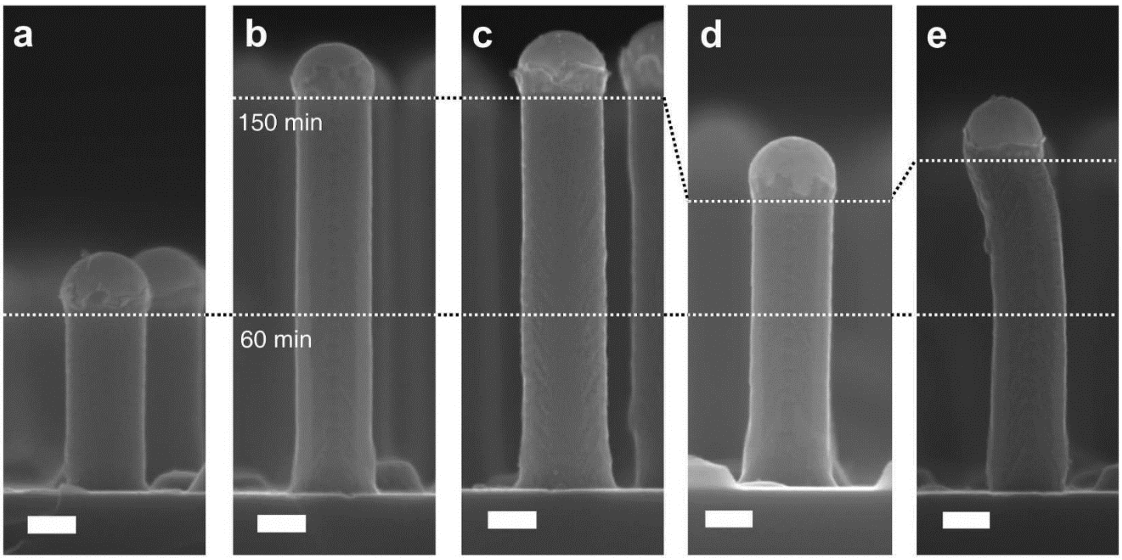

Figure 3.11: Atomic hydrogen induced kinking of Si NWs. SEM images of representative Si NWs grown (a) for 60 min with 5×10^{-5} Torr Si_2H_6 at 490 °C, (b) for 150 min under the same conditions as (a), (c) for 60 min under the same conditions as (a) followed by the addition of 5×10^{-4} Torr H_2 with the W filament off for another 90 min (150 min total), (d) for 60 min under the same conditions as (a) followed by a reduction of the pressure to 2.5×10^{-4} Torr Si_2H_6 for another 90 min (150 min total), (e) for 60 min under the same conditions as (a) followed by the addition of 5×10^{-4} Torr H_2, at the same Si_2H_6 pressure, with the W filament on for another 90 min (150 min total). Scale bars: 100 nm.

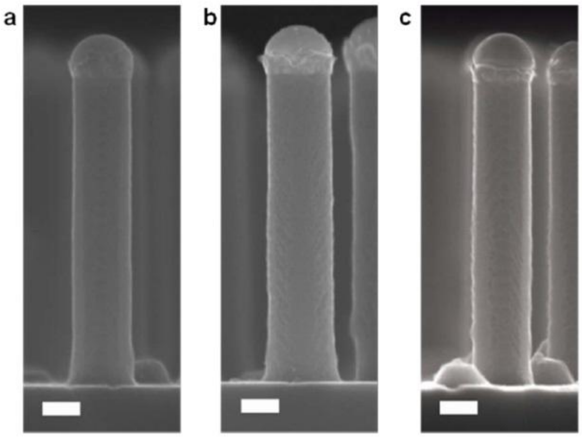

Figure 3.12: Effect of H_2 and the W filament on Si NW growth. SEM images of a Si NW grown (a) with 5 × 10^{-5} Torr Si_2H_6 at 490 °C for 150 min (identical to Figure 3.11b), (b) for 60 min under the same conditions as (a) followed by the addition of 5 × 10^{-4} Torr H_2 with the W filament off for another 90 min (150 min total), (c) for 60 min under the same conditions as (a) followed by turning the filament on in the absence of H_2 for another 90 min (150 min total). These control experiments confirm that molecular H_2 and any Si_2H_6 cracked at the hot W filament do not impact growth rate or direction. Scale bars: 100 nm.

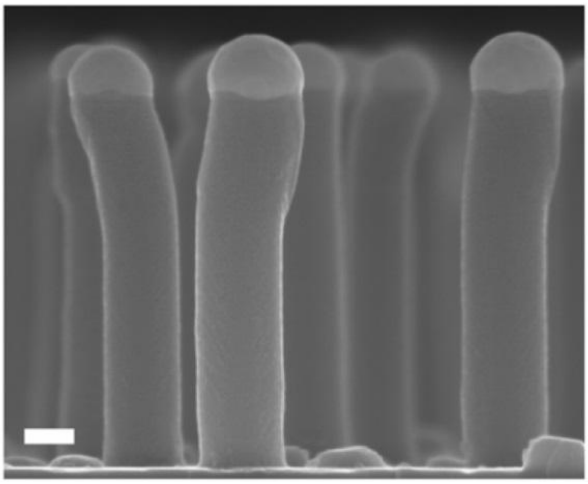

Figure 3.13: Cross-section SEM image showing H-atom induced kinking in Si NWs grown at 5 × 10^{-5} Torr Si_2H_6 and 5 × 10^{-4} Torr H_2 at 490 °C with the W filament on (same as Figure 3.11e). Scale bar: 100 nm.

As shown in Figure 3.14, a longer exposure to H atoms confirms that the new growth direction is <112>. The rough sidewall, especially on the <111> oriented base, is attributed to etching by atomic hydrogen after the growth front has passed. We also observe single "stubs" along the sidewall of the <112> section for some NWs (Figure

3.14a), a phenomenon that is ascribed to the difference between H atoms derived from H_2 cracking and Si_2H_6 decomposition. However, these features do not appear to impact growth direction. These results provide striking evidence that transiently adsorbed hydrogen is responsible for the <111> to <112> growth direction transition in the classic Si/Au NW/catalyst system. Although previous reports corroborate the modulation of growth direction and catalyst diffusion, the *in situ* analysis completed here connects these changes to surface chemistry and provides a mechanistic justification for the first time.

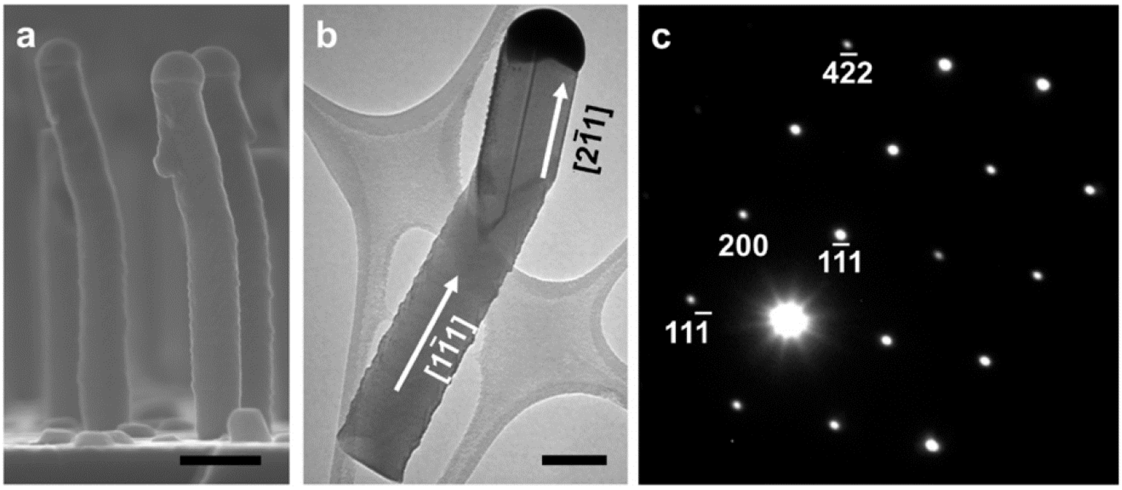

Figure 3.14: Direction of H-atom induced kinking. (a) SEM image of Si NWs grown for 60 min with 5×10^{-5} Torr Si_2H_6 at 490 °C followed by the addition of 1×10^{-4} Torr H_2, at the same Si_2H_6 pressure, with the W filament on for another 120 min (180 min total). Scale bar: 200 nm. (b) Bright-field TEM image of a representative Si NW grown with the same conditions as (a). A defect plane is visible in the <112> oriented segment. Scale bar: 100 nm. (c) SAED pattern of the NW in (b), measured along the [110] zone axis, confirming the <112> oriented growth upon the addition of H atoms.

We now briefly discuss the microscopic mechanism that underlies kinking as a function of surface termination. In particular, we propose that covalently bonded hydrogen, which is prevalent in the triple-phase region under reaction conditions that favor <112> oriented growth, reduces the solid-vapor interface energy (γ_{SV}) and favors distinct sidewall facets. The stability of these newly stabilized facets (*vide infra*) changes the force balance at the triple phase line and drives growth into a new direction (<112> here). Calculations of hydrogen-terminated group IV semiconductor surfaces (e.g. C, Si, and Ge),[33] which show that the energy change upon surface covalent bond formation can be large, supports this explanation. Our findings also corroborate recent modeling by Tersoff and coworkers,[16] which indicate that subtle changes to γ_{SV} are sufficient to induce kinking.

We expect that the particular set of facets and kink direction is NW structure and chemistry (e.g. diameter, contact angle, precursor, reaction conditions, etc.) dependent. Closed-packed facets (e.g. {111}) are generally expected under conditions that favor monohydrides, while lower density facets (e.g. {100} or {110}) are likely more favorable when additional hydrogen is present. This behavior is supported by our data. When monohydrides exist on the sidewall (Figure 2), <112> oriented Si NWs with a smooth {111} facet are observed in the present work (Figure 3.15) and by others.[12,34] Although further investigation is required to unravel the interconnectivity between adsorbate species, facet stability, and preferred crystal orientation, these results provide crucial insight into the atomic-level chemistry that influences Si NW growth direction and open the door to *ab initio* kink design.

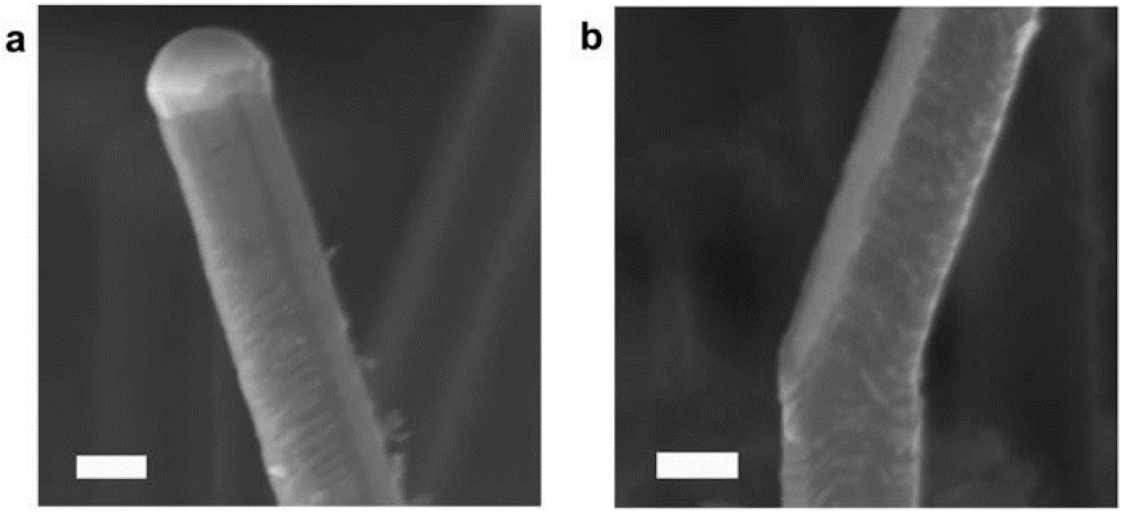

Figure 3.15: <112> oriented NWs exhibit a smooth {111} sidewall facet. (a) SEM image near the tip of a Si NW grown with 1 × 10^{-4} Torr Si_2H_6 at 415 °C for 120 min. (b) SEM image near the kink of a Si NW grown with the same conditions as (a). Scale bars: 100 nm.

3.5. Conclusion

In conclusion, our results represent an important step toward answering long-standing questions regarding kinking during Au-catalyzed Si NW growth. We specifically reveal the critical role of hydrogen near the triple-phase line and create new opportunities to control the structure and physical properties of semiconductor NWs via surface chemistry. The tendency of the observed chemical bonds to change following synthesis or upon removal from the vacuum environment necessitates the *in situ* spectroscopic measurements performed here. These findings are of general importance and are expected to advance the rational engineering of this (e.g. group IV) and other semiconductor NW systems (e.g. group III-V).

3.6. References

1. Tian, B. Z.; Zheng, X. L.; Kempa, T. J.; Fang, Y.; Yu, N. F.; Yu, G. H.; Huang, J. L.; Lieber, C. M. *Nature* **2007,** *449*, 885-U888.
2. Nadj-Perge, S.; Frolov, S. M.; Bakkers, E.; Kouwenhoven, L. P. *Nature* **2010,** *468*, 1084-1087.
3. Chen, R.; Tran, T. T. D.; Ng, K. W.; Ko, W. S.; Chuang, L. C.; Sedgwick, F. G.; Chang-Hasnain, C. *Nature Photonics* **2011,** *5*, 170-175.
4. Dick, K. A. *Prog. Cryst. Growth Charact. Mater.* **2008,** *54*, 138-173.
5. Schmidt, V.; Wittemann, J. V.; Senz, S.; Goesele, U. *Advanced Materials* **2009,** *21*, 2681-2702.
6. Ross, F. M. *Rep. Prog. Phys.* **2010,** *73*, 114501.
7. Wagner, R. S.; Doherty, C. J. *J. Electrochem. Soc.* **1968,** *115*, 93-99.
8. Tian, B.; Xie, P.; Kempa, T. J.; Bell, D. C.; Lieber, C. M. *Nat. Nanotechnol.* **2009**, *4*, 824-829.
9. Tian, B. Z.; Cohen-Karni, T.; Qing, Q.; Duan, X. J.; Xie, P.; Lieber, C. M. *Science* **2010,** *329*, 830-834.
10. Madras, P.; Dailey, E.; Drucker, J. *Nano Lett.* **2009,** *9*, 3826-3830.
11. Madras, P.; Dailey, E.; Drucker, J. *Nano Lett.* **2010,** *10*, 1759-1763.
12. Dailey, E.; Madras, P.; Drucker, J. *J. Appl. Phys.* **2010,** *108*, 064320.
13. Dayeh, S. A.; Wang, J.; Li, N.; Huang, J. Y.; Gin, A. V.; Picraux, S. T., *Nano Lett.* **2011,** *11*, 4200-4206.
14. Schwalbach, E. J.; Davis, S. H.; Voorhees, P. W.; Wheeler, D.; Warren, J. A. *J. Mater. Res.* **2011,** *26*, 2186-2198.
15. Schwarz, K. W.; Tersoff, J. *Nano Lett.* **2011,** *11*, 316-320.
16. Schwarz, K. W.; Tersoff, J.; Kodambaka, S.; Chou, Y. C.; Ross, F. M. *Phys. Rev. Lett.* **2011**, *107*, 265502.
17. Hofmann, S.; Sharma, R.; Wirth, C. T.; Cervantes-Sodi, F.; Ducati, C.; Kasama, T.; Dunin-Borkowski, R. E.; Drucker, J.; Bennett, P.; Robertson, J. *Nature Materials* **2008,** *7*, 372-375.
18. Kim, B. J.; Tersoff, J.; Kodambaka, S.; Reuter, M. C.; Stach, E. A.; Ross, F. M. *Science* **2008,** *322*, 1070-1073.
19. Oh, S. H.; Chisholm, M. F.; Kauffmann, Y.; Kaplan, W. D.; Luo, W.; Ruehle, M.; Scheu, C. *Science* **2010,** *330*, 489-493.
20. Sun, X. H.; Wang, S. D.; Wong, N. B.; Ma, D. D. D.; Lee, S. T.; Teo, B. K. *Inorg. Chem.* **2003,** *42*, 2398-2404.
21. Gupta, P.; Colvin, V. L.; George, S. M. *Phys. Rev. B* **1988,** *37*, 8234-8243.
22. Ross, F. M.; Tersoff, J.; Reuter, M. C. *Phys. Rev. Lett.* **2005**, *95*, 146104.
23. Wiethoff, C.; Ross, F. M.; Copel, M.; Hoegen, M. H.-v.; Heringdorf, F.-J. M. z. *Nano Lett*. **2008**, *8*, 3065−3068.

24. Higashi, G. S.; Chabal, Y. J.; Trucks, G. W.; Raghavachari, K. *Appl. Phys. Lett.* **1990,** *56*, 656-658.
25. Dumas, P.; Chabal, Y. J.; Higashi, G. S. *Physical Review Letters* **1990,** *65*, 1124-1127.
26. Uram, K. J.; Jansson, U. *Surf. Sci.* **1991,** *249*, 105-116.
27. Shinohara, M.; Niwano, M.; Neo, Y.; Yokoo, K. *Thin Solid Films* **2000,** *369*, 16-20.
28. Tao, F.; Dag, S.; Wang, L.-W.; Liu, Z.; Butcher, D. R.; Bluhm, H.; Salmeron, M.; Somorjai, G. A. *Science* **2010,** *327*, 850-853.
29. Xia, L. Q.; Jones, M. E.; Maity, N.; Engstrom, J. R. *J. Chem. Phys.* **1995**, *103*, 1691−1701.
30. Oura, K.; Lifshits, V. G.; Saranin, A. A.; Zotov, A. V.; Katayama, M. *Surface Science Reports* **1999,** *35*, 1-69.
31. den Hertog, M. I.; Rouviere, J.-L.; Dhalluin, F.; Desre, P. J.; Gentile, P.; Ferret, P.; Oehler, F.; Baron, T. *Nano Lett.* **2008,** *8*, 1544-1550.
32. Lugstein, A.; Steinmair, M.; Hyun, Y.; Hauer, G.; Pongratz, P.; Bertagnolli, E. *Nano Lett*. **2008**, 8, 2310.
33. Stekolnikov, A. A.; Furthmuller, J.; Bechstedt, F. *Phys. Rev. B* **2002**, *65*, 115318.
34. Hyun, Y. J.; Lugstein, A.; Steinmair, M.; Bertagnolli, E.; Pongratz, P. *Nanotechnology* **2009**, *20*, 125606.

CHAPTER 4

RATIONAL DEFECT INTRODUCTION IN SILICON NANOWIRES

4.1. Overview[†]

The controlled introduction of planar defects, particularly twin boundaries and stacking faults, in group IV nanowires remains challenging despite the prevalence of these structural features in other nanowire systems (e.g. II-VI and III-V). In this chapter, we demonstrate how user-programmable changes to precursor pressure and growth temperature can rationally generate both transverse twin boundaries and angled stacking faults during the growth of <111> oriented Si nanowires. We leverage this new capability to demonstrate prototype defect superstructures. These findings yield important insight into the mechanism of defect generation in semiconductor nanowires and suggest new routes to engineer the properties of this ubiquitous semiconductor.

4.2. Introduction and background

Defect superstructures offer an unparalleled opportunity to manipulate the function of nanoscale semiconductors. The placement of planar defects, particularly twin boundaries (TBs) and stacking faults (SFs), at user-programmable locations would create new routes to tune optical, electrical, and/or thermophysical properties.[1-3] For example, transverse {111} TBs and SFs – those oriented perpendicular to the nanowire axis – are

---

[†] Reprinted with permission from Shin, N.; Chi, M.; Howe, J. Y.; Filler, M. A. *Nano Lett.* **2013**, *13*, 1928-1933. Copyright 2013 American Chemical Society.

readily formed in <111> oriented III-V nanowires synthesized via the vapor-liquid-solid (VLS) technique.[4-6] Recent reports of twinning superlattices highlight the remarkable level of structural control that is already possible in this system.[7-9]

Group IV and III-V nanowires exhibit a number of well documented, and currently unexplained, differences.[10,11] Foremost, defects in Si and Ge nanowires usually appear as single or multiple longitudinal {111} TBs – those oriented parallel to the nanowire axis – in <112> nanowires.[12,13] Hexagonal polytypes[14] or ordered defect arrays[15] are occasionally observed as well and assigned to various Si polytypes, but some controversy remains.[16,17] Randomly positioned transverse TBs are also reported in Si nanowires synthesized with catalysts other than Au, including Al,[18] Cu,[19] Ga,[20] In,[21] or Au/Ag alloys.[22] However, there are no reports of <111> oriented Si nanowires with rationally introduced defect planes. In fact, the fabrication of defects in Si nanowires remains sufficiently challenging that alternative approaches, including crystal structure transfer, have been pursued.[23] The clear differences between group IV and III-V nanowires are particularly surprising since these material systems exhibit similar bulk defect formation energies. For example, the twin plane energy in bulk Si and GaAs is 22 and 19.5 meV/bond, respectively.[24]

Here, we demonstrate that TBs and SFs can be rationally positioned within Si nanowires by rapidly modifying growth conditions. More specifically, we simultaneously increase precursor partial pressure and reduce substrate temperature for a short time interval during <111> oriented Si nanowire growth. We correlate two types of planar defects with the user-applied “condition change”: (1) transverse TBs or (2) angled (19.5° from the <111> direction) SFs and leverage this insight to fabricate prototype defect superstructures, consisting of equally spaced TBs or SFs, for the first time in the Si nanowire system. Our results suggest that surface chemical bonding plays an important role in the defect generation process.

4.3. Experimental methods

4.3.1. Sample preparation

Si(111) wafers (El-Cat, FZ, double-side polished, 40-60 Ω-cm) were cut to 5 mm × 24 mm prior to immersion in 1M HF solution for 5 min, rinsing in deionized (DI) water, and loading into the sample holder. Substrate heating occurs via direct resistive heating and temperature is monitored by an infrared pyrometer (Mikron). Substrate outgassing occurs at 700 °C under vacuum for 1 hr. The sample was subsequently flashed to 1200 °C for 30 s prior to cooling to room temperature at a rate below 2 K/s. A thin Au (ESPI Metals, 99.9999%) layer was deposited via *in situ* thermal evaporation (SVT Associated) with the substrate held at room temperature.

4.3.2. Nanowire growth

Si nanowires were synthesized via a two-step process, which includes an incubation and elongation step, to achieve a uniform diameter distributions and reproducible areal densities. The incubation step begins by exposing an Au-covered Si substrate to Si_2H_6 (Voltaix, 99.998%) at a pressure of 2×10^{-4} Torr while ramping the substrate temperature to 590 °C for 2 min. At the start of the elongation step, the substrate temperature is reduced to 490 °C at a rate of 3 K/s while the Si_2H_6 pressure is maintained as 2×10^{-4} Torr. The "condition change" described in Chapter 4.4 refers to the near simultaneous increase in Si_2H_6 pressure to 5×10^{-4} Torr and reduction of substrate temperature to 410 °C for 1 min prior to returning to the original elongation conditions. The pressure change takes 10 sec and occurs first while the substrate temperature is changed immediately afterward at a rate of 8 K/s. At the end of 1 min, the reverse process is applied.

4.3.3. SEM and TEM analysis

Structural characterization of Si nanowires was carried out using a combination of several instruments, including a Zeiss Ultra 60 field emission scanning electron microscope (SEM) as well as FEI Titan S 80-300, Hitachi HF-3300, and JEOL 100 CX II transmission electron microscopes (TEMs). For TEM imaging, substrates were ultrasonicated in methanol for 15 min to remove Si nanowires from the growth substrate followed by dispersion of the resulting nanowire suspension onto lacey carbon Cu grids (Ted Pella).

4.4. Results and discussion

Si nanowires were grown on *in situ* cleaned Si(111) substrates with an evaporated Au catalyst and Si_2H_6 in an ultrahigh vacuum (UHV) chamber. A two-step procedure, consisting of incubation and elongation steps, maintains a constant areal density, as shown in Figure 4.1.[25]

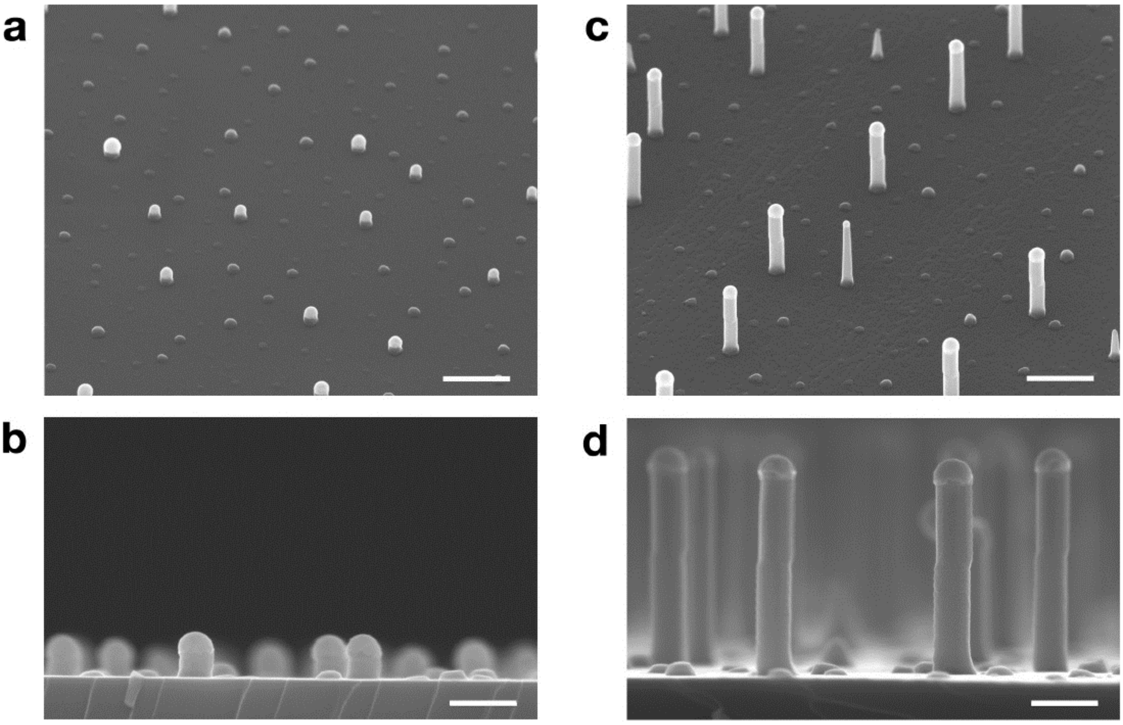

Figure 4.1: SEM images of Si nanowires synthesized via a two-step process. (a, b) Short Si "stubs" grown during the incubation step with a Si_2H_6 pressure of 2 × 10^{-4} Torr and a substrate temperature of 590 °C. (c, d) Si nanowires exhibiting one transverse {111} twin boundary (TB) after growth consisting of elongation at a Si_2H_6 pressure of 2 × 10^{-4} Torr and substrate temperature of 490 °C for 9 min, raising the Si_2H_6 pressure to 5 × 10^{-4} Torr and lowering the substrate temperature to 410 °C for 1 min, and subsequently returning to the original conditions for an additional 9 min. Scale bars: (a) 500 nm, (b) 200 nm, (c) 500 nm, and (d) 200 nm.

As shown in Figure 4.2a and as reported previously,[25,26] Si nanowires grow in the <111> direction with no appreciable defects when Si_2H_6 pressure and the substrate temperature are held at 2 × 10^{-4} Torr and 490 °C, respectively. Additional control experiments indicate that the nanowire elongation rate is 37.3 nm/min under these growth conditions, as shown in Figure 4.3.

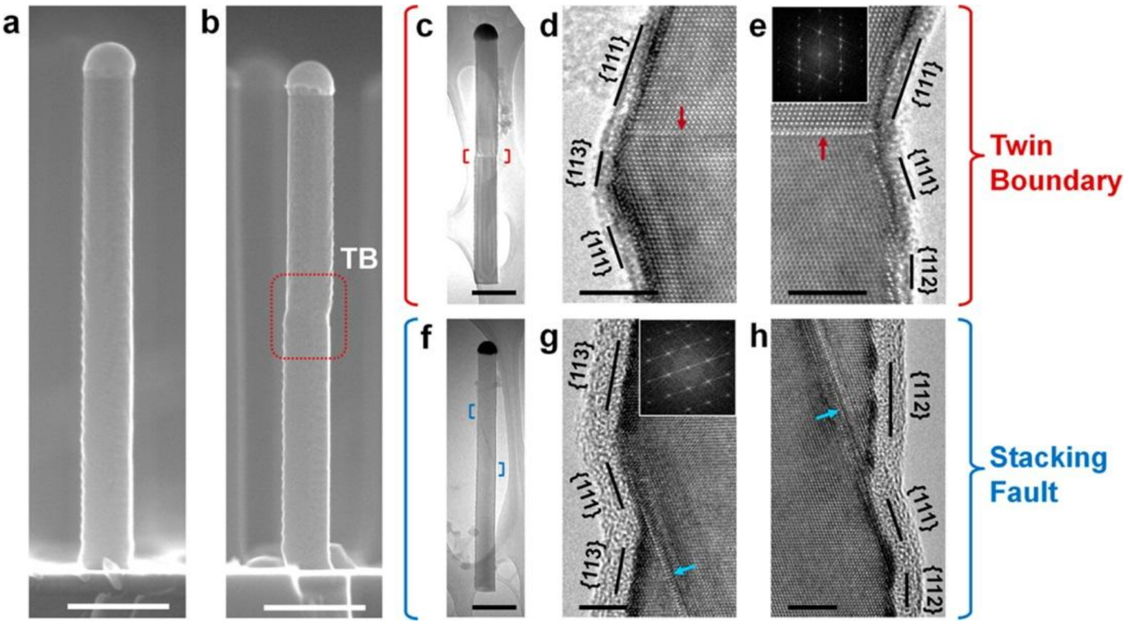

Figure 4.2: SEM and TEM images of Si nanowires containing either a transverse twin boundary (TB) or stacking fault (SF) near the midpoint. (a) SEM image showing a defect free Si nanowire grown by maintaining Si_2H_6 pressure at 2 × 10^{-4} Torr and substrate temperature at 490 °C for 38 min. (b) SEM image showing a Si nanowire with a clearly visible TB after growth at Si_2H_6 pressure of 2 × 10^{-4} Torr and substrate temperature of 490 °C for 17 min, followed by an increase of Si_2H_6 pressure to 5 × 10^{-4} Torr and lowering substrate temperature to 410 °C for 1 min, and then reverting to the original conditions for an additional 17 min. All SEM images are measured along the <110> direction to clearly show how the saw-tooth faceting changes after the TB. Scale bars: 200 nm. Bright-field TEM images of representative Si nanowires containing a single (c) TB or (f) SF. Scale bars: 200 nm. (d, e) High resolution bright-field TEM images showing the sidewall structure near the TB. Inset: FFT confirming the existence of a TB. Scale bars: 4 nm. (g, h) High resolution bright-field TEM images showing the sidewall structure nearby a SF. Inset: FFT confirming that the defect is a SF. Scale bars: 5 nm. All TEM images are measured along the [110] zone axis.

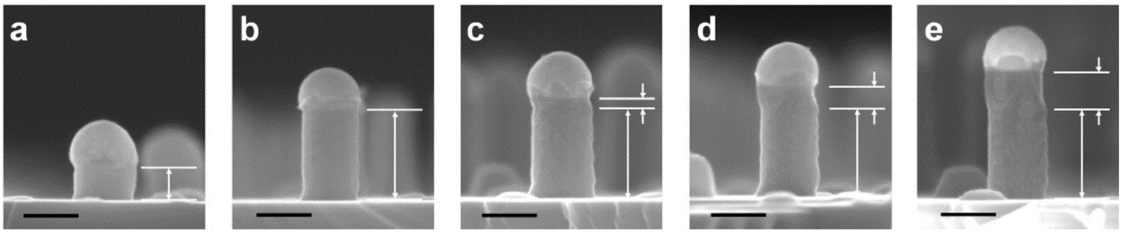

Figure 4.3: SEM images showing the evolution of the TB, sidewall morphology, and contact angle as a function of growth time. (a) Si “stub” synthesized with the standard incubation step conditions for 2 min. (b) Si nanowire following an elongation step with a Si_2H_6 pressure of 2 × 10^{-4} Torr and substrate temperature of 490 °C for 3 min. Si nanowires synthesized with the same conditions as (b), but followed by an

additional (c) 1 min, (d) 2 min (d) or 4 min (e) at a Si_2H_6 pressure of 5 × 10^{-4} Torr and substrate temperature of 410 °C. Note the change in contact angle visible in (c). The growth rate with a Si_2H_6 pressure of 2 × 10^{-4} Torr and substrate temperature of 490 °C is 37.3 nm/min whereas it slows to 18 nm/min with a Si_2H_6 pressure of 5 × 10^{-4} Torr and substrate temperature of 410 °C. Scale bars: 100 nm.

The situation is dramatically different if the growth conditions are abruptly modulated. When the Si_2H_6 pressure increases from 2 × 10^{-4} to 5 × 10^{-4} Torr and the substrate temperature decreases from 490 to 410 °C at the midpoint of nanowire elongation, before being returned to the original conditions after 1 min, we observe transverse {111} TBs (Figure 4.2b-e) or angled (19.5° from the <111> direction) {111} SFs (Figure 4.2f-h). It is important to note that this partial pressure and substrate temperature range is chosen to minimize nanowire kinking (Figure 4.4).

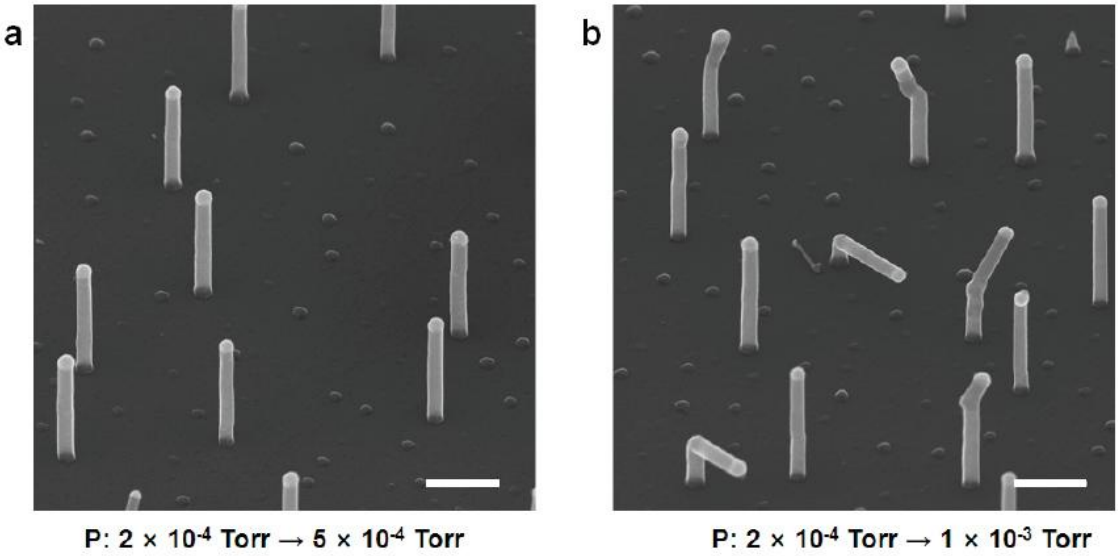

Figure 4.4: SEM images showing that kinking increases for larger pressures. (a) Nanowires grown using the same procedure as the nanowires shown in Figure 4.7. (b) Nanowires grown with the same procedure as Figure 4.7, but with a larger pressure increase (i.e. 2 × 10^{-4} Torr to 1 × 10^{-3} Torr) at each condition change. Scale bars: 500 nm.

While transmission electron microscopy (TEM) images confirm the presence of TBs and SFs, the characteristic sawtooth faceting[27] of Si nanowires enable facile observation of TBs with scanning electron microscopy (SEM). Due to the three-fold symmetry of the nanowire cross-section and 60°, or equivalently 180°, lattice rotation that takes place at the TB, sawtooth faceting appears to switch sides when viewed along the <110> direction (Figure 4.2b).[22] Nanowire growth with a Si_2H_6 pressure and substrate temperature equivalent to that during the 1 min condition change indicates that the elongation rate is approximately 18 nm/min (Figure 4.3) during this time.

High-resolution TEM (HR-TEM) images and associated Fast Fourier Transforms (FFTs) provide additional insight into these defects. Foremost, a classic double diffraction (inset, Figure 4.2e) confirms that the transverse defect is a TB. As expected, the narrow {112} sidewall is sawtooth faceted, consisting of alternating {111} and {113} planes.[27] The sawtooth faceting seen on this sidewall continues until the transverse TB appears, after which a {111} facet emerges (Figure 4.2d). Although the broad {112} sidewall is comparatively flat, {111} facets appear immediately before and after the TB (Figure 4.2e). Importantly, and as discussed in detail below, these inward facing {111} facets appear without exception immediately prior to the TB, as shown in Figure 4.5.

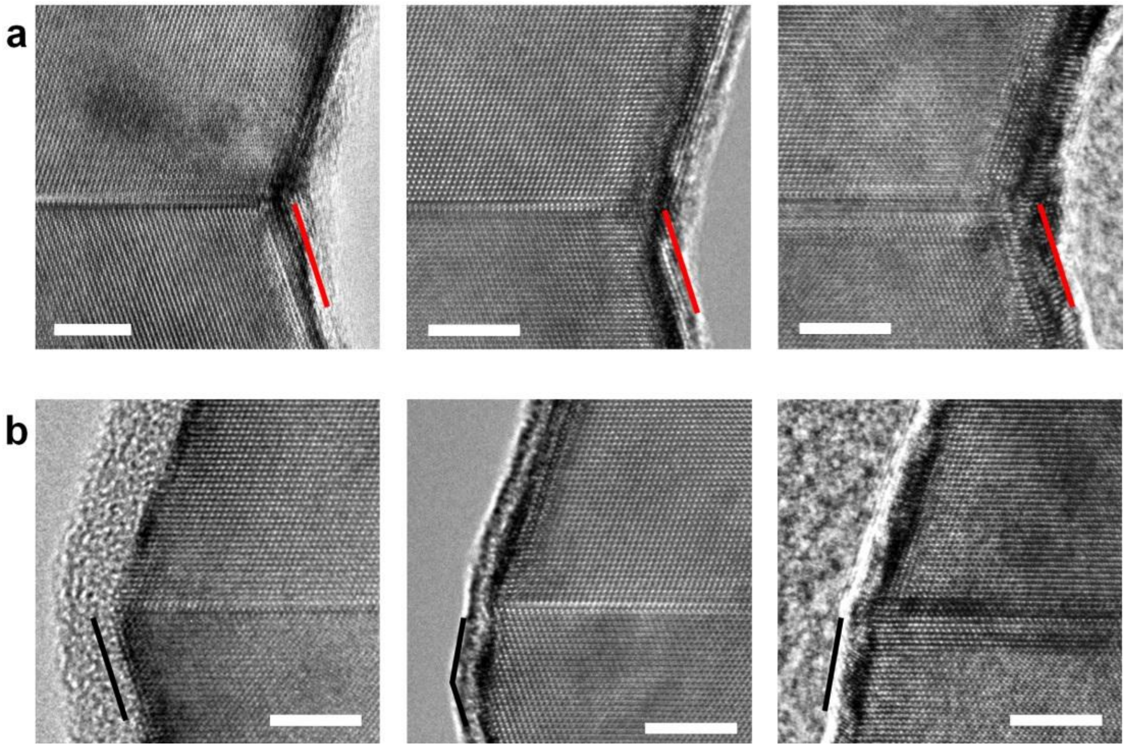

Figure 4.5: High resolution bright-field TEM images along the [110] zone axis of Si nanowire sidewalls near multiple transverse {111} TBs. (a) Images of the broad {112} sidewalls show that inward {111} facets (highlighted by red lines) appear before all TBs. (b) Images of the narrow {112} sidewalls reveal that sawtooth facets (highlighted by black lines) are present prior to the TB, whereas a {111} facet emerges after the TB. Scale bars: 5 nm.

SFs always initiate at the broad {112} sidewall (Figure 4.2h) and terminate at the opposite sawtooth faceted sidewall (Figure 4.2g). The FFT pattern (inset, Figure 4.2g) confirms that SFs are {111} planes and propagate in the <112> direction. The sidewalls near the SF sometimes, but not always, exhibit inward {111} facets similar to those near the TB (Figure 4.6).

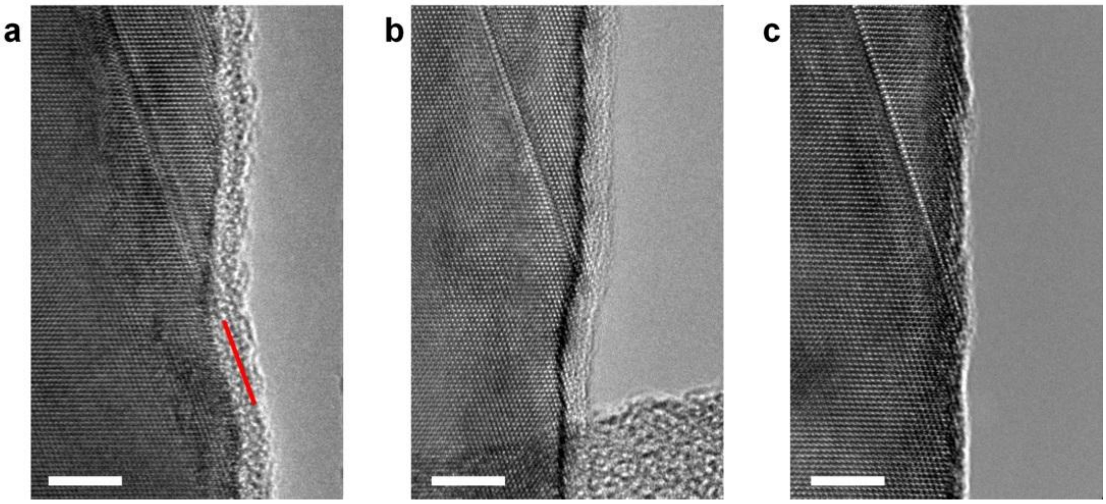

Figure 4.6: High resolution bright-field TEM images along the [110] zone axis of Si nanowire sidewalls showing SFs (a) with (highlighted by a red line) and (b, c) without clear {111} facets immediately prior to defect generation. Scale bars: 5 nm.

To definitively connect defect initiation with the user-defined Si_2H_6 pressure increase and substrate temperature decrease, we completed a series of experiments where the same condition change was applied at multiple points during nanowire growth. Figure 4.7 shows representative nanowires that result from 4 distinct condition changes, each spaced by 7 min. For the reasons mentioned above, transverse TB position, sometimes several in a single nanowire, can be readily identified via SEM (Figure 4.7a). Importantly, we only observe TBs at positions that correspond to the growth condition change. However, we do not observe a TB in every nanowire at every condition change. Additional experiments with condition change intervals of 5 min – 11 min – 5 min and 9 min – 3 min – 9 min confirm that the defects only result from changing growth conditions (Figure 4.8). The same changes to growth conditions also generate SFs (Figure 4.9). To accurately measure SF position via TEM, we increased the time intervals to 10 min – 10 min – 10 min, 15 min – 15 min – 15 min, and 20 min – 20 min – 20 min. Although SF introduction also correlates with changes to growth conditions, the insertion position exhibits more variability than was observed for TBs. We attribute some of the variability for SFs to the uncertain tilt angle on nanowires resting on a TEM grid, but also suspect that the defect generation mechanism plays a role (*vide infra*).

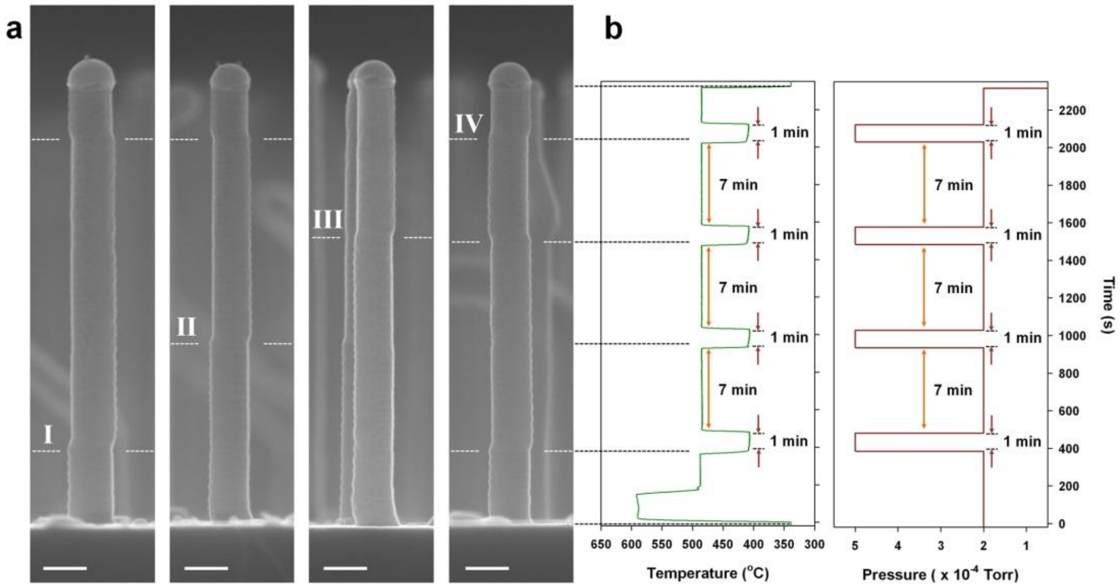

Figure 4.7: Correlation between TB position and growth condition changes. (a) SEM images of representative Si nanowires containing TBs at different axial positions. Si nanowires were grown with a Si_2H_6 pressure of 2×10^{-4} Torr and substrate temperature of 490 °C for the first 3 min followed by a series of condition changes, where the Si_2H_6 pressure is raised to 5×10^{-4} Torr and the substrate temperature is reduced to 410 °C for 1 min. This experiment consisted of four sets of pressure and temperature changes, each spaced by 7 min, as shown in (b). TB position is designated by the Roman numerals I, II, III, and IV, which correspond to each of the four condition changes. Scale bars: 100 nm. (b) Substrate temperature and Si_2H_6 pressure profile during the nanowire growth. The temperature profile is data collected by an infrared pyrometer with a 340 °C temperature cut-off. The pressure profile is schematically illustrated for comparison purposes.

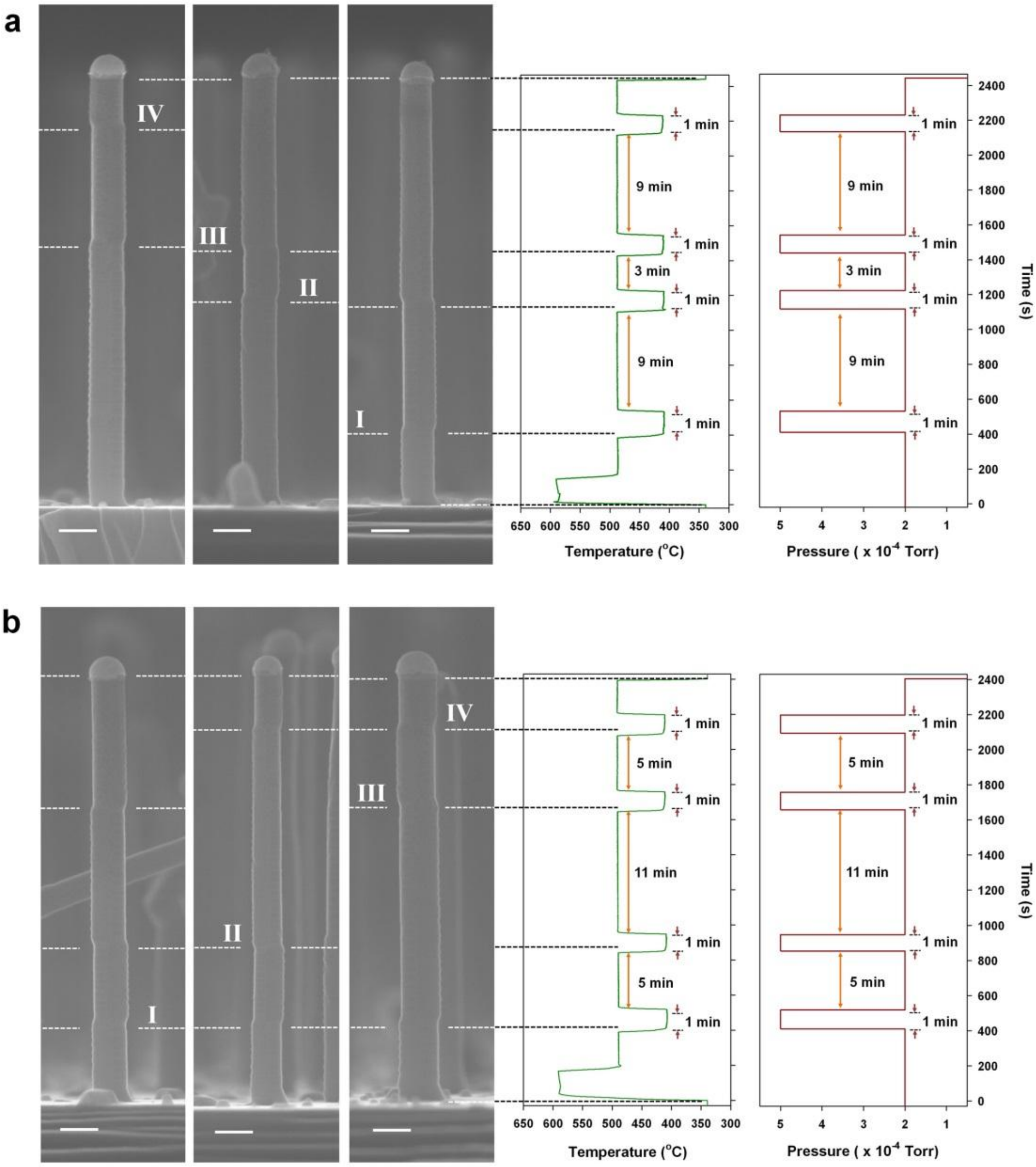

Figure 4.8: SEM images of representative Si nanowires containing TBs at different axial positions. Si nanowires were grown with a Si_2H_6 pressure of 2 × 10^{-4} Torr and substrate temperature of 490 °C for the first 3 min followed by a series of condition changes, where the Si_2H_6 pressure is raised to 5 × 10^{-4} Torr and the substrate temperature is reduced to 410 °C for 1 min. The overall growth procedure was identical to that shown in Figure 4.7, except for the time interval between each condition change: (a) 9 min – 3 min – 9 min and (b) 5 min – 11 min – 5 min. Scale bars: 100 nm.

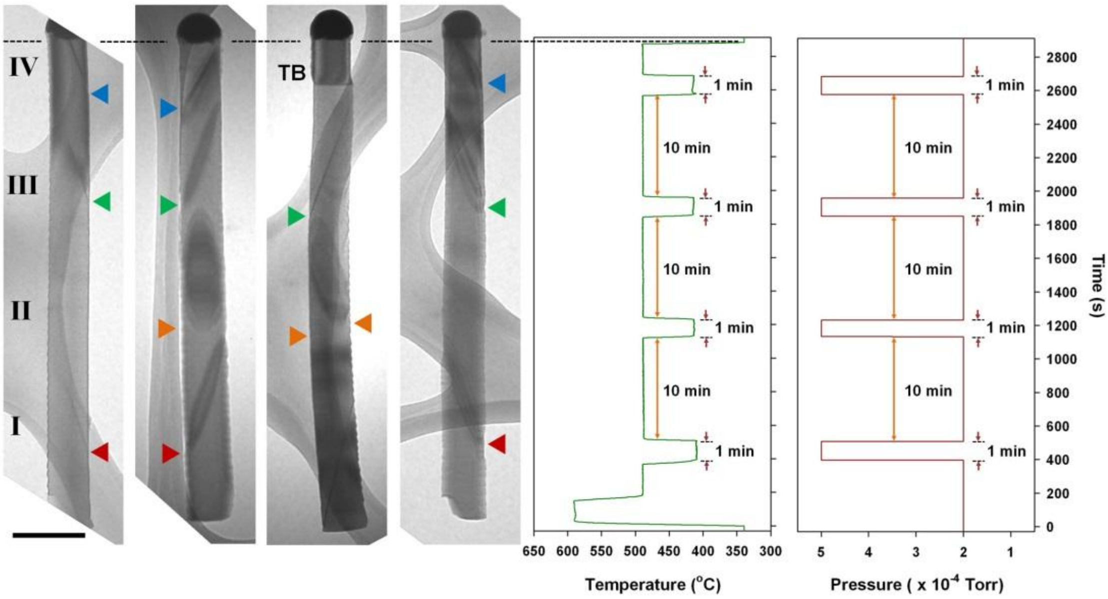

Figure 4.9: Bright-field TEM images of representative Si nanowires containing SFs at different axial positions. Si nanowires were grown with a Si_2H_6 pressure of 2×10^{-4} Torr and substrate temperature of 490 °C for the first 3 min followed by a series of condition changes, where the Si_2H_6 pressure is raised to 5×10^{-4} Torr and the substrate temperature is reduced to 410 °C for 1 min. This experiment consisted of four sets of pressure and temperature changes, each spaced by 10 min. SFs and TBs are sometimes observed simultaneous as denoted by 'TB' in the figure. Scale bars: 200 nm.

Figures 4.10a and 4.10b summarize our data for the average TB or SF axial position (relative to the catalyst tip) for many Si nanowires as a function of time interval between condition changes (Figure 4.11). The strong correlation between inter-defect distance and time interval supports our assertion that defects result from the user-applied growth condition change. We note that the inter-defect distance for TBs and SFs is diameter independent in the range of 70 to 110 nm (Figure 4.11). As shown in Figure 4.10c, there is no strong axial preference for defect formation.

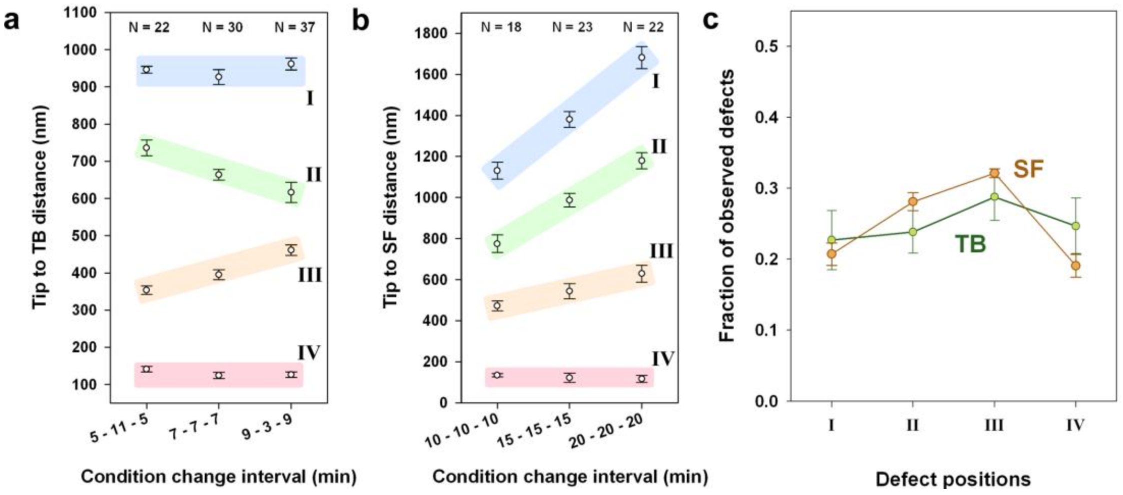

Figure 4.10: Average position and associated standard deviation for (a) TBs and (b) SFs as a function of different condition change intervals, as compiled from the data shown in Figure 4.11. These statistics are compiled from *N* nanowires that each exhibit at least one defect plane. The Roman numerals correspond to each condition change, beginning with that closest to the substrate. (c) Of those nanowires showing at least one defect, the fraction of defects appearing at positions that correspond to condition change I, II, III, or IV. These statistics are compiled from 157 TBs and 131 SFs sources from all of their respective interval experiments.

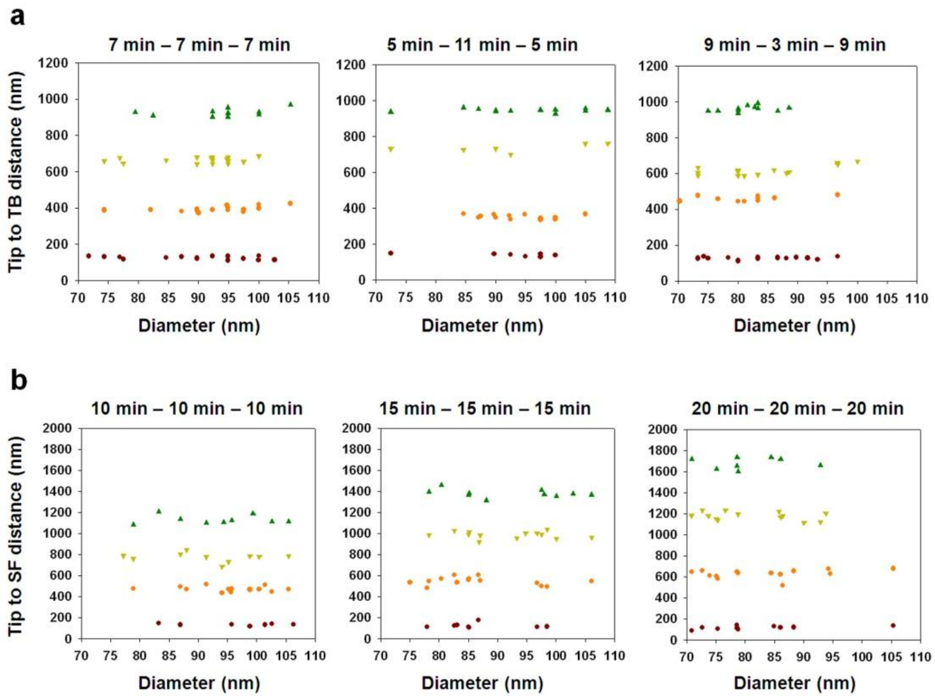

Figure 4.11: Distribution of (a) TB and (b) SF positions in Si nanowires grown with a Si_2H_6 pressure of 2 × 10^{-4} Torr and substrate temperature of 490 °C for the first 3 min followed by a series of condition changes, with intervals as indicated, where the Si_2H_6 pressure is raised to 5 × 10^{-4} Torr and the substrate

temperature is reduced to 410 °C for 1 min. TB and SF position determined via SEM and TEM, respectively.

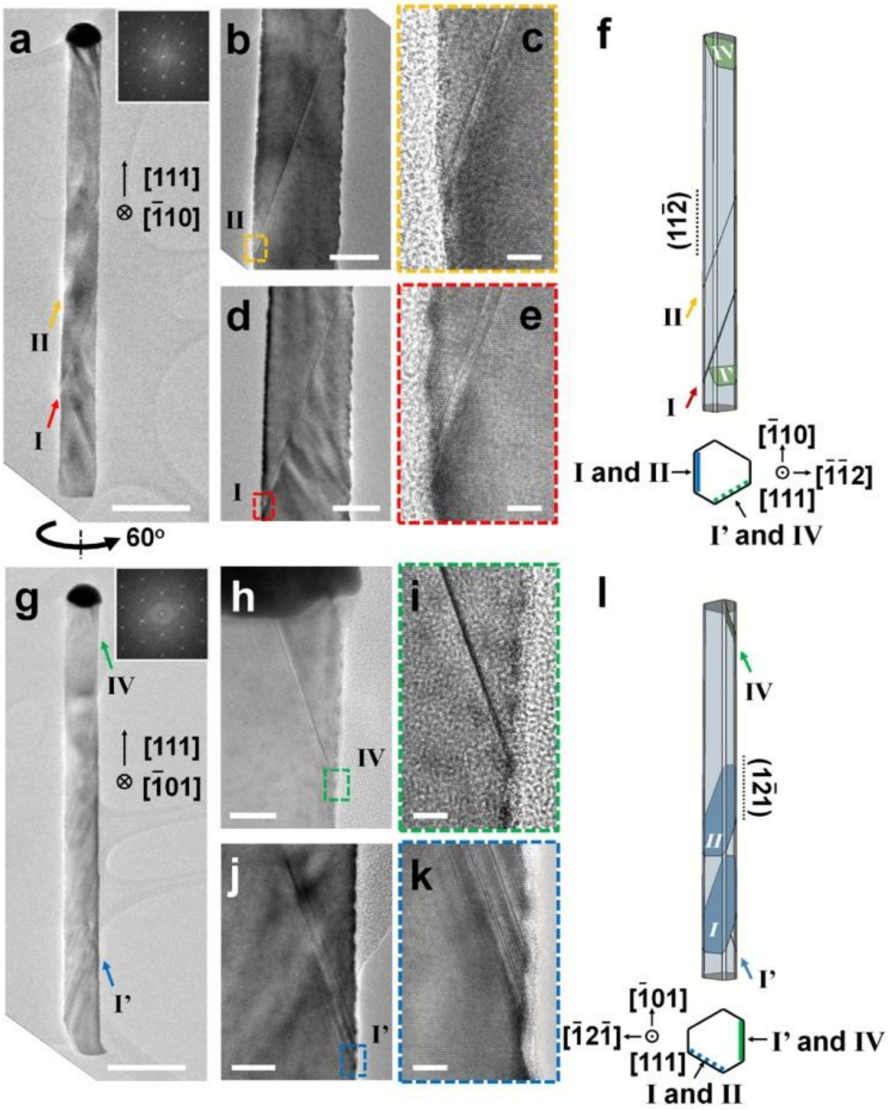

Figure 4.12: SFs can initiate from different sidewalls within the same Si nanowire. (a-f) SF I and II initiate from the $(11\bar{2})$ sidewall, whereas (g-l) SF I’ and IV initiate from the $(1\bar{2}1)$ sidewall. A comparison of FFT insets (a,g) demonstrates that the nanowire has been rotated 60° around the <111> axis. Examination of the TEM grid confirms that all images result from the same nanowire. (b, d) Bright-field TEM images along the $[\bar{1}10]$ zone axis showing that SF I and II both initiate at the $(11\bar{2})$ sidewall and both terminate at the $(\bar{1}\bar{1}2)$ sidewall. (h, j) Bright-field TEM images along the $[\bar{1}01]$ zone axis showing that SF I’ and IV both initiate from the $(1\bar{2}1)$ sidewall. SF I’ terminates in the nanowire core while SF IV terminates at the liquid-solid interface. (c, e, i, k) High resolution bright-field TEM images of SF I, II, I’ and IV. (f, l) Schematic illustration of the as observed SFs. Scale bars: (a, g) 200 nm, (b, d) 50 nm, (h, j) 20 nm, and (c, e, i, k) 5 nm.

Our data also shows that SFs can initiate from different sidewalls in the same Si nanowire. Figure 4.12 displays TEM images measured along different <110> zone axes for a representative Si nanowire grown with the procedure used for the nanowires in Figure 4.7. Two SFs (labeled I and II), originating from the $(11\bar{2})$ sidewall, are evident when the nanowire is viewed along the $[\bar{1}10]$ zone axis (Figure 4.12a-f). However, two different SFs (labeled I' and IV), initiating from the $(1\bar{2}1)$ sidewall, appear when the nanowire is rotated 60° to the $[\bar{1}01]$ zone axis (Figure 4g-l). Diffraction patterns (insets, Figure 4.12a and 4.12g) confirm the 60° rotation around the nanowire axis. These data indicate that SF initiation can occur at any of geometrically similar, broad {112} sidewalls: $(11\bar{2})$, $(1\bar{2}1)$, and $(\bar{2}11)$. Moreover, the condition change can initiate SFs from different {112} sidewalls at the same axial position, as shown for SF I and I'. While SF I propagates across the entire nanowire, SF I' terminates partway into the nanowire core. The termination of SF I' likely occurs when these defect planes intersect, but a complete analysis of this phenomenon is beyond the scope of the present work. We also identify a range of distinct SF types: single extrinsic SF (Figure 4.13) as well as SFs comprised of different numbers of closely spaced twin planes (Figure 4.12e, 4.12k). Since SFs can begin at any of the broad {112} sidewalls, many SFs are invisible when viewing a nanowire along a single zone axis.

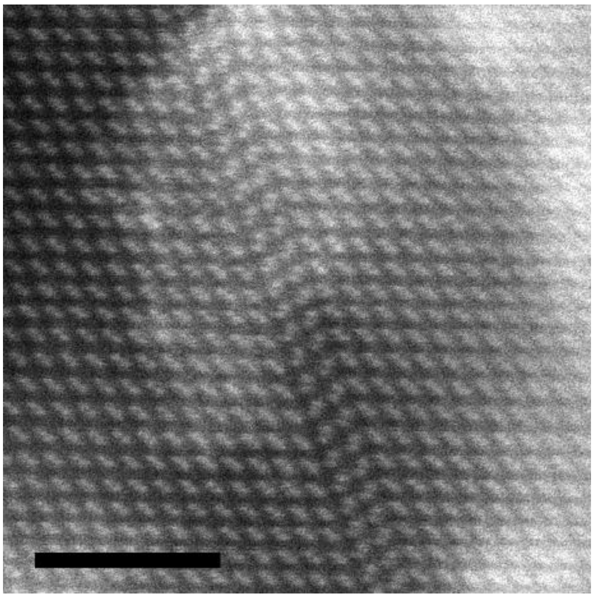

Figure 4.13: Dark-field STEM image confirming the presence of an extrinsic stacking fault inside a representative Si nanowire. Scale bar: 2 nm.

We now address the efficiency of defect introduction at each condition change, which we define as:

$$\eta = \frac{N_\mathrm{D}}{N_\mathrm{NW}\chi}$$

where N_D is the total number of defects, N_NW is the total number of nanowires examined, and χ is the number of condition changes. This equation is valid for situations where the probability of forming a defect does not depend on axial position (Figure 4.10c). Transverse TB introduction efficiency, η_TB, is easily assessed since the sidewall morphology change (i.e. appearance of sawtooth facets on the opposite side of the nanowire when viewed along the <110> direction) is clearly visible in the SEM (Figure 4.2b). We find a total of 114 transverse TBs (N_D) in 766 nanowires (N_NW) that underwent 4 condition changes (χ) with 7 min time intervals, which yields a transverse TB introduction efficiency of 3.7%. While transverse TB introduction efficiency is low, a topic we return to below, the SF introduction efficiency, η_{SF}, is substantially higher. A TEM analysis of 17 nanowires (N_{NW}) with the same, four condition change sequence as the TBs counted above shows 40 SFs, which corresponds to a SF introduction efficiency of at least 59% (Figure 4.14). Importantly, this value is a lower bound since the propagation direction/orientation relative to the viewing direction for some SFs (Figure 4.12) likely obscures their presence. While improvements are clearly possible, η_{TB} and η_{SF} are sufficiently large to identify nanowires exhibiting both TB and SF superstructures as shown in Figures 4.15a and 4.15b, respectively.

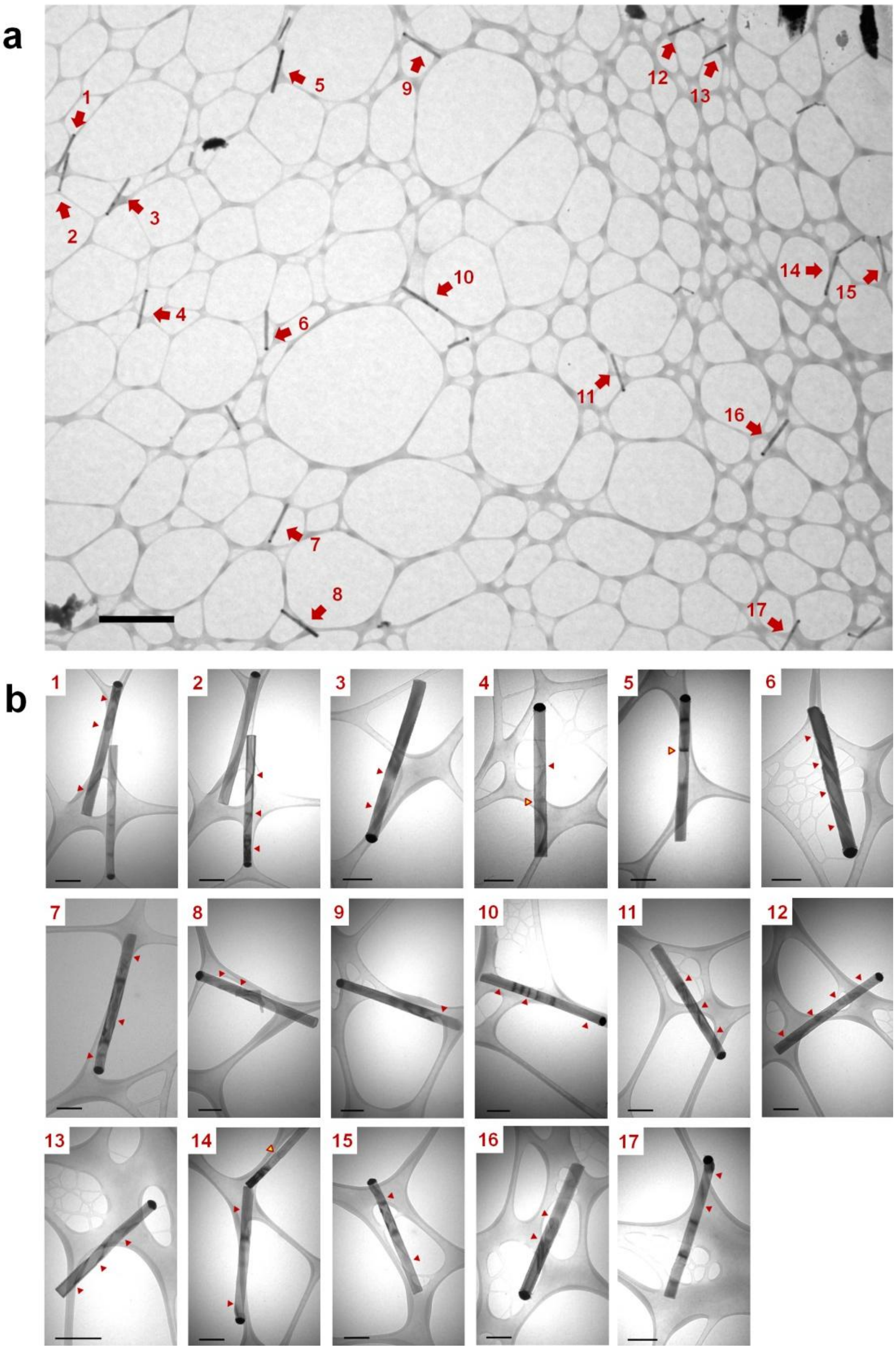

Figure 4.14: Bright-field TEM images showing Si nanowires from a 7 min – 7 min – 7 min time interval experiment that was used to determine SF introduction efficiency. (a) Low magnification image of 17 nanowires distributed on a single lacey carbon grid. Scale bar: 2 μm. (b) Higher magnification images of each nanowire in (a). Angled SFs and transverse TBs are marked by red and yellow triangles, respectively. 40 SFs (and 2 TBs) are observed from these 17 nanowires, which yields a SF introduction efficiency (η_{SF}) of 59%. The TB introduction efficiency (η_{TB}) as determined from these nanowires is 3%, which is consistent with the analysis of SEM images. Scale bars: 200 nm.

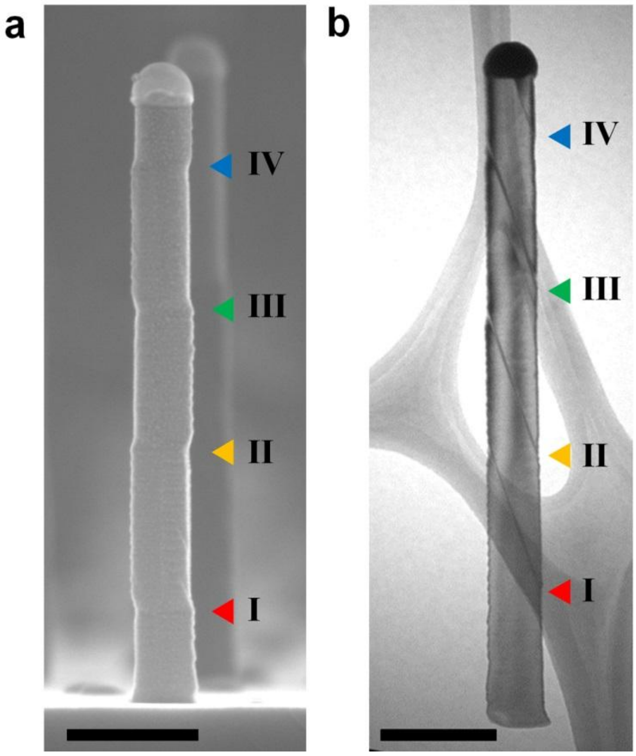

Figure 4.15: Demonstration of defect superstructures. (a) SEM image of a Si nanowire exhibiting a TB superstructure and (b) a bright-field TEM image along the [110] zone axis showing a Si nanowire with a SF superstructure. Scale bars: 200 nm.

A number of models have been developed to explain defect generation in VLS synthesized semiconductor nanowires. For the case of transverse {111} TBs in III-V nanowires, Algra *et al*. proposed that changes to catalyst supersaturation[28] and the catalyst liquid-vapor interface energy,[29] which modify the triple-phase line, are responsible for increasing the probability of defect nucleation. Dayeh *et al*. invoke a similar argument, that increases in supersaturation enhance the probability of faulted adatom stacking, to explain the appearance of angled {111} SFs in Si[11] and GaAs[30] nanowires. We note that Dayeh and coworkers do not observe transverse {111} TBs in their nanowires. An analysis by Davidson *et al*. suggests that the low contact angle for the Au-Si and Au-Ge system precludes transverse {111} TB formation in group IV nanowires.[10]

Our findings suggest that TB and SF formation is influenced by changes to solid-vapor interface chemistry near the triple-phase line, which occurs upon modulation of growth conditions. This mechanism is motivated by our report in the previous chapter of surface chemistry induced "kinking" in Si nanowires where we show via real-time *in situ* infrared spectroscopy that very similar changes to growth conditions increase the quantity of adsorbed hydrogen atoms on the Si nanowire sidewall.[25] Hydrogen atoms accumulate near the triple-phase line because the Si_2H_6 delivery rate increases and the H_2 desorption rate decreases as the Si_2H_6 pressure increases and the substrate temperature decreases, respectively. Although infrared spectra are challenging to acquire over the course of the 1 min condition changes applied in the present study, two pieces of indirect evidence provide additional support for a mechanism driven by surface chemistry. Foremost, SFs appear when we expose nanowires to additional hydrogen atoms (i.e. via cracking H_2 at a tungsten filament) while holding Si_2H_6 pressure and substrate temperature constant (Figure 4.16a). Dark-field imaging also shows a reduced Au coverage on the sidewall immediately following transverse TBs (Figure 4.16b), an observation which is consistent with the presence of adsorbed hydrogen.[31]

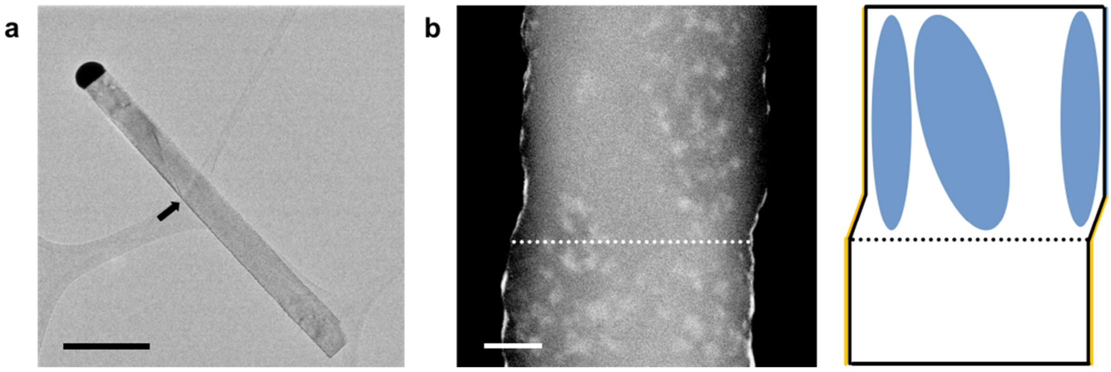

Figure 4.16: TEM evidence of the importance of surface hydrogen. (a) Bright-field image of a nanowire showing a SF (denoted by the black arrow) that appears following a 1 min exposure to hydrogen atoms without changing Si_2H_6 partial pressure (1×10^{-4} Torr) or substrate temperature (465 °C). Scale bar: 200 nm. (b) Dark-field image of a region near a transverse TB (denoted by the dotted white line) showing reduced Au coverage on the sidewall above the TB. Au appears as bright spots in the image. The blue shading in the schematic illustrates areas with reduced Au coverage. The narrow {112} sidewall after TB (i.e. upper right sidewall) also contains less Au when compared to the sidewalls prior to the TB (i.e. lower left and right sidewalls). Scale bar: 20 nm.

In the case of transverse TBs, we propose that condition change increases the local concentration of hydrogen atoms to a point where closed-packed {111} surfaces become favored. This behavior is fundamentally identical to the stabilization of distinct nanocrystal facets via addition of surfactant molecules.[32-34] We find that the length of this newly formed {111} facet can vary. Since all of our TEM images show the inward {111} facet prior to transverse TB formation (Figure 4.5a), the 3-fold symmetry of the Si nanowire cross-section implies that this structural feature simultaneously emerges from all three broad {112} sidewalls (i.e., $(11\bar{2})$, $(1\bar{2}1)$, and $(\bar{2}11)$). The narrow sidewalls, which exhibit sawtooth faceting, do not show such facet changes before the TB (Figure 4.5b).

The shape of the triple-phase line changes as the newly formed {111} facets elongate. This process is schematically illustrated in Figure 4.17c and is analogous to that previously proposed by Algra *et al*. to describe periodic twinning in III-V nanowires.[7] The triple-phase line becomes increasingly triangular and the Au-Si catalyst droplet undergoes a concomitant deformation as the {111} facets continue to grow. As long as the surface hydrogen concentration is maintained (i.e. during the 1 min condition change), this process continues until the triple-phase line reaches a critical point and a TB forms to lower the line tension. After the TB, the original inward moving {111} facets begin to propagate outward and the previously sawtooth faceted {112} sidewalls become inward moving {111} facets (Figure 4.2). The triple-phase line then returns to its original shape.

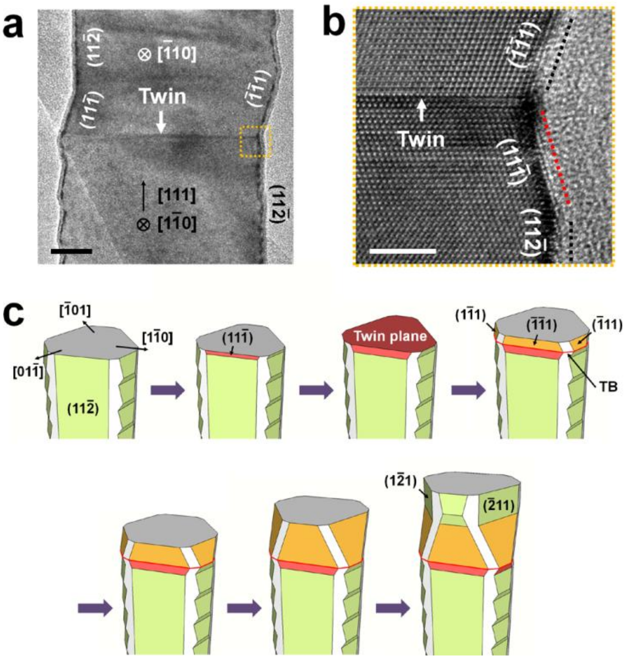

Figure 4.17: Transverse TB formation in Si nanowires. (a,b) Bright-field TEM images along the [110] zone axis showing a transverse TB. Scale bars: (a) 20 nm, (b) 4 nm. (c) Schematic illustration of the of the TB formation process. The nanowire is initially surrounded by 3 broad, flat {112} sidewalls and 3 narrow sidewalls that exhibit sawtooth faceting (shown in light green). {110} sidewalls also exist between each {112} sidewall (shown in white). Three new {111} facets (shown in red) emerge from the broad {112} sidewall at the onset of the each growth condition change. After the TB, the nanowire exhibits six {111} facets (shown in orange) that continue to propagate until {112} sidewalls remerge upon returning to the original growth conditions.

We observe that the {111} facets eventually revert back to their original {112} orientation (Figure 4.17a). Interestingly, Algra *et al.* also report a similar observation in their analysis of TBs in GaP nanowires grown under constant pressure and temperature.[28] In their report, they define the so-called "inversion length" as the distance from the TB to the point where the nanowire cross-section inverts and show that this parameter exhibits a linear dependence on diameter. Conversely, we observe an inversion length that is constant over the range of nanowire diameters studied here (Figure 4.18). We attribute this behavior to the fixed condition change time (i.e. 1 min) used in the present experiments, after which the Si_2H_6 pressure and substrate temperature revert to their original conditions (i.e. 2×10^{-4} Torr and 490 °C), and the {112} sidewalls reappear. The differences between the present work and Algra *et al.* provide evidence that the growth environment, rather than nanowire morphology (i.e. diameter) or crystal structure, is responsible for {111} facet formation and TB nucleation in the Si nanowire system. Furthermore, the transition from three to six {111} facets only at the TB suggest that there is a non-negligible barrier to {111} facet formation, but a complete understanding of this observation will require additional studies.

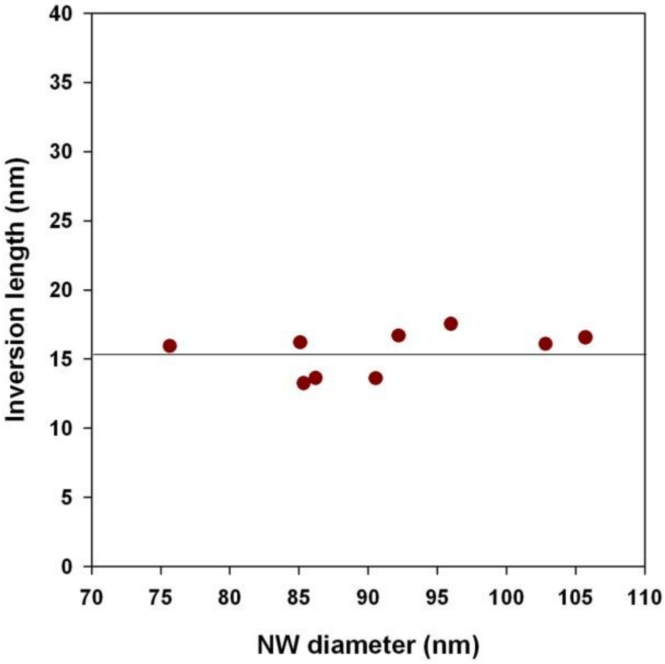

Figure 4.18: Distance from the transverse {111} TB to the point where the sidewall facets revert to {112} as a function of nanowire diameter. This distance, also known as the "inversion length," is 15.5 ± 1.5 nm and is independent of nanowire diameter.

The need for three {111} facets to simultaneously emerge from the broad {112} sidewalls prior to transverse TB appearance may explain why η_{TB} is low for Au-catalyzed Si nanowires. In particular, the sawtooth facets appearing on the narrow {112} sidewalls, which are a hallmark of this system, are not necessarily in phase.[27] This behavior leads to local differences in triple phase line shape and contact angle that likely prevents, or at least delays, {111} facet formation at one or more of the broad {112} sidewalls. When this occurs, transverse TBs are unlikely to form. In addition, sawtooth faceting also exhibits diameter-dependent periods[27] such that the triple-phase line shape and contact angle varies between nanowires, even at the same time point, in arrays synthesized from dewetted Au thin films. This effect is also expected to reduce the probability of transverse TB introduction. We anticipate that catalysts or precursors that yield a more consistent triple-phase line shape and contact angle will improve the probability of TB introduction upon each condition change.

The mechanism of SF formation is less clear. We observe that SFs, with a diversity of types (Figure 4.12) and sidewall morphologies (Figure 4.6), emerge as a result of the user-applied condition change. Importantly, the SF initiation point is more variable than for TBs (Figure 4.10) and indicates that the local conditions necessary for their formation are more easily achieved. While prior reports propose that changes to catalyst supersaturation are responsible for fault introduction,[11,15] our hydrogen atom exposure experiments (Figure 4.16a) indicate that surface chemistry also plays a role. Recent work indicates that changes to diameter may initiate defects as well.[35] Experiments to further elucidate the physical phenomena underlying SF generation are currently underway in our laboratory.

4.5. Conclusion

In conclusion, we demonstrate that user-defined changes to growth conditions permit the introduction of planar defects in Si nanowires. Transverse TBs, which are rarely observed during Au-catalyzed Si nanowire growth, and SFs were rationally generated for the first time. Our data suggests that surface chemistry plays a role in the defect generation process. We determine a lower bound on the overall defect introduction efficiency between 60 and 65% and expect that judicious choice of catalysts and precursor species will improve this value. Rational selection of defect type (i.e. TB or SF), which still remains challenging in III-V nanowires, is not yet possible for Si nanowires and will require additional insight into defect introduction mechanism. We expect that these results will open new routes to engineer defect superstructure and materials properties in Si nanowires specifically, and all semiconductor nanowires in general.

4.6. References

1. Akopian, N.; Patriarche, G.; Liu, L.; Harmand, J.-C.; Zwiller, V. *Nano Lett*. **2010**, *10*, 1198-1201.
2. Dayeh, S. A.; Susac, D. A.; Kavanagh, K. L.; Yu, E. T.; Wang, D. L. Adv. Func. Mater. **2009**, *19*, 2102-2108.
3. Hochbaum, A. I.; Chen, R.; Delgado, R. D.; Liang, W.; Garnett, E. C.; Najarian, M.; Majumdar, A.; Yang, P. *Nature* **2008**, *451*, 163-167.
4. Xiong, Q.; Wang, J.; Eklund, P. C. *Nano Lett*. **2006**, *6*, 2736-2742.
5. Johansson, J.; Karlsson, L. S.; Svensson, C. P. T.; Martensson, T.; Wacaser, B. A.; Deppert, K.; Samuelson, L.; Seifert, W., *Nat. Mater.* **2006**, *5*, 574-580.
6. Joyce, H. J.; Gao, Q.; Tan, H. H.; Jagadish, C.; Kim, Y.; Fickenscher, M. A.; Perera, S.; Hoang, T. B.; Smith, L. M.; Jackson, H. E.; Yarrison-Rice, J. M.; Zhang, X.; Zou, J., *Nano Lett.* **2009**, *9*, 695-701.
7. Algra, R. E.; Verheijen, M. A.; Borgstrom, M. T.; Feiner, L.-F.; Immink, G.; van Enckevort, W. J. P.; Vlieg, E.; Bakkers, E. P. A. M. *Nature* **2008**, *456*, 369-372.
8. Caroff, P.; Dick, K. A.; Johansson, J.; Messing, M. E.; Deppert, K.; Samuelson, L. *Nat. Nanotechnol.* **2009**, *4*, 50-55.
9. Dick, K. A.; Thelander, C.; Samuelson, L.; Caroff, P., *Nano Lett*. **2010**, *10*, 3494-3499.
10. Davidson, F. M.; Lee, D. C., III; Fanfair, D. D.; Korgel, B. A. *J. Phys. Chem. C* **2007**, *111*, 2929-2935.
11. Dayeh, S. A.; Wang, J.; Li, N.; Huang, J. Y.; Gin, A. V.; Picraux, S. T. *Nano Lett.* **2011**, *11*, 4200-4206.
12. Su, Z.; Dickinson, C.; Wan, Y.; Wang, Z.; Wang, Y.; Sha, J.; Zhou, W. *CrystEngComm* **2010**, *12*, 2793-2798.
13. Barth, S.; Boland, J. J.; Holmes, J. D. *Nano Lett*. **2011**, *11*, 1550-1555.
14. Fontcuberta i Morral, A.; Arbiol, J.; Prades, J. D.; Cirera, A.; Morante, J. R. *Adv. Mater.* **2007**, *19*, 1347-1351.
15. Lopez, F. J.; Givan, U.; Connell, J. G.; Lauhon, L. J. *Acs Nano* **2011**, *5*, 8958-8966.
16. den Hertog, M. I.; Cayron, C.; Gentile, P.; Dhalluin, F.; Oehler, F.; Baron, T.; Rouviere, J. L. *Nanotechnology* **2012**, *23*, 025701.
17. Hemesath, E. R.; Schreiber, D. K.; Kisielowski, C. F.; Petford-Long, A. K.; Lauhon, L. J. *Small* **2012**, *8*, 1717-1724.
18. Wang, Y.; Schmidt, V.; Senz, S.; Goesele, U. *Nat. Nanotechnol.* **2006**, *1*, 186-189.

19. Arbiol, J.; Fontcuberta i Morral, A.; Estrade, S.; Peiro, F.; Kalache, B.; Roca i Cabarrocas, P.; Ramon Morante, J., *J. Appl. Phys*. **2008**, *104*,064312.
20. Conesa-Boj, S.; Zardo, I.; Estrade, S.; Wei, L.; Alet, P. J.; Roca i Cabarrocas, P.; Morante, J. R.; Peiro, F.; Fontcuberta i Morral, A.; Arbiol, J. *Cryst. Growth Des.* **2010**, *10*, 1534-1543.
21. Iacopi, F.; Vereecken, P. M.; Schaekers, M.; Caymax, M.; Moelans, N.; Blanpain, B.; Richard, O.; Detavernier, C.; Griffiths, H. *Nanotechnology* **2007**, *18*, 505307.
22. Chou, Y.-C.; Wen, C.-Y.; Reuter, M. C.; Su, D.; Stach, E. A.; Ross, F. M. *Acs Nano* **2012**, *6*, 6407-6415.
23. Algra, R. E.; Hocevar, M.; Verheijen, M. A.; Zardo, I.; Immink, G. G. W.; van Enckevort, W. J. P.; Abstreiter, G.; Kouwenhoven, L. P.; Vlieg, E.; Bakkers, E. P. A. M. *Nano Lett*. **2011**, *11*, 1690-1694.
24. Takeuchi, S.; Suzuki, K. *Phys. Status Solidi A* **1999**, *171*, 99-103.
25. Shin, N.; Filler, M. A. *Nano Lett.* **2012**, *12*, 2865-2870.
26. Madras, P.; Dailey, E.; Drucker, J. *Nano Lett.* **2009**, *9*, 3826-3830.
27. Ross, F. M.; Tersoff, J.; Reuter, M. C. *Phys. Rev. Lett.* **2005**, 95, 146104.
28. Algra, R. E.; Verheijen, M. A.; Feiner, L.-F.; Immink, G. G. W.; Theissmann, R.; van Enckevort, W. J. P.; Vlieg, E.; Bakkers, E. P. A. M. *Nano Lett.* **2010**, *10*, 2349-2356.
29. Algra, R. E.; Verheijen, M. A.; Feiner, L. F.; Immink, G. G. W.; van Enckevort, W. J. P.; Vlieg, E.; Bakkers, E. *Nano Lett.* **2011**, *11*, 1259-1264.
30. Dayeh, S. A.; Liu, X. H.; Dai, X.; Huang, J. Y.; Picraux, S. T.; Soci, C. *Appl. Phys. Lett*. **2012**, *101*, 053121.
31. Oura, K.; Lifshits, V. G.; Saranin, A. A.; Zotov, A. V.; Katayama, M. *Surf. Sci. Rep*. **1999**, *35*, 1−69.
32. Manna, L.; Scher, E. C.; Alivisatos, A. P. *J. Am. Chem. Soc*. **2000**, *122*, 12700-12706.
33. Milliron, D. J.; Hughes, S. M.; Cui, Y.; Manna, L.; Li, J. B.; Wang, L. W.; Alivisatos, A. P. *Nature* **2004**, *430*, 190-195.
34. Yin, Y.; Alivisatos, A. P. *Nature* **2005**, *437*, 664-670.
35. Hillerich, K.; Dick, K. A.; Wen, C.-Y.; Reuter, M. C.; Kodambaka, S.; Ross, F. M. *Nano Lett.* **2013**, *13*, 903-908.

CHAPTER 5

SIDEWALL MORPHOLOGY-DEPENDENT FORMATION OF MULTIPLE TWINS IN SI NANOWIRES

5.1. Overview[†]

Precise placement of twin boundaries and stacking faults promises new opportunities to fundamentally manipulate the optical, electrical, and thermal properties of semiconductor nanowires. In this chapter, we report on the appearance of consecutive twin boundaries in Si nanowires and show that sidewall morphology governs their spacing. Detailed electron microscopy analysis reveals that thin {111} sidewall facets, which elongate following the first twin boundary (TB_1), are responsible for deforming the triple-phase line and favoring the formation of the second twin boundary (TB_2). While multiple, geometrically correlated defect planes are known in group III-V nanowires, there are no prior reports of this behavior in group IV materials.

5.2. Introduction

The manipulation of semiconductor nanowire properties is possible via control of crystal phase,[1] growth orientation,[2] and sidewall faceting,[3] among others.[4,5] Engineering of the bilayer stacking sequence is particularly intriguing, assuming a sufficient level of precision is ultimately achievable, as it offers direct access to a material's optoelectronic

---

[†] Reprinted with permission from Shin, N.; Chi, M.; Filler, M. A. *ACS Nano* **2013**, *7*, 8206-8213. Copyright 2013 American Chemical Society.

and phononic behavior.[6-8] To this end, twin boundaries (TBs) and stacking faults (SFs) have been extensively studied in group III-V nanowires synthesized via the vapor-liquid-solid (VLS) method.[9-11] Careful selection of process conditions and/or dopants now enables periodic sequences of TBs known as twinning superlattices.[12,13]

The frequency and morphology of defects in group IV nanowires, particularly Si, exhibit a number of well-known differences relative to their III-V counterparts. Longitudinal defects – those oriented parallel to the nanowire growth direction – are common in <112> oriented Si nanowires catalyzed by Au.[14-16] Catalysts other than Au (*e.g.* Cu, Ga, Au/Ag) are also known to randomly generate transverse TBs – those oriented perpendicular to the nanowire growth direction – in <111> oriented Si nanowires.[17-19] In Chapter 4, we showed that the rapid modulation of precursor pressure and substrate temperature can rationally introduce transverse TBs in Au-catalyzed Si nanowires.[20]

Here, we show that two transverse TBs, which exhibit a sidewall morphology-dependent spacing, are possible in <111> oriented Si nanowires. We find that the first TB appears upon raising the Si_2H_6 pressure and reducing the substrate temperature. When maintaining these new conditions for an extended period of time, a second TB sometimes appears at a geometry-dependent distance from the first. A detailed investigation of nanowire morphology reveals that the second TB is coincident with the appearance of thin {111} facets that propagate across the nanowire's {110} sidewall. Algra *et al.* reported on the presence of similar "twin pairs" in III-V nanowires,[21] but the situation in Si nanowires exhibits a number of important differences.

5.3. Experimental methods

Si nanowires were prepared in an UHV chamber with a base pressure of 3×10^{-10} Torr. Nanowire growth begins with an incubation step, where a flash-annealed Si (111) substrate covered with a 2 nm Au film is ramped to 590 °C and exposed to 2×10^{-4} Torr Si_2H_6 (Voltaix, 99.998%) for 2 min. The substrate temperature is subsequently lowered to 490 °C at a rate of 3 °C/s while maintaining a constant Si_2H_6 pressure. After 10 min of elongation at 490 °C and 2×10^{-4} Torr Si_2H_6, the the Si_2H_6 pressure is increased to 5×10^{-4} Torr and substrate temperature decreased to 410 °C at a rate of 8 °C/s. The growth is continued at these conditions for another 10 min. Nanowire sidewall morphologies are analyzed via a Zeiss Ultra 60 field emission scanning electron microscope (SEM). High resolution bright-field transmission electron microscopy (TEM) and aberration-corrected high angle annular dark-field scanning transmission electron microscopy (HAADF-STEM) images are obtained with a FEI Titan S 80-300 microscope. Samples for TEM analysis are prepared via substrate ultrasonication in isopropyl alcohol (Sigma Aldrich) for 15 min and subsequent dispersion of the resulting nanowire suspension onto lacey carbon grids (Ted Pella).

5.4. Results and discussion

Figure 5.1a shows representative scanning electron microscopy (SEM) images of <111> oriented Si nanowires containing double TBs, which appear upon increasing the Si_2H_6 pressure from 2×10^{-4} to 5×10^{-4} Torr and lowering the substrate temperature from 490 to 410 °C. The new process conditions are applied after 10 min of initial elongation and maintained for another 10 min. While nanowire diameter ranges from 70 to 130 nm, the growth rate is diameter independent.[22]

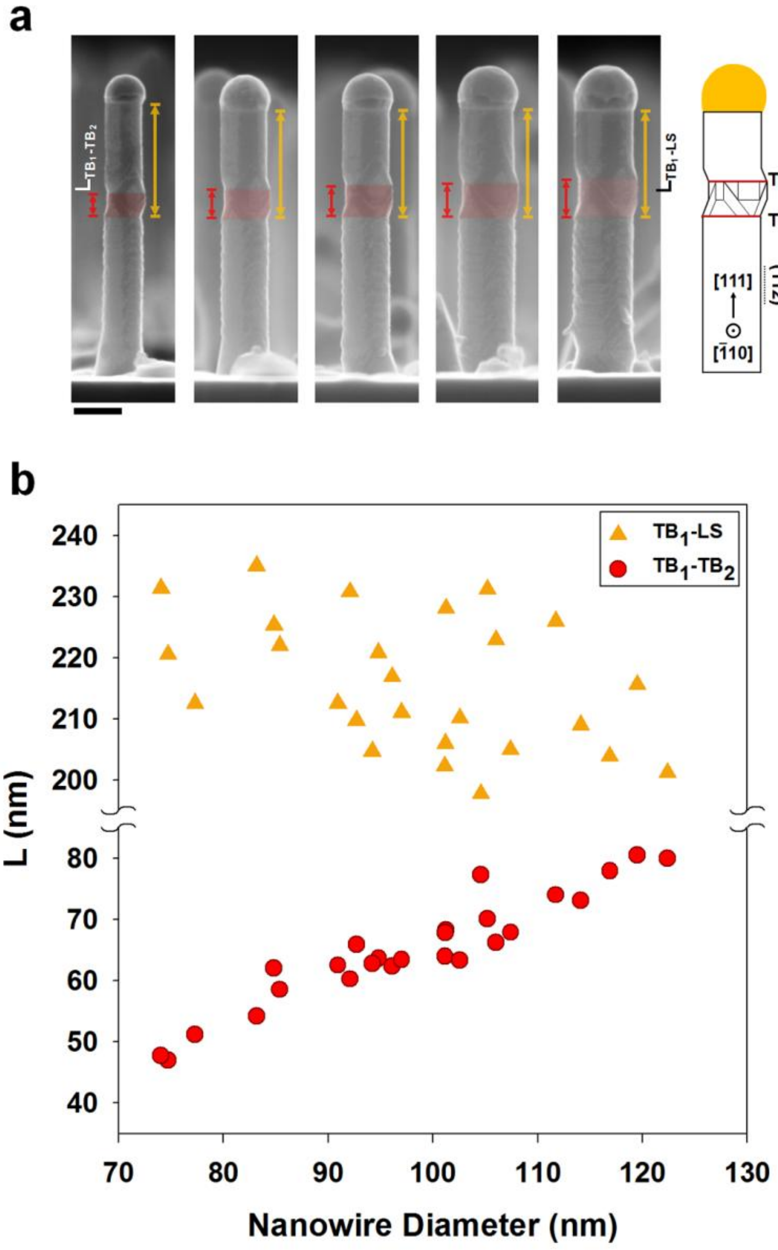

Figure 5.1: (a) Side view SEM images of representative Si nanowires with a range of diameters measured along the <110> direction that show changes to sidewall morphology near double TBs. A schematic projection of a nanowire containing double TBs onto the $(\bar{1}10)$ plane is included for comparison purposes. $L_{TB_1-TB_2}$ is indicated by red lines and defined as the distance between the first (TB$_1$) and second (TB$_2$) TB. The distance between TB$_1$ and the catalyst-nanowire interface is defined as L_{TB_1-LS} and indicated with

orange lines. Scale bar: 100 nm. (b) The values of $L_{TB_1-TB_2}$ and L_{TB_1-LS}, as determined from SEM images of 26 nanowires containing double TBs, plotted as a function of nanowire diameter.

As the nanowires are imaged along the <110> direction, the characteristic sawtooth faceting of the {112} sidewalls[23] is visible on the left side of each nanowire and provides an initial indication of the first TB's position (denoted TB_1). We note that the axial position of TB_1 is similar for all nanowires and independent of diameter, which indicates that it formed upon changing process conditions.[20] While maintaining the conditions at 5×10^{-4} Torr and 410 °C, a second TB (denoted TB_2) can also appear at some axial distance after TB_1. We identified 161 and 26 nanowires containing single (*i.e.* TB_1 only) and double TBs (*i.e.* TB_1 and TB_2), respectively, from a total of 1055 examined nanowires. Thus, the probability of TB_2 appearing after TB_1 is 13.9%. While this probability is clearly low, and not yet appropriate for defect superstructure engineering, the geometric relationship described herein provides important insight into the defect introduction mechanism in Si nanowires.

The distance between TB_1 and the liquid-solid (*i.e.* catalyst-nanowire) interface, defined as L_{TB_1-LS} and shown as orange lines in Figure 5.1a, is plotted as a function of nanowire diameter in Figure 5.1b. Since TB_1 forms upon raising Si_2H_6 pressure and lowering substrate temperature,[20] L_{TB_1-LS} represents the portion of the nanowire grown after the condition change and, as is evident from the plot, the growth rate (~22 nm/min) remains largely diameter-independent over this length. We also define $L_{TB_1-TB_2}$, indicated by the red lines in Figure 5.1a, as the distance between TB_1 and TB_2. Figure 5.1b shows $L_{TB_1-TB_2}$ plotted as a function nanowire diameter and reveals a clear diameter-dependence. TB_2 nucleates earlier in nanowires with small diameters and later in nanowires with large diameters. Since the process conditions are fixed following TB_1, the observed diameter-dependence of TB_2 position suggests that it forms due to a geometric effect. We return to this point below.

High-resolution transmission electron microscopy (HRTEM) images, measured along the <110> zone axis of a representative Si nanowire with a double TB are displayed in Figure 5.2.

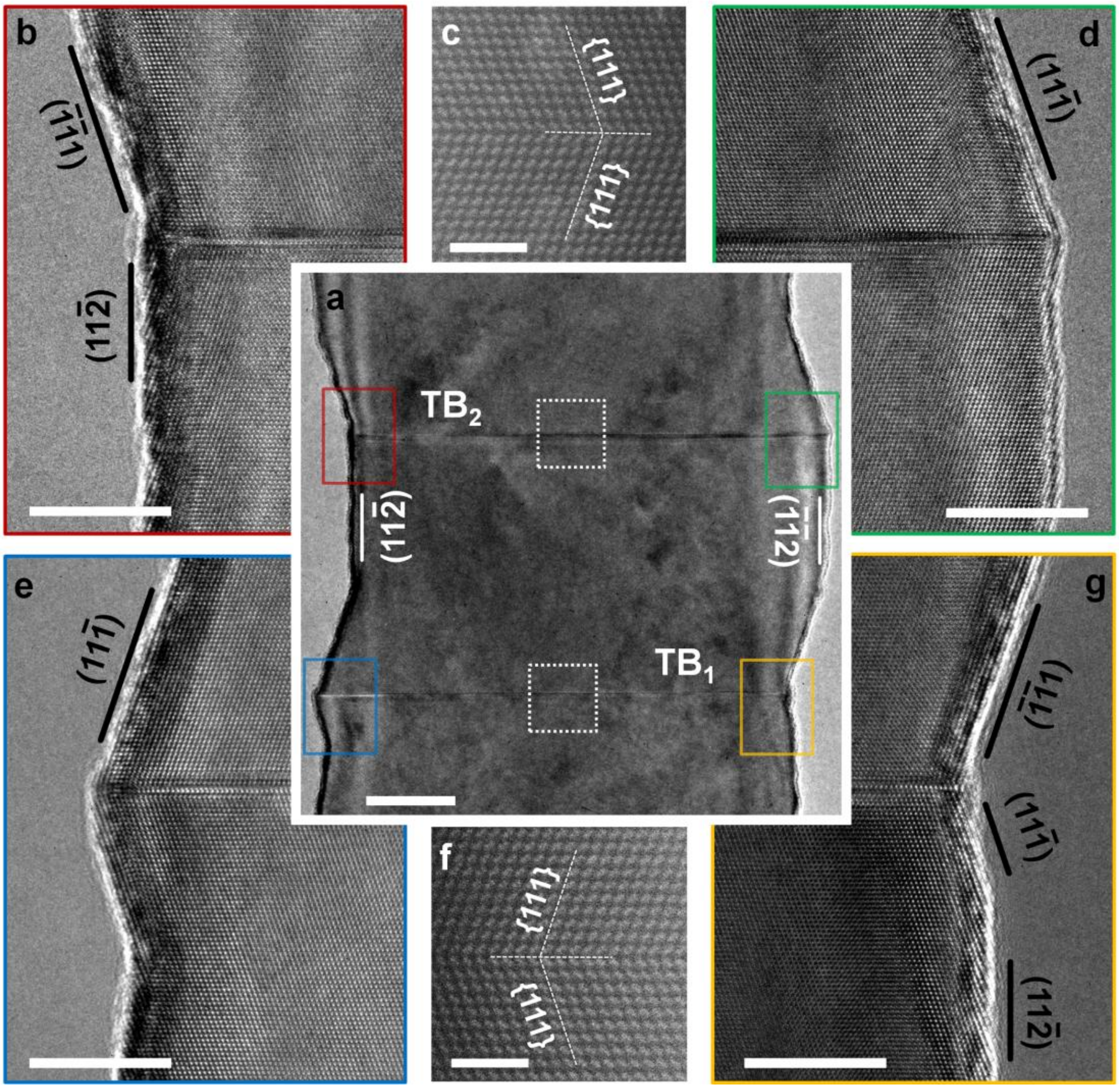

Figure 5.2: Representative TEM images of the region near double TBs in Si nanowires measured along the [$\bar{1}10$] zone axis. (a) Low-magnification bright-field image showing the overall structure of a double TB. Scale bar: 20 nm. High resolution bright-field images of the region inside the colored boxes in (a) and corresponding to the left and right side of (b, d) TB$_2$ and (e, g) TB$_1$. Scale bars: 10 nm. (c, f) Aberration-corrected HAADF-STEM images of (c) TB$_2$ and (f) TB$_1$ measured in the regions denoted by the dotted white boxes in (a). Scale bars: 2 nm.

Figure 5.2a shows the change of overall sidewall morphology for both TBs. Corresponding Fast Fourier Transforms (FFTs) confirm that the crystal structure rotates by 180° about the <111> axis at each TB (Figure 5.3). The evolution of catalyst contact angle near each TB is also consistent with double TB formation (Figure 5.4). The aberration-corrected high angle annular dark-field scanning transmission electron microscopy (HAADF-STEM) images shown in Figure 5.2c and 5.2f verify that TB$_1$ and TB$_2$ are composed of single twin planes, unlike the defect arrays frequently observed in <112> oriented Si nanowires.[24-26]

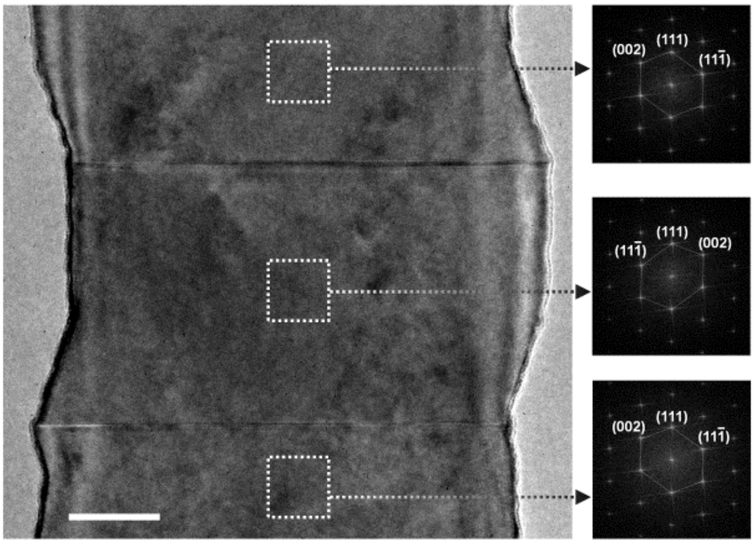

Figure 5.3: Bright-field TEM image of the Si nanowire shown in Figure 5.2 with Fast Fourier Transforms (FFTs) of the regions denoted by white dotted boxes, which confirm that the lattice rotates by 180 ° after each TB. Scale bar: 20 nm.

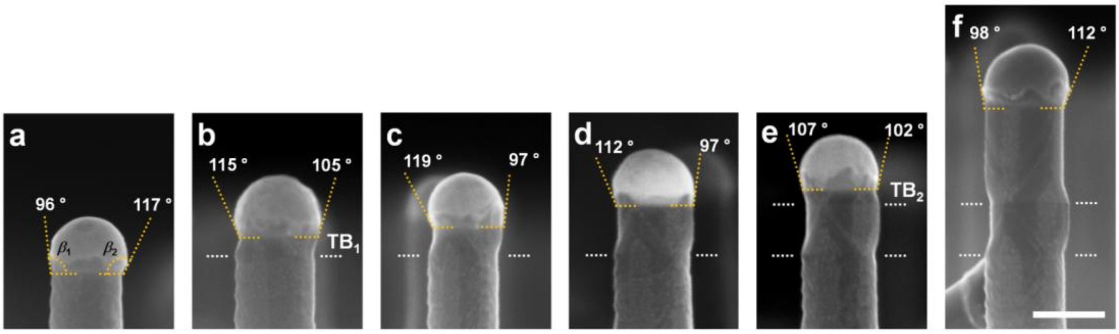

Figure 5.4: Side view SEM images of representative Si nanowires measured along the <110> direction showing the evolution of catalyst contact angle during double TB formation. The contact angles at the left and right side of the nanowire are labeled as β_1 and β_2, respectively. These images were acquired by terminating growth (a) after 10 min (i.e. before TB_1) as well as (b) 1 min, (c) 2 min, (d) 4 min, (e) 5 min, and (f) 10 min after the increase in Si_2H_6 pressure and decrease of substrate temperature (i.e. after TB_1). Scale bar: 100 nm.

Figures 5.2b, 5.2d, 5.2e, and 5.2g reveal the detailed sidewall morphology before and after each TB. Immediately prior to TB_1 and consistent with our previous report, inward moving {111} facets emerge from the broad {112} sidewall (Figure 5.2g), but the narrow, sawtooth faceted {112} facet on the opposite sidewall is not significantly impacted (Figure 5.2e). After TB_1, six {111} sidewalls emerge from the original {112} sidewalls.^{20} Conversely, and importantly, TB_2 forms without the formation of inward moving {111} facets on the broad {112} sidewall (Figure 5.2b). As the process conditions remained constant since the formation of TB_1, this result implies that the mechanism underlying TB_2 formation is distinct from that for TB_1. However, and similarly to TB_1, six {111} facets appear immediately after TB_2. We also note that the six {111} facets appearing following TB_1 and TB_2 eventually revert to {112} facets (Figure 5.2a). Although {110} facets cannot be identified when the nanowire is viewed along this zone axis, they are present on the nanowire sidewall before and after each TB (*vide infra*).

A careful analysis of SEM images taken along the <112> and <110> directions for representative nanowires containing single and double TBs, as shown in Figure 5.5, provides additional information regarding the evolution of the sidewall morphology in the vicinity of TB_1 and TB_2. Due to the complexity of the sidewall morphology, illustrations that schematically show each facet are also included with each SEM image. {112}, {111}, and {110} facets are colored in green, red, and white, respectively.

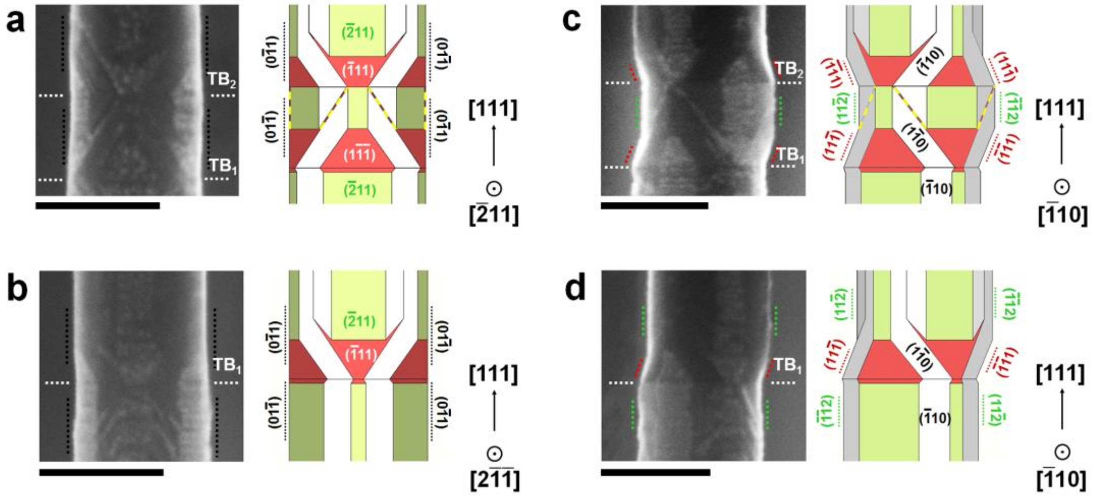

Figure 5.5: Side view SEM images and schematic illustrations of the sidewall morphology for representative single and double TBs in Si nanowires. (a) Double and (b) single TBs viewed along the <112> direction. (c) Double and (d) single TBs viewed along the <110> direction. In each SEM image, the location of TBs as well as key {112}, {111}, and {110} facets are denoted by the white, green, red, and black dotted lines, respectively. In the schematics, {112}, {111} and {110} facets are labeled as such and shaded in green, red, and white, respectively. The thin {111} facets present for double TBs are shown as yellow dashed lines. Scale bars: 100 nm.

While all nanowires exhibit six {112} sidewalls separated by {110} facets prior to TB_1, as is well documented for Si nanowires under similar growth conditions,[27,28] we subsequently observe important morphological differences for single and double TBs. When viewing nanowires containing single and double TBs along the <112> direction

(Figure 5.5a and 5.5b), the left and right sidewalls appear perpendicular to the <111> growth direction, which indicates that these are {110} facets. Upon rotating the nanowire to the <110> viewing direction (Figure 5.5c and 5.5d), it can be seen that these {110} planes, which appear dark as a result of reduced Au wetting,[28] propagate at an angle across the nanowire sidewall. SEM images measured at a range of angles relative to the substrate normal indicate that these {110} sidewalls are nearly in the same plane before and after TB_1 and TB_2 (Figure 5.6). When viewing both types of nanowire along the <110> direction (Figure 5.5c and 5.5d), and via comparison with the TEM images in Figure 5.2, large {111} facets that separate the {110} facets are identifiable after each TB.

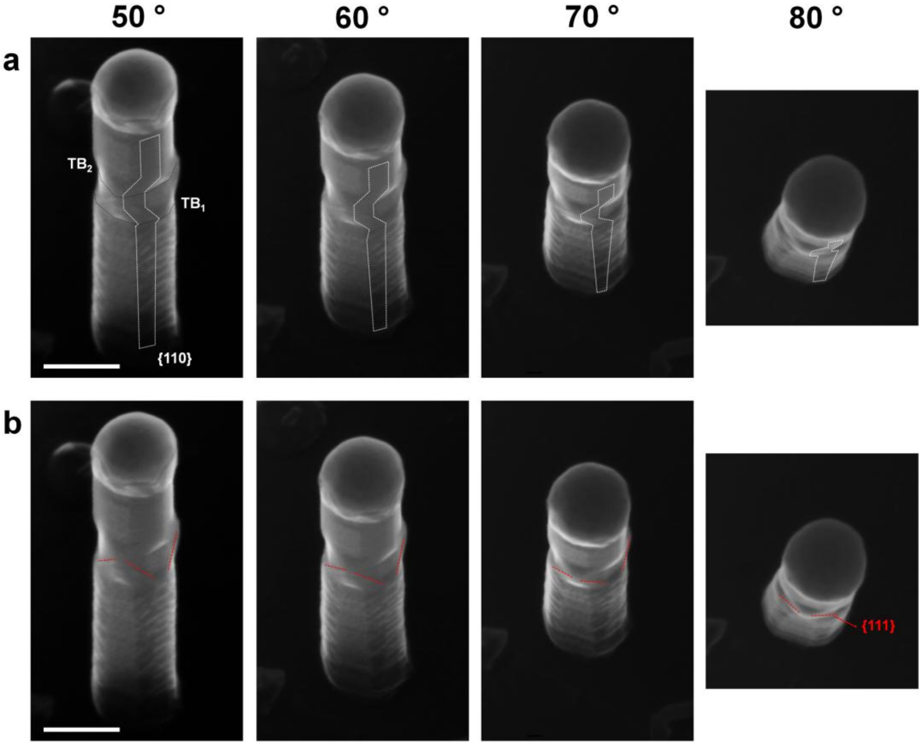

Figure 5.6: SEM images of a representative Si nanowire containing a double TB measured at a range of angles above the substrate: 50°, 60°, 70°, and 80°, where a (a) {110} sidewall is outlined in white and (b) two thin {111} facets are denoted by red dashed lines. Scale bars: 100 nm.

The sidewalls of nanowires that contain single and double TBs exhibit a number of key differences above TB_1. In the case of single TBs, the {111} facets revert to {112} orientation at some distance beyond TB_1 and the sidewall morphology matches that prior to changing process conditions, albeit rotated by 180° (Figure 5.5d). For double TBs, very thin, diagonally oriented facets, which are identified by the bright lines observed in the SEM image and represented by dashed yellow lines in the Figure 5.5a and 5.5c schematics, are visible before TB_2. These facets are assigned to {111} since they extend from the edge between {110} and {111} facets and continue even though the majority of the {111} facets reverts to {112}. Angle-dependent SEM images provide another view of these facets (Figure 5.6). Pairs of these thin {111} facets propagate toward each other across {110} facets until they intersect the {110}/{112} edge near TB_2. While the same, thin {111} facets initially appear for some nanowires containing single TBs, they terminate much earlier (Figure 5.5b and 5.5d). Double TBs can also exhibit thin {111} facets after TB_2 that disappear in the same manner as those for nanowires with a single TB.

We propose a mechanism, as illustrated in Figure 5.7, for double TB formation based on the above described changes in sidewall morphology. As we reported previously,[20] TB_1 formation appears due to the increase in Si_2H_6 pressure and decrease in substrate temperature. The triple-phase line (*i.e.* where the vapor, liquid, and solid meet) becomes increasing triangular due to the three new, inward propagating {111} facets and TB_1 eventually nucleates to reduce the line tension (Figure 5.7a). The sidewall morphology continues to evolve under the new Si_2H_6 pressure and substrate temperature after TB_1. Of the six {111} facets that appear immediately following TB_1, the width of all inward moving {111} facets – $(\bar{1}11)$, $(1\bar{1}1)$, and $(11\bar{1})$ – increases, while the width of the outward moving {111} facets – $(\bar{1}\bar{1}1)$, $(\bar{1}1\bar{1})$, and $(1\bar{1}\bar{1})$ – decreases. {110} facets, which are also present and separate the {111} planes, maintain their width as the nanowire elongates. For most of the nanowires in our study, the entire {111} facet reverts to {112} at some distance beyond TB$_1$ and no second TB (*i.e.* TB$_2$) is observed.

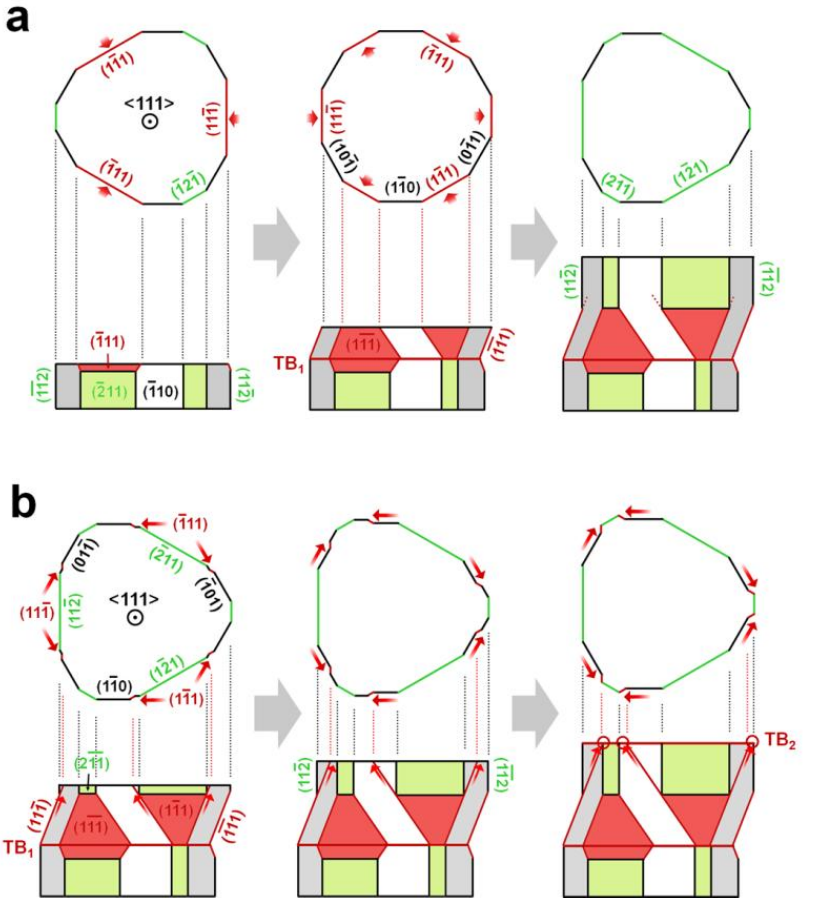

Figure 5.7: Schematic illustrations of (a) single and (b) double TB formation during Si nanowire elongation. In all illustrations, {112}, {111} and {110} facets are labeled as such and shaded in green, red, and white, respectively. Red arrows indicate the direction of facet propagation. In the case of single TBs, deformation of the triple-phase line occurs following the formation of inward moving {111} facets after the increase of Si_2H_6 pressure and decrease of substrate temperature. After TB$_1$, {111} facets continue until the {112} sidewalls remerge. In the case of double TBs, thin {111} facets, highlighted by red arrows, survive after the {112} sidewalls reappear and propagate diagonally across the {110} facet. {111} facet propagation beyond the opposite {110}/{112} edge is highly unfavorable and TB$_2$ nucleates to reduce the

triple-phase line tension. Thin {111} facets, shown as short dotted red lines in (a), occasionally appear following the reappearance of {112} sidewalls for the case of single TBs, but disappear before reaching the opposite {110}/{112} edge.

However, nanowires with two TBs exhibit thin {111} facets, which continue to propagate across the {110} facet even after the reversion to {112} (Figure 5.7b). These thin {111} facets eventually reach the {110}/{112} edge at the opposite side of the {110} facet. Beyond this point, the facets cannot extend without protruding from the nanowire sidewall and TB nucleation becomes favored over further deformation of the triple-phase line. Notably, the {112} sidewall does not undergo any obvious changes during this process (Figure 5.2b), which indicates that the thin {111} facets are largely responsible for deforming the triple-phase line and generating TB_2.

The above mechanism implies that the continued presence of thin {111} facets may enable some nanowires to contain three or more TBs. While we found a handful of nanowires with triple TBs, no nanowires with four or more TBs were observed (Figure 5.8). Nonetheless, nanowires exhibiting triple TBs contained thin {111} facets after TB_1 *and* TB_2, a finding that further supports the proposed mechanism. We expect that process conditions where six {111} facets appear after each TB, but do not revert to {112}, will lead to a more dramatic deformation of the triple-phase line, generation of more closely spaced TBs, and ultimately the appearance of twinning superlattices.[12,13]

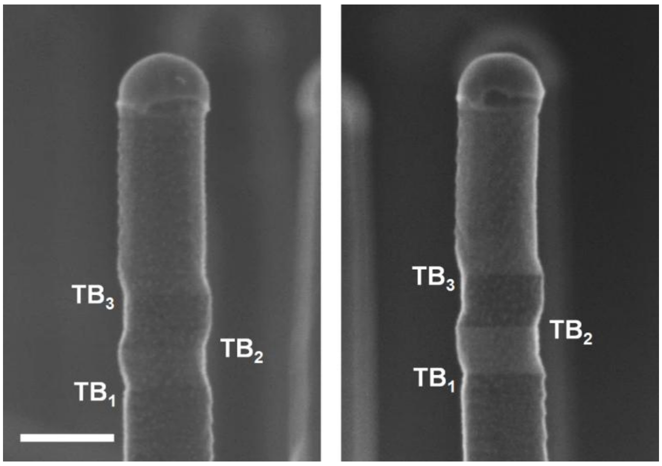

Figure 5.8: Side view SEM images of Si nanowires containing triple TBs. Scale bar: 100 nm.

Additional evidence that the thin {111} facets underlie TB$_2$ nucleation comes from a correlation of {110} facet width with the distance between TB$_1$ and TB$_2$ ($L_{TB_1-TB_2}$). More specifically, the thin {111} facets must propagate across the {110} facet before deforming the triple-phase line to the point where TB$_2$ forms and, as such, we expect the width of this facet to be linearly related to $L_{TB_1-TB_2}$.

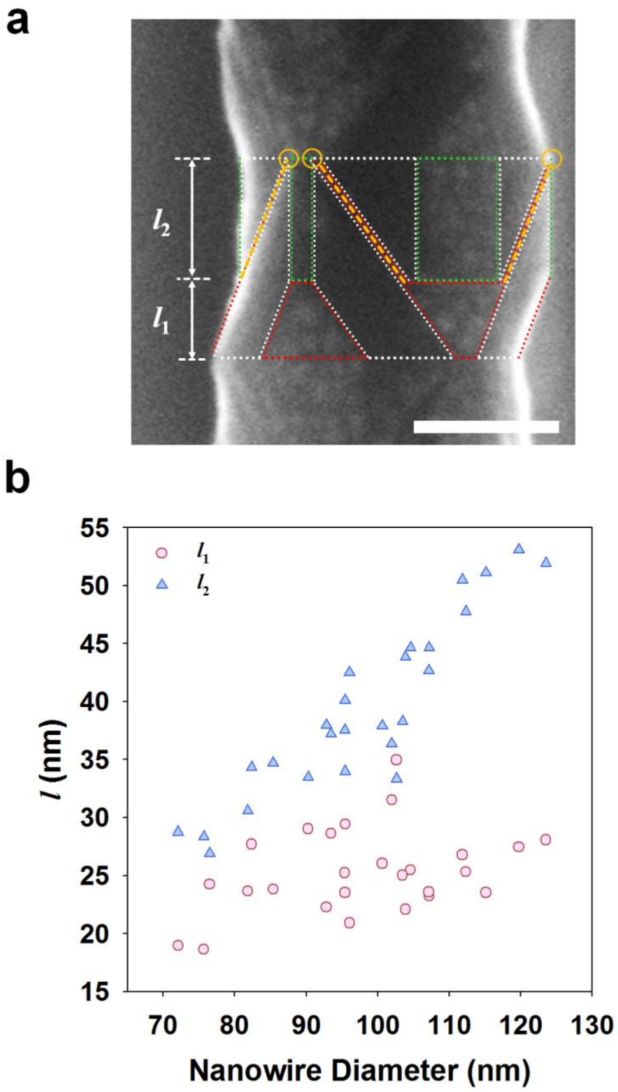

Figure 5.9: Correlation of TB spacing with sidewall morphology. (a) Side view SEM image of a representative Si nanowire containing a double TB. The {112}, {111}, and {110} facets are delineated by green, red, and white dashed lines, respectively. The thin {111} facets, which propagate across the {110} facet, are shown as dashed yellow lines and the point where they intersect the opposite {110}/{112} edge is circled in yellow. The axial distance between TB_1 and the point where the {112} sidewalls reemerge is defined as l_1, while l_2 is the axial distance between the point where the {112} sidewalls reappear and TB_2. Scale bar: 50 nm. (b) l_1 and l_2 measured from SEM images of the same 26 nanowires used in Figure 5.1b plotted as function of nanowire diameter.

Two important length scales, specifically l_1 and l_2, are identified in Figure 5.9a and sum to give $L_{TB_1-TB_2}$. l_1 is the axial length between TB_1 and the point where the majority of

{111} sidewall reverts to {112}. As illustrated in Figure 5.7, six {111} and six {110} sidewalls bound the nanowire over this length. l_2 is the axial distance from the point where the {112} sidewalls reappear to TB_2. Over this length, the nanowires containing double TBs are bounded by six {112} and six {110} surfaces, as well as the thin {111} facets. Figure 5.9b shows the relationship between l_1 and l_2, as measured from high resolution SEM images, and nanowire diameter. These data clearly show that l_1 and l_2 are linearly related to diameter, with the l_2 dependence being stronger. Since $L_{TB_1-TB_2}$ is simply the sum of l_1 and l_2, the linear dependence of $L_{TB_1-TB_2}$ with nanowire diameter (Figure 5.1b) arises primarily from changes in l_2.

A projection of the nanowire onto the $(1\bar{1}0)$ plane in the region between TB_1 and TB_2 is schematically illustrated in Figure 5.10a, where the actual ($w_{\{110\}}$) and apparent ($w_{\{110\}}$' and $w_{\{111\}}$') facet widths are labeled. While $w_{\{110\}}$ can be directly measured when viewing the nanowire along the <110> direction, $w_{\{111\}}$ must be indirectly determined. Thus, we measure $w_{\{111\}}$' and then convert this value to $w_{\{111\}}$ by knowing the angle between {110} and {111} facets is 30°:

$$w_{\{111\}} = \frac{w_{\{111\}}'}{\cos(30°)} = \frac{2}{\sqrt{3}} w_{\{111\}}' \qquad (5.1)$$

Based on high-resolution SEM images and the above relationship, the values of $w_{\{110\}}$ and $w_{\{111\}}$ were extracted (Figure 5.11). While both $w_{\{110\}}$ and $w_{\{111\}}$ are linearly correlated with diameter, the dependence of $w_{\{110\}}$ is much stronger and less variable than $w_{\{111\}}$.

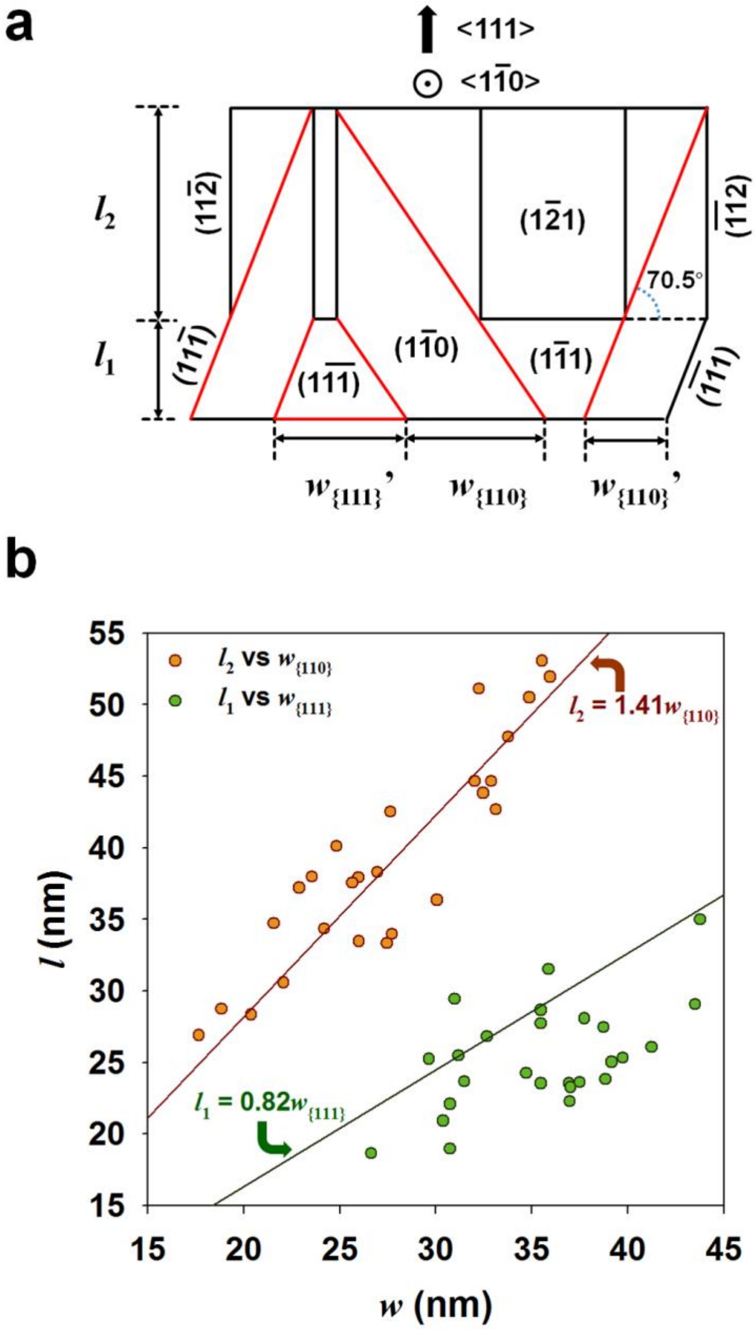

Figure 5.10: (a) Schematic illustration showing the projection of a Si nanowire containing a double TB onto the $(1\bar{1}0)$ plane. $w_{\{111\}}$ and $w_{\{111\}}$' are defined as the actual and apparent widths, respectively, of the large {111} facets. $w_{\{110\}}$ and $w_{\{110\}}$' are defined as the actual and apparent widths, respectively, of the {110} facets. (b) l_1 and l_2 plotted as a function of $w_{\{111\}}$ and $w_{\{110\}}$, respectively. Data points are experimentally derived from measurements of SEM images. Solid lines are plots of the equations relating l_1/l_2 and $w_{\{111\}}/w_{\{110\}}$, specifically $l_1 = 0.82w_{\{111\}}$ and $l_2 = 1.41w_{\{110\}}$, as derived from the nanowire structure shown in (a).

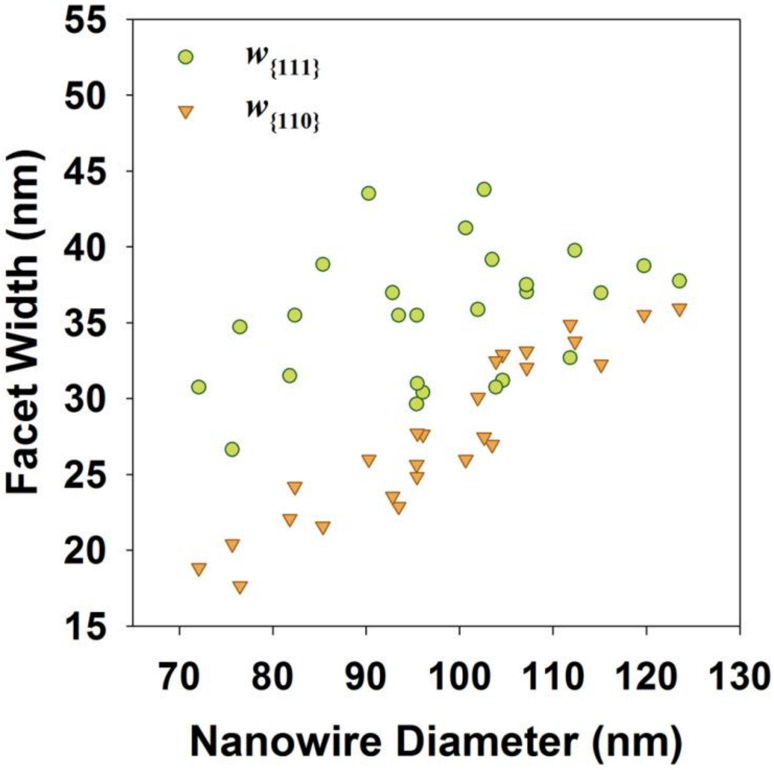

Figure 5.11: Facet width, $l_{\{111\}}$ and $l_{\{110\}}$, plotted as a function of nanowire diameter. Data points are derived from SEM images of the same 26 nanowires used in Figure 5.1b.

The values of l_1 and l_2 are now plotted as a function of $w_{\{111\}}$ and $w_{\{110\}}$, respectively, in Figure 5.10b. While the data points are extracted from experiment, it is important to note that the lines are not fits to these data and we discuss their origin below. We see that l_2 depends linearly on $w_{\{110\}}$, and because the value of l_2 is largely responsible for the change of $\mathrm{L}_{\mathrm{TB}_1-\mathrm{TB}_2}$, we then know that $w_{\{110\}}$ also correlates with $\mathrm{L}_{\mathrm{TB}_1-\mathrm{TB}_2}$. In other words, as {110} facet width increases, so too does the distance between TB_1 and TB_2. This finding is consistent with the proposed mechanism, whereby thin {111} facets propagate across the {110} plane and, in doing so, deform the triple phase line. As the {110} facet width increases (*i.e.* for larger diameter nanowires), the distance that these thin {111} facets must travel before reaching the opposite {112}/{110} edge also increases. This additional length requires that the nanowire elongate further before TB_2 nucleates.

We now compare our proposed model of nanowire sidewall evolution (*i.e.* Figure 5.7) and final morphology (*i.e.* Figure 5.5 and 5.10a) with parameters extracted from experiment (*i.e.* l_1, l_2, $w_{\{111\}}$, and $w_{\{110\}}$). This comparison serves to further validate the structure derived from our electron microscopy measurements and is particularly valuable due to the complexity seen here. If the 6 {111} facets present over the length l_1 comprise the surfaces of an ideal octahedron,[10] the relationship between $w_{\{111\}}$ and l_1 would be

$$l_1 = \frac{w_{\{111\}}}{2} \times \tan(60°) \times \sin(70.5°) = 0.82 w_{\{111\}} \tag{5.2}$$

We can determine the relationship between $w_{\{110\}}$ and l_2 similarly. If the {110} facet width is constant as the nanowire cross-section evolves over the length l_1, as indicated by our data (Figure 5.5c and 5.9a), the projection of the nanowire in the $(1\bar{1}0)$ plane (Figure 5.10a) allows us to relate l_2 and $w_{\{110\}}$' (*i.e.* the apparent width of the {110} facet) as follows:

$$l_2 = w_{\{110\}}' \times \tan(70.5°) \tag{5.3}$$

The value of $w_{\{110\}}$' can be related to $w_{\{110\}}$ (*i.e.* the actual width of the {110} facet) since all {110} sidewall are oriented 60° relative to each other:

$$w_{\{110\}}' = w_{\{110\}} \times \cos(60°) = \frac{w_{\{110\}}}{2} \tag{5.4}$$

By combining equations (5.3) and (5.4), we find that

$$l_2 = w_{\{110\}}' \times \tan(70.5°) = \frac{w_{\{110\}} \times \tan(70.5°)}{2} = 1.41 w_{\{110\}} \tag{5.5}$$

Equations (5.2) and (5.5) indicate that l_1 and l_2 are directly proportional to the width of {111} and {110} facets, respectively. Inclusion of the lines described by these equations (Figure 5.10b), which are based on the structural model alone (Figure 5.10a), shows excellent agreement with our experimental measurements. The clear correspondence strongly supports the validity of the proposed sidewall structure and double TB formation mechanism. We note that the values measured for l_1 are less than predicted by the structural model, and we suspect that this stems from our assumption that the nanowire is an ideal octahedron over the length l_1. In reality, our images indicate that the octahedron is slightly truncated (Figure 5.9a), a result that would overestimate the value of l_1.

5.5. Conclusion

We demonstrate that multiple transverse TBs are possible in <111> oriented Si nanowires and that sidewall morphology controls their spacing. While the first TB (TB_1) is driven by inward moving {111} facets that form following an abrupt increase in Si_2H_6 pressure and decrease of substrate temperature, another TB (TB_2) results from a different set of thin {111} facets that traverse the {110} sidewall. Both mechanisms, while distinct in their details, deform the triple-phase line and eventually favor TB nucleation. Detailed measurements of the sidewall show that {110} facet width governs TB_2 position and support the proposed model of nanowire morphology. It remains to be determined why the efficiency of TB_1 and TB_2 introduction is low. We recently suggested that local differences in triple-phase line shape, as a result of asynchronous sawtooth faceting, reduce the probability of TB_1 formation.[20] In terms of TB_2, the observed revision of {111} facets to {112} suggests that the energetics of these two surfaces are similar under our growth conditions. As such, we anticipate that the further stabilization of {111} facets (*i.e.* relative to {112}), possibly via surface functionalization or modification of catalyst droplet composition, will enable the fabrication of periodic defect superstructures similar to those seen in III-V nanowires.

5.6. References

1. Akopian, N.; Patriarche, G.; Liu, L.; Harmand, J. C.; Zwiller, V. *Nano Lett.* **2010,** *10*, 1198–1201.
2. Tian, B. Z.; Xie, P.; Kempa, T. J.; Bell, D. C.; Lieber, C. M. *Nat. Nanotechnol.* **2009,** *4*, 824–829.
3. Hochbaum, A. I.; Chen, R. K.; Delgado, R. D.; Liang, W. J.; Garnett, E. C.; Najarian, M.; Majumdar, A.; Yang, P. D. *Nature* **2008,** *451*, 163–167.
4. Xie, P.; Hu, Y. J.; Fang, Y.; Huang, J. L.; Lieber, C. M. *Proc. Natl. Acad. Sci. U.S.A.* **2009,** *106*, 15254–15258.
5. Zhang, G. Q.; Wang, W.; Li, X. *Adv. Mater.* **2008,** *20*, 3654–3656.
6. Perera, S.; Pemasiri, K.; Fickenscher, M. A.; Jackson, H. E.; Smith, L. M.; Yarrison-Rice, J.; Paiman, S.; Gao, Q.; Tan, H. H.; Jagadish, C. *Appl. Phys. Lett.* **2010**, *97*, 023106.
7. Ketterer, B.; Heiss, M.; Uccelli, E.; Arbiol, J.; Fontcuberta i Morral, A. *ACS Nano* **2011**, *5*, 7585–7592.
8. Assali, S.; Zardo, I.; Plissard, S.; Kriegner, D.; Verheijen, M. A.; Bauer, G.; Meijerink, A.; Belabbes, A.; Bechstedt, F.; Haverkort, J. E. M. *et al. Nano Lett.* **2013,** *13*, 1559–1563.
9. Johansson, J.; Karlsson, L. S.; Svensson, C. P. T.; Martensson, T.; Wacaser, B. A.; Deppert, K.; Samuelson, L.; Seifert, W. *Nat. Mater.* **2006,** *5*, 574–580.
10. Xiong, Q.; Wang, J.; Eklund, P. C. *Nano Lett.* **2006,** *6*, 2736–2742.
11. Verheijen, M. A.; Algra, R. E.; Borgstrom, M. T.; Immink, G.; Sourty, E.; van Enckevort, W. J. P.; Vlieg, E.; Bakkers, E. P. A. M. *Nano Lett.* **2007,** *7*, 3051–3055.
12. Algra, R. E.; Verheijen, M. A.; Borgstrom, M. T.; Feiner, L.-F.; Immink, G.; van Enckevort, W. J. P.; Vlieg, E.; Bakkers, E. P. A. M. *Nature* **2008,** *456*, 369–372.
13. Caroff, P.; Dick, K. A.; Johansson, J.; Messing, M. E.; Deppert, K.; Samuelson, L. *Nat. Nanotechnol.* **2009,** *4*, 50–55.
14. Carim, A. H.; Lew, K. K.; Redwing, J. M. *Adv. Mater.* **2001,** *13*, 1489–1491.
15. Dayeh, S. A.; Wang, J.; Li, N.; Huang, J. Y.; Gin, A. V.; Picraux, S. T. *Nano Lett.* **2011,** *11*, 4200–4206.
16. Shin, N.; Filler, M. A. *Nano Lett.* **2012,** *12*, 2865–2870.
17. Arbiol, J.; Fontcuberta i Morral, A.; Estrade, S.; Peiro, F.; Kalache, B.; Roca i Cabarrocas, P.; Ramon Morante, J. *J. Appl. Phys.* **2008,** *104*, 064312.

18. Conesa-Boj, S.; Zardo, I.; Estrade, S.; Wei, L.; Alet, P. J.; Roca i Cabarrocas, P.; Morante, J. R.; Peiro, F.; Fontcuberta i Morral, A.; Arbiol, J. Defect Formation in Ga-Catalyzed Silicon Nanowires. *Cryst. Growth Des.* **2010,** *10*, 1534–1543.
19. Chou, Y.-C.; Wen, C.-Y.; Reuter, M. C.; Su, D.; Stach, E. A.; Ross, F. M. *ACS Nano* **2012,** *6*, 6407–6415.
20. Shin, N.; Chi, M.; Howe, J. Y.; Filler, M. A. *Nano Lett.* **2013,** 13, 1928–1933.
21. Algra, R. E.; Verheijen, M. A.; Feiner, L.-F.; Immink, G. G. W.; Theissmann, R.; van Enckevort, W. J. P.; Vlieg, E.; Bakkers, E. P. A. M. *Nano Lett.* **2010,** *10*, 2349–2356.
22. Kodambaka, S.; Tersoff, J.; Reuter, M. C.; Ross, F. M. *Phys. Rev. Lett.* **2006,** *96*, 096105.
23. Ross, F. M.; Tersoff, J.; Reuter, M. C. *Phys. Rev. Lett.* **2005,** *95*, 146104.
24. Davidson, F. M.; Lee, D. C., III; Fanfair, D. D.; Korgel, B. A. *J. Phys. Chem. C* **2007,** *111*, 2929–2935.
25. Lopez, F. J.; Givan, U.; Connell, J. G.; Lauhon, L. J. *ACS Nano* **2011,** *5*, 8958–8966.
26. Barth, S.; Boland, J. J.; Holmes, J. D. *Nano Lett.* **2011,** *11*, 1550–1555.
27. Oehler, F.; Gentile, P.; Baron, T.; Ferret, P.; Den Hertog, M.; Rouviere, J. *Nano Lett.* **2010,** *10*, 2335–2341.
28. Boukhicha, R.; Gardes, C.; Vincent, L.; Renard, C.; Yam, V.; Fossard, F.; Patriarche, G.; Jabeen, F.; Bouchier, D. *Europhys. Lett.* **2011,** *95*, 18004.

CHAPTER 6

THE INTERPLAY BETWEEN SURFACE HYDROGEN AND DEFECT PROPAGATION IN SI NANOWIRE KINKING SUPERSTRUCTURES

6.1. Overview

Despite recent demonstrations of kinking superstructures in semiconductor nanowires, it remains difficult to achieve the fidelity needed for robustly manipulating electronic, optical, thermal, and mechanical behavior. Here, we combine real-time *in situ* infrared spectroscopy with high-resolution electron microscopy to show the critical role of surface hydrogen and twin boundary (TB) propagation during the <111>/<112> kinking of Si nanowires. We also identify the mechanism by which high fidelity superstructures are possible. In particular, the presence of a continuous TB at <112> → <112> kinks, and the pinning of the nucleation site that likely accompanies it, reduces the number of degenerate directions available to the nanowire. Our findings provide important insight into the vapor-liquid-solid technique and identify new possibilities for systematically controlling nanowire kinking.

6.2. Introduction

Semiconductor nanowires containing kinking superstructures – multiple, user-programmable changes to growth orientation – offer tantalizing opportunities to create new electronic devices,[1-3] manipulate thermal conductivity,[4] and explore mechanical behavior.[5] While the synthesis of such structures is possible via shape-guided lateral growth[6] or metal-assisted chemical etching,[7] the vapor-liquid-solid (VLS) technique holds particular promise.[8, 9] For example, VLS allows for the integration of additional functionality via selective doping[10] and/or heterostructure formation. The point where a nanowire changes its growth orientation – the "kink" – is the most basic building block of any kinking superstructure. For example, a <111> to <112> kink is frequently observed for Si nanowires[11-15] and induced by low temperature,[11] high pressure,[14, 15] and/or the addition of hydrogen on the sidewall.[13] Kinking superstructures, composed of different, yet degenerate, <112> segments, are also attainable by briefly decreasing pressure.[1, 8] Despite this recent demonstration, however, similar, high fidelity superstructures have yet to be reported for other growth orientations or nanowire systems (e.g., Ge, III-V).[9, 16] Most often, it is not possible to select a specific crystal orientation (e.g., [110]) out of many possible degenerate options (e.g., [101], [011], etc.).[9]

Planar defects, in the form of twin boundaries (TB)[17-19] and/or polytypes,[20, 21] are often seen in conjunction with kinks. Several mechanisms have been proposed to explain defect introduction when Si nanowires kink to the <112> direction, including changes to supersaturation,[18, 22, 23] sidewall hydrogen coverage,[13] or catalyst volume.[24] It is also unclear why these defects remain during <112> oriented growth and how they behave at subsequent growth direction changes. Although previously demonstrated Si nanowire kinking superstructures consist of <112> segments,[1, 8] the presence of planar defects, and their potential influence on the synthesis, is unknown.

A detailed understanding of the interplay between surface termination, defect propagation, and kinking would constitute an important step toward the *ab initio* synthesis of distinct types of high fidelity kinking superstructures. Here, we extend our previous work,[13] which showed that covalently bonded hydrogen on the surface of Si nanowires is essential for <112> oriented growth. When surface hydrogen is removed, despite the favorability of nucleation at the TB,[18] we find that the nanowire returns to <111> oriented growth and the defect terminates at the sidewall. We also confirm that <112> → <112> kinking, the process underlying previously demonstrated kinking superstructures,[8] is assisted by the presence of a TB that is continuous in all segments. Our data indicate that the TB, and the pinning of the nucleation site that accompanies it, enhances defect superstructure fidelity by forcing the nanowire to select from two, as opposed to the many possible, <112> directions.

6.3. Experimental methods

6.3.1. Nanowire growth

Si nanowires are grown on a Si (111) substrate in a custom-built ultrahigh vacuum (UHV) chamber described previously.[13] Samples are cut to 5 mm × 24 mm and pre-cleaned by immersing into 1M HF solution for 5 min to remove the native oxide. After deionized water rinsing for 30 seconds and drying with N_2, the sample is immediately loaded into the chamber and heated to 600 °C for 1 hr in vacuum. The sample is then cleaned by flash-annealing to 1200 °C for 30 s. A 2 nm thick Au film is deposited after slowly cooling to near room temperature. To initiate nanowire growth, disilane (Voltaix, 99.998%) is initially introduced at pressure of 2×10^{-4} Torr with the substrate at 590 °C for 2 min. To elongate the initial <111> segment, the substrate temperature is subsequently lowered to 490 °C, at constant Si_2H_6 pressure. The pressure and temperatures for each subsequent segment are described in the main text.

6.3.2. *In situ* IR spectroscopy

Surface hydrogen covalently bonded to the nanowire sidewall is measured via *in situ* infrared spectroscopy. The FTIR spectrometer (Bruker V70) is equipped with a KBr beamsplitter and HgCdTe detector.[13] In this work, all spectra are collected with a 58° angle of incidence. The sample and background spectra consist of 1680 scans with a resolution of 4 cm^{-1}. A new background scan is recorded when the substrate temperature changes during the I → II transition (*vide infra*). All spectra are baseline corrected with a standard concave rubberband procedure.

6.3.3. SEM and TEM analysis

Si nanowire kink morphology and crystal structure are analyzed via a Zeiss Ultra 60 field emission scanning electron microscope (SEM) and a FEI Titan S80-300 transmission electron microscope (TEM). Nanowires are removed from the growth substrate via ultrasonication and then drop cast onto lacey carbon grids (Ted Pella) in isopropanol.

6.4. Results and discussion

We first show the relationship between Si nanowire growth direction and the presence of adsorbed hydrogen atoms on the sidewalls. Two different growth procedures were used to investigate <112> → <111> (Figure 6.1a-d) and <112> → <112> (Figure 6.1f-i) kinking. Nanowires containing both types of kink are first initiated with a <111> segment, oriented perpendicular to the Si(111) substrate, which simplifies the identification and comparison of different growth directions. The growth conditions for this initial <111> segment, denoted as I for simplicity, are 2 × 10^{-4} Torr Si_2H_6 and 490 °C.

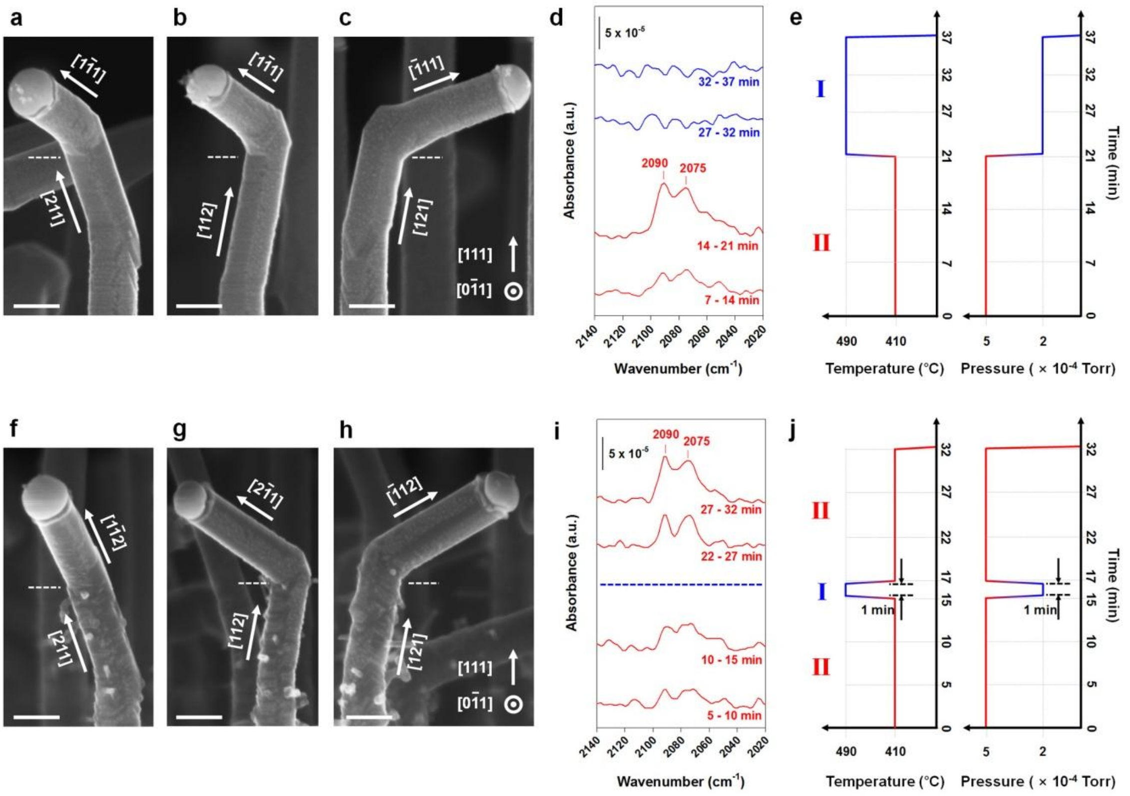

Figure 6.1: Pressure- and temperature-dependent kinking. Side view SEM images along the $[0\bar{1}1]$ orientation of representative Si nanowires showing <112> → <111> kinking: (a) [211] → $[1\bar{1}1]$, (b) [112] → $[1\bar{1}1]$, and (c) [121] → $[\bar{1}11]$. Scale bars: 100 nm. (d) Corresponding real-time *in-situ* infrared spectra of the ν(Si-H) stretching region measured during <112> and <111> segment growth. (e) Schematic profile of substrate temperature and Si_2H_6 pressure as a function of time for <112> → <111> kinking. Condition I: 2 × 10^{-4} Torr Si_2H_6 and 490 °C; Condition II: 5 × 10^{-4} Torr Si_2H_6 and 410 °C. Side view SEM images along the $[0\bar{1}1]$ orientation of representative Si nanowires showing <112> → <112> kinking: (f) [211] → $[1\bar{1}2]$, (g) [112] → $[2\bar{1}1]$, and (h) [121] → $[\bar{1}12]$. Scale bars: 100 nm. (i) Corresponding real-time *in situ* infrared spectra of the ν(Si-H) stretching region measured during growth of two <112> segments. The blue dotted line, located between the 10 – 15 and 22 – 27 min spectra, marks the 1 min step at condition I prior to returning to condition II. (j) Schematic profile of substrate temperature and Si_2H_6 pressure as a function of time change for <112> → <112> kinking.

To examine <112> → <111> kinking, Si nanowires were subsequently elongated at 5 × 10^{-4} Torr Si_2H_6 and 410 °C, denoted condition II, for 21 min and then returned to 2 × 10^{-4}

Torr Si_2H_6 and 490 °C (i.e., I) for another 15 min (Figure 6.1e). Figure 6.1a-c show representative side view scanning electron microscopy (SEM) images, measured along the $[0\bar{1}1]$ direction, of the <112> → <111> transition that results from this sequence of steps. While the earlier I → II condition change does not immediately force a kink (Figure 6.2), it is important to note that <111> oriented growth begins almost instantly at the II → I transition. We confirm each of these growth orientation assignments with transmission electron microscopy (TEM), as discussed below.

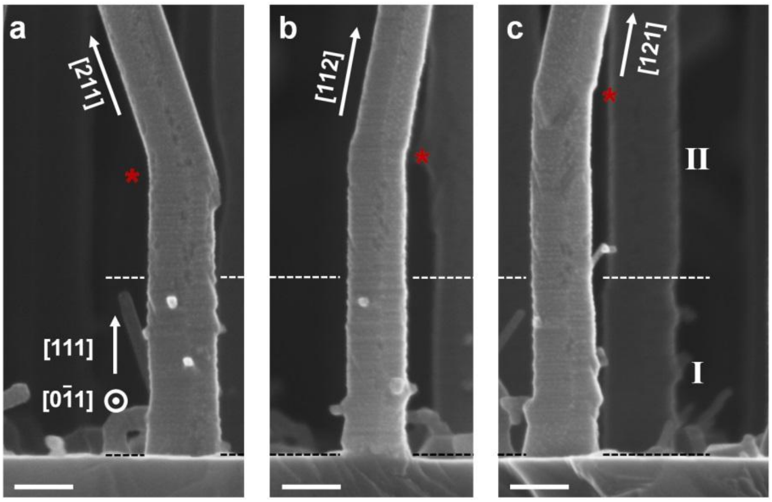

Figure 6.2: Side view SEM images of Si nanowires viewed along the $[0\bar{1}1]$ direction showing that the initial <111> → <112> kink, denoted by a red star, occurs at different axial positions: (**a**) [111] → [211], (**b**) [111] → [112], and (**c**) [111] → [121]. Scale bars: 100 nm.

Figure 6.1d shows real-time *in-situ* infrared absorption spectra measured at multiple points, beginning at the I → II condition transition, for <112> and <111> segment growth. Spectra recorded from 7 - 14 and 14 - 21 min show an increase of two characteristic ν(Si−H) stretching modes at 2075 and 2090 cm^{-1}, which we assign to hydrogen atoms adsorbed on {111} and {113} facets, respectively.[13] These spectral features are consistent with the {111} and {113} facets previously reported, and also discussed below, for <112> oriented nanowires.[13, 25] However, spectra measured following the subsequent II → I condition transition, specifically for 27 - 32 and 32 - 37 min, reveal that ν(Si−H) modes, and thus adsorbed hydrogen atoms, are no longer present. These data, in conjunction with our previous results for <111> → <112> kinking,[13] confirm the strong relationship between nanowire growth direction and adsorbed hydrogen atoms. Raising the concentration of adsorbed hydrogen increases the probability of a <111> → <112> kink, while lowering the concentration of adsorbed hydrogen results in an immediate <112> → <111> transition.

We find a distinct situation for <112> → <112> kinking. Following the initial <111> segment growth, we synthesize the first <112> segment at condition II for 15 min and then form the second <112> segment by returning to condition I, but only for 1 min, and then resuming <112> elongation at condition II for the final 15 min (Figure 6.1j). Side view SEM images of Si nanowires with representative <112> → <112> kinks are displayed in Figure 6.1f-h. Unlike <112> → <111> kinking, we observe small diameter nanowires on the sidewalls of the first <112> segment and attribute their presence to Au diffusion on the sidewall.[13, 26] Figure 6.1i shows the corresponding *in-situ* infrared spectra recorded during growth of both <112> segments. During growth at condition II, and similar to that observed at the 7 - 14 and 14 - 21 min time points in Figure 6.1d, the ν(Si−H) stretching mode intensity increases. These features are again attributed to hydrogen atoms adsorbed on {111} and {113} facets. However, growth of the second <112> segment results in a further increase of these modes, indicating that adsorbed hydrogen remains. We are not able to directly probe the hydrogen coverage during the 1 min application of condition I, but expect that some, if not all, of the hydrogen is temporarily removed via H_2 desorption.[27]

The <111> → <112> → <111> and <111> → <112> → <112> nanowire superstructures, owing to the degeneracy of the {112} and {111} crystallographic orientations, are both chiral.

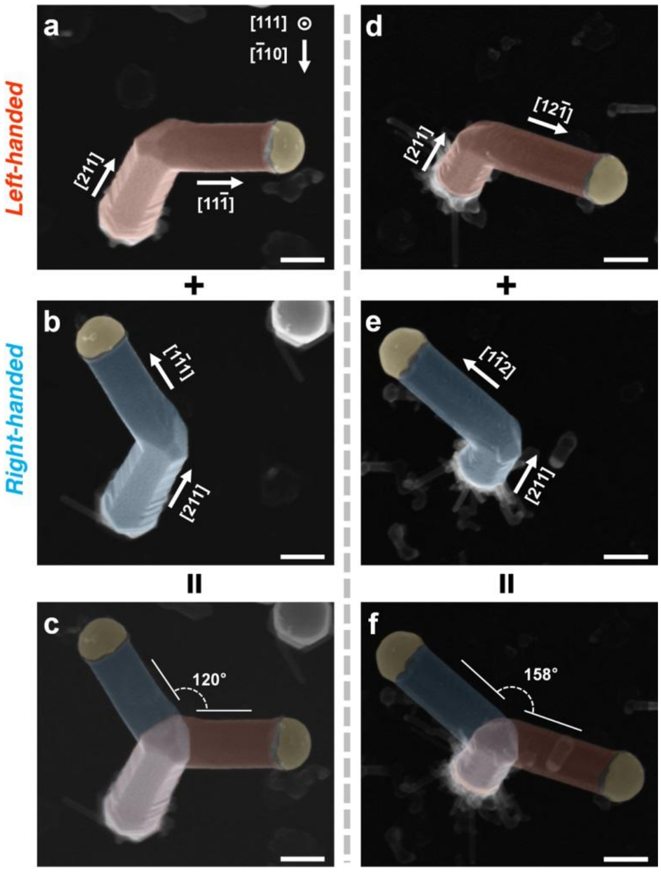

Figure 6.3: Left- and right-handed kinking superstructures. Top view SEM images of representative (a) [111] → [211] → [11$\bar{1}$] (false-colored red) and (b) [111] → [211] → [1$\bar{1}$1] (false-colored blue) kinking superstructures. (c) Superimposition of the superstructures shown in (a) and (b). Top view SEM images of representative (d) [111] → [211] → [12$\bar{1}$] (false-colored red) and (e) [111] → [211] → [1$\bar{1}$2] (false-colored blue) kinking superstructures. (f) Superimposition of the superstructures shown in (d) and (e). Scale bars: 100 nm.

Figure 6.3a and 6.3b show top-down SEM images of two representative <111> → <112> → <111> nanowires. When viewed in this manner, the first [111] segment is hidden. Here, the nanowires can kink from [211] to one of two degenerate <111> directions, $[11\bar{1}]$ or $[1\bar{1}1]$, and the resulting nanowire is either left-handed (false-colored in red) or right-handed (false-colored blue). By overlaying the SEM images of left- and right-handed nanowires, as shown in Figure 6.3c, we observe an angle of 120° as expected for two <111> segments when viewed in this direction (Figure 6.4). Analogous SEM images of left- and right-handed <111> → <112> → <112> nanowires are displayed in Figure 6.3d and 6.3e. As shown in Figure 6.3f, and expected for <112> segments, these nanowires exhibit an angle of 158° relative to each other (Figure 6.4). Due to the degeneracy of the <111> and <112> directions, Figure 6.3 is only showing a subset of the six structures possible for each type of kinking. We note that, without additional structural information, such a large number of available structures would that suggest high fidelity superstructure formation is unlikely. We return to this point below.

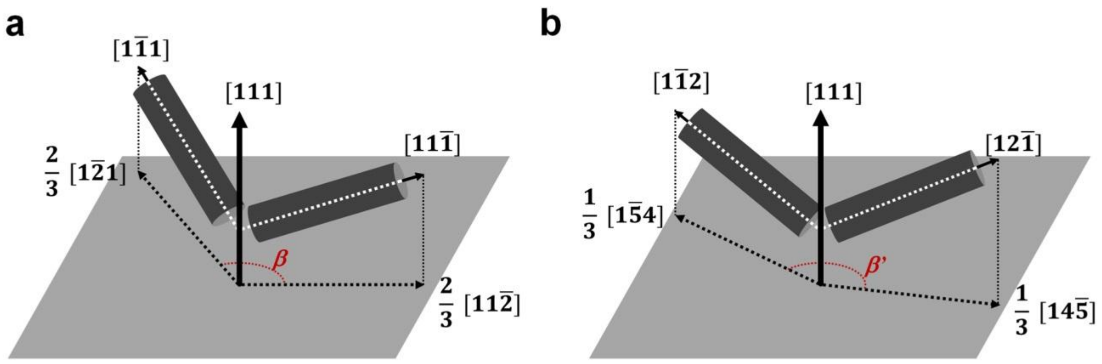

Figure 6.4: Schematic illustrates of the terminal nanowire segments projected onto the (111) plane. (a) For a <112> → <111> kink, the projection of the terminal segments ($[11\bar{1}]$ and $[1\bar{1}1]$) onto the (111) plane are $\frac{2}{3}[11\bar{2}]$ and $\frac{2}{3}[1\bar{2}1]$, and β, the angle between these vectors is 120°. (b) For a <112> → <112> kink, the

projection the terminal segments ($[12\bar{1}]$ and $[1\bar{1}2]$) onto the (111) plane are $\frac{1}{3}[14\bar{5}]$ and $\frac{1}{3}[1\bar{5}4]$. β', the angle between these vectors is 158.2°.

We now use TEM to examine the crystal structure and presence of defects for our kinking superstructures. The first <112> segment, which is grown with condition II, always contains an odd number of TBs (Figure 6.5).[18, 21]

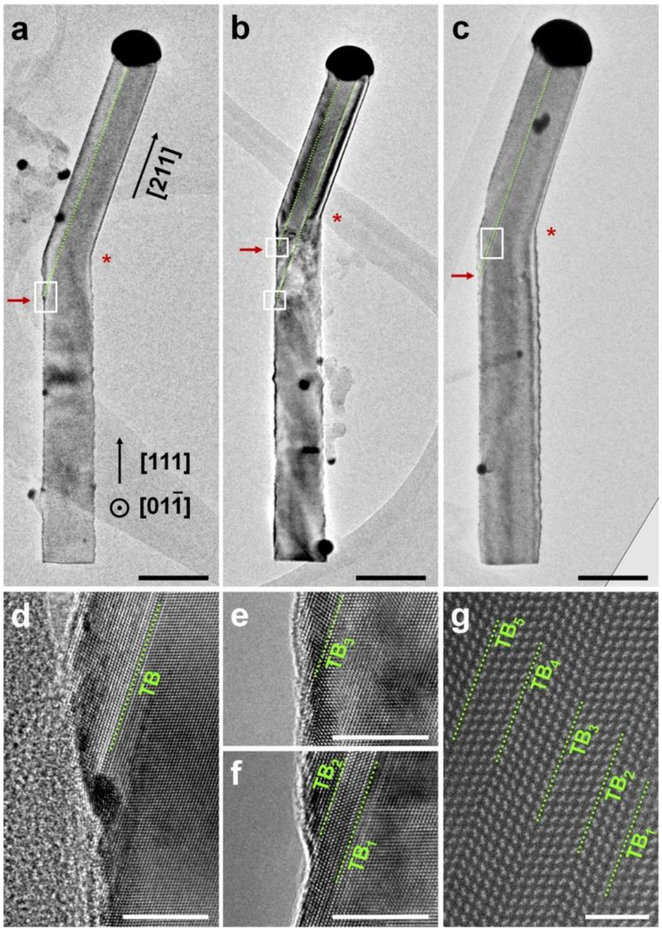

Figure 6.5: Structural analysis of the initial <111> to <112> kink. (a-c) Bright field TEM images of Si nanowires viewed along the $[01\bar{1}]$ zone axis. As described in the main text, the initial <111> segment is grown at 2 × 10^{-4} Torr Si_2H_6 and 490 °C (condition I) for 10 min and then 5 × 10^{-4} Torr Si_2H_6 and 410 °C (condition II) for the next 10 min. All Si nanowires exhibiting a kink contain an odd number of TBs, as indicated by the green dotted lines, parallel to the [211] direction: (a) 1, (b) 3, and (c) 5 TBs. Red arrows and stars indicate the nucleation point of the last formed TB and kink position, respectively. Scale bars: 100 nm. (d) High resolution TEM image of the region indicated by the white box in (a) showing a single TB. Scale bar: 10 nm. (e, f) High resolution TEM images of the regions indicated in (b) showing the existence

of 3 TBs. Scale bars: 10 nm. (g) High angle annular dark-field (HAADF) scanning TEM image of the region indicated in (c) confirming 5 TBs. Scale bar: 2 nm.

The TBs initiate from the broad {112} sidewall at the initial <111> → <112> kink. We propose that adsorbed hydrogen atoms, present for growth with condition II (Figure 6.1d or 6.1h), lowers the solid-vapor interface energy, modifies the force balance at the triple-phase line, and increases the probability of TB nucleation. For the present discussion, we will simply focus on the presence of the TB in <112> oriented segments and note that additional studies are required to unravel the details of its initial nucleation. However, we find that the time between the application of condition II and kinking varies between nanowires (Figure 6.2) and, in some cases, the nanowires remain <111> oriented. These results suggest that a kinetic barrier separates <111> and <112> oriented growth and that the TB helps overcome it.

Nanowire morphology near both <112> → <111> (Figure 6.1a-d) and <112> → <112> (Figure 6.1f-i) kinks is particularly informative. Figure 6.6 shows TEM and SEM images as well as summary illustrations for the <112> → <111> transition that show the direction change, facet evolution, and the fate of the TB. Importantly, distinct superstructures form when the nanowire selects different, yet degenerate, crystallographic directions (i.e., $[1\bar{1}1]$, $[11\bar{1}]$, and $[\bar{1}11]$ for the last <111> segment). However, when projected into the plane, these structures appear identical (Figure 6.7) and cannot be distinguished via TEM. Therefore, we label the sequence of segments shown in Figure 6.6 as [211] → $[1\bar{1}1]$ for all the nanowires. When viewing the nanowire along the $[0\bar{1}1]$ zone axis (Figure 6.6a), we observe a $(\bar{1}11)$ TB that propagates along the [211] growth direction and terminates at the sidewall near the kink. The FFT inset confirms its assignment as a TB. The [211] segment is bounded by a $(1\bar{1}\bar{1})_t$ facet, where the subscript t indicates that the facet belongs to the twinned lattice (Figure 6.6b).

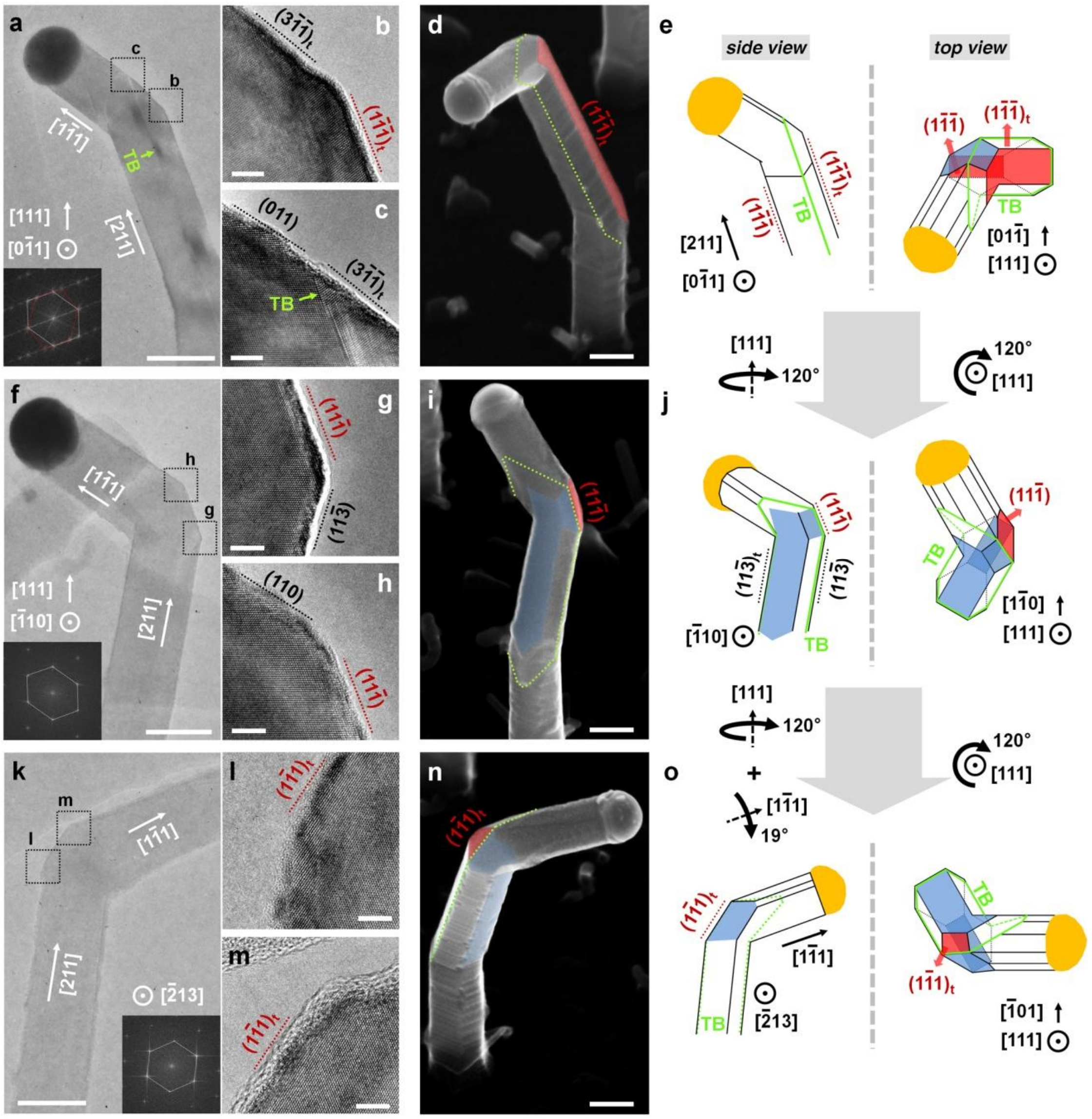

Figure 6.6: Sidewall facet morphology near a <112> → <111> kink. Nanowires in all images are labeled [111] → [211] → $[1\bar{1}1]$ for simplicity and as described in the text. (a, f, k) Low magnification bright field TEM images taken along $[0\bar{1}1]$, $[\bar{1}10]$, and $[\bar{2}13]$ zone axis, respectively. Each FFT inset is of the region near the kink. Scale bars: 100 nm. (b, c) High resolution TEM images of the regions boxed in (a). Scale bars: 5 nm. (g, h) High resolution TEM images of the regions boxed in (f). Scale bars: 5 nm. (l, m) High resolution TEM images of the regions boxed in (k). Scale bars: 5 nm. (d,i,n) 45° view SEM images highlighting the {111} facets (false-colored in red) shown in (a,f,k). {111} facets not observed via TEM are also noted (false-colored in blue). All facets belonging to the twinned domain are denoted with the

subscript t. TBs are indicated by green dotted lines and/or arrows. Scale bars: 100 nm. (e,j,o) Summary illustrations from the side and top of the [211] → $[1\bar{1}1]$ kink.

The $(1\overline{11})_t$ facet subsequently transitions to $(3\overline{11})_t$ near the kink (Figure 6.6b) and then to (011) at the point where the TB intersects the sidewall (Figure 6.6c). Viewing the nanowire along the $[\bar{1}10]$ zone axis (Figure 6.6f) allows us to see that a $(11\bar{3})$ facet also bounds the [211] segment (Figure 6.6g). This facet converts to $(11\bar{1})$ and then to (110) at the kink (Figure 6.6g,h). The FFT inset verifies that all of these facets belong to the original lattice. We also note that the $(\bar{1}11)$ TB is not observable from this zone axis. Finally, viewing the nanowire along the $[\bar{2}13]$ zone axis, in which both the [211] and $[1\bar{1}1]$ segment lie on the plane perpendicular to the zone axis, shows that the kink is bounded by another $(1\bar{1}1)_t$ facet (Figure 6.6k-m).

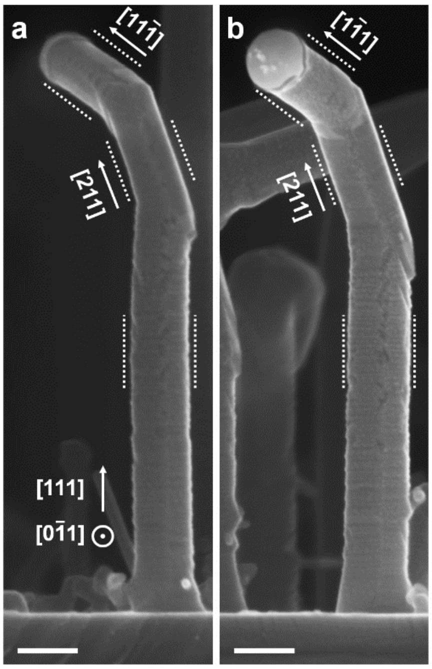

Figure 6.7: Side view SEM images of two distinct kinking superstructures, specifically (a) [111] → [211] → $[11\bar{1}]$ and (b) [111] → [211] → $[1\bar{1}1]$, exhibiting a nearly identical projection onto the $[0\bar{1}1]$ plane. Scale bars, 100 nm.

We note that the FFT inset of Figure 6.6k shows a diffraction pattern that does not correspond to a single crystalline diamond cubic lattice. Additional TEM images of the [211] → $[1\bar{1}1]$ kink are shown in Figure 6.8 and help explain this observation. The lattice fringes (Figure 6.8b,c) and FFT patterns (Figure 6.8d,e) observed at the points indicated in Figure 6.8a are clearly distinct. The FFT pattern in Figure 6.8d corresponds to diamond cubic Si viewed along the $[\bar{2}13]$ zone axis.[28] As illustrated in Figure 6.8f, [451] is not the orientation of the nanowire sidewall. This can be understood by considering the irregular hexagonal cross section of <111> oriented Si nanowires,[29, 30] where the broad {121} sidewall is angled 19° relative to [451]. On the other hand, the FFT image in Figure 6.8e exhibits a pattern consistent with two lattices exhibiting a twinned relationship.[28, 31] Diffraction spots associated with the original lattice, and similar to those seen in Figure 6.8d, are labeled in white. An additional set of diffraction spots, labeled in yellow, are also present and result from the twinned region. Based on this double diffraction pattern, we assign the surface facet shown in Figure 6.8c to $(1\bar{1}1)_t$ (Figure 6.8g). Since the TB orientation is neither vertical nor parallel to the zone axis, it is not visible in these images. The observation of distinct diffraction patterns for different regions of the nanowire provides additional evidence that the [211] → $[1\bar{1}1]$ kink results in TB termination.

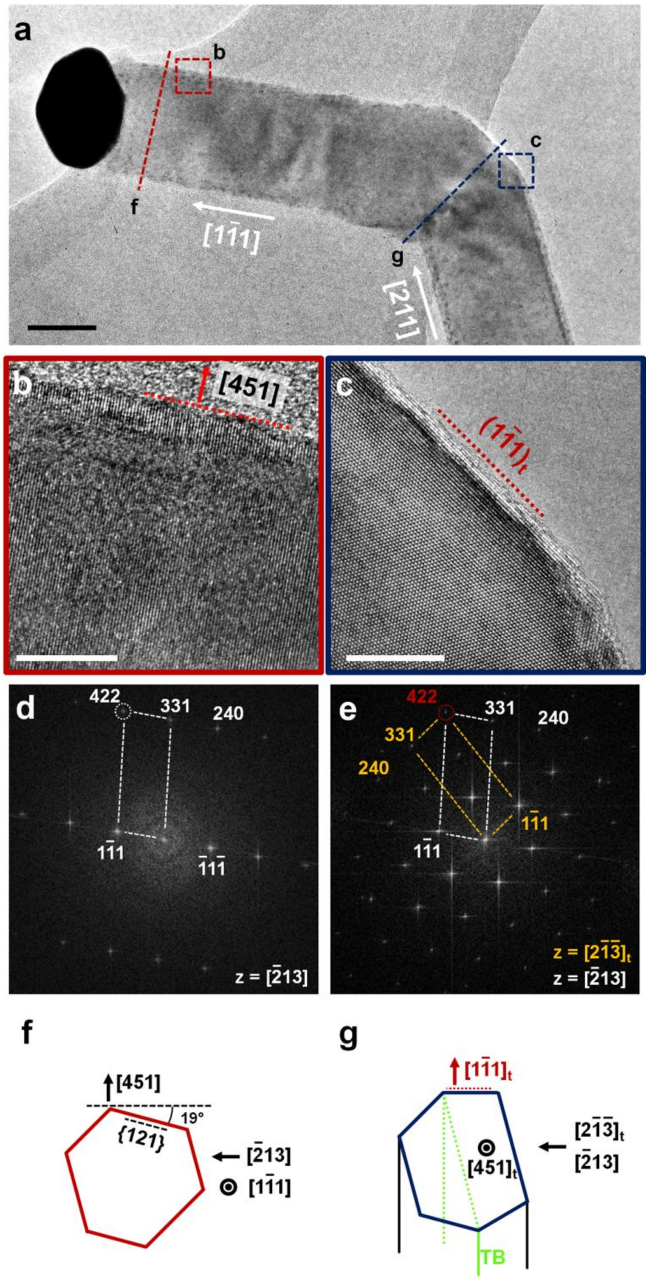

Figure 6.8: Analysis of odd diffraction pattern at [211] → [1$\bar{1}$1] kink. (a) Low magnification bright field TEM image along [$\bar{2}$13] zone axis of representative [211] → [1$\bar{1}$1] kink. Scale bar: 50 nm. High resolution TEM images of the nanowire measured, as denoted by the dotted boxes in (a), near the (b) catalyst droplet tip and (c) [211] → [1$\bar{1}$1] kink. Scale bars: 10 nm. (d, e) FFT diffraction patterns corresponding to the TEM images in (b, c). The diffraction patterns in (d) and (e) confirm that these regions are single-crystalline and twinned, respectively. (f, g) Schematic illustration of nanowire cross-section at each point indicated in (a).

Figure 6.9 compares the morphology of [211] → $[1\bar{1}1]$ and [211] → $[1\bar{1}2]$ kinks viewed along the $[01\bar{1}]$ direction. The observed kink direction (Figure 6.9a,b) and TB propagation (Figure 6.9c,d) for these situations exhibit critical differences. As shown above, when a [211] nanowire kinks to $[1\bar{1}1]$, the $(\bar{1}11)$ TB terminates at the sidewall of the $[1\bar{1}1]$ segment (Figure 6.9c). Strikingly, the TB continues when a [211] nanowire kinks to $[1\bar{1}2]$ (Figure 6.9d, Figure 6.10). The inset high resolution TEM image clearly shows that the TB extends to the liquid-solid interface. We also note that the liquid-solid interface morphology in the $[1\bar{1}2]$ segment is inverted relative to the prior [211] segment (Figure 6.11).

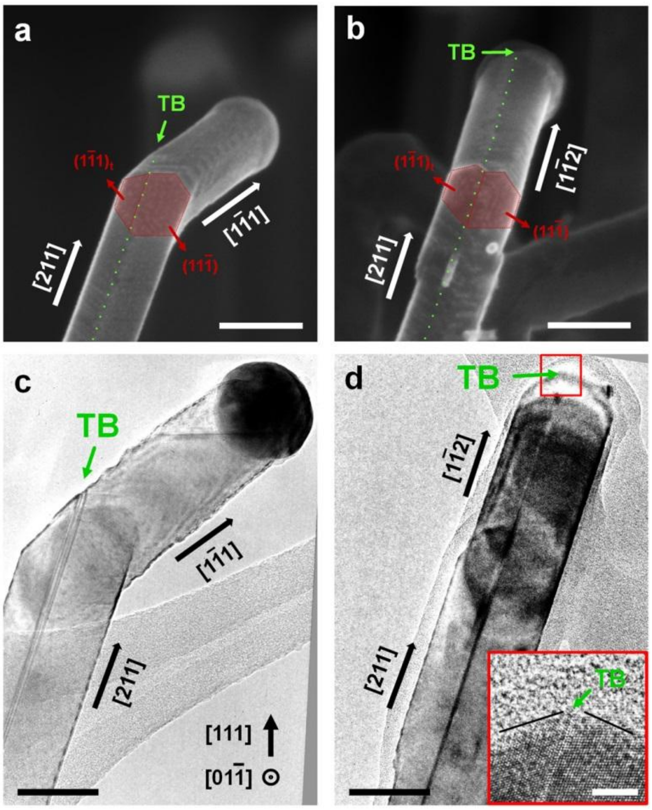

Figure 6.9: Comparison of TB propagation at [211] → $[1\bar{1}1]$ and [211] → $[1\bar{1}2]$ kinks. Side view SEM images along the $[01\bar{1}]$ direction of representative (a) [211] → $[1\bar{1}1]$ and (b) [211] → $[1\bar{1}2]$ kinks. The approximate location of each TB is denoted by green dotted lines and arrows. Important sidewall facets are

false-colored in red. Scale bars: 100 nm. (c) Low magnification bright field TEM image along the [$01\bar{1}$] zone axis of the [211] → [$1\bar{1}1$] kink showing that the TB terminates at the sidewall of the [$1\bar{1}1$] segment. Scale bar: 50 nm. (d) Low magnification bright field TEM image along the [$01\bar{1}$] zone axis of the [211] → [$1\bar{1}2$] kink. The TB does not terminate in this situation, but propagates inside the new [$1\bar{1}2$] segment. Scale bar: 50 nm. Inset: High resolution TEM image showing the TB and faceting of the liquid-solid interface. Scale bar: 5 nm.

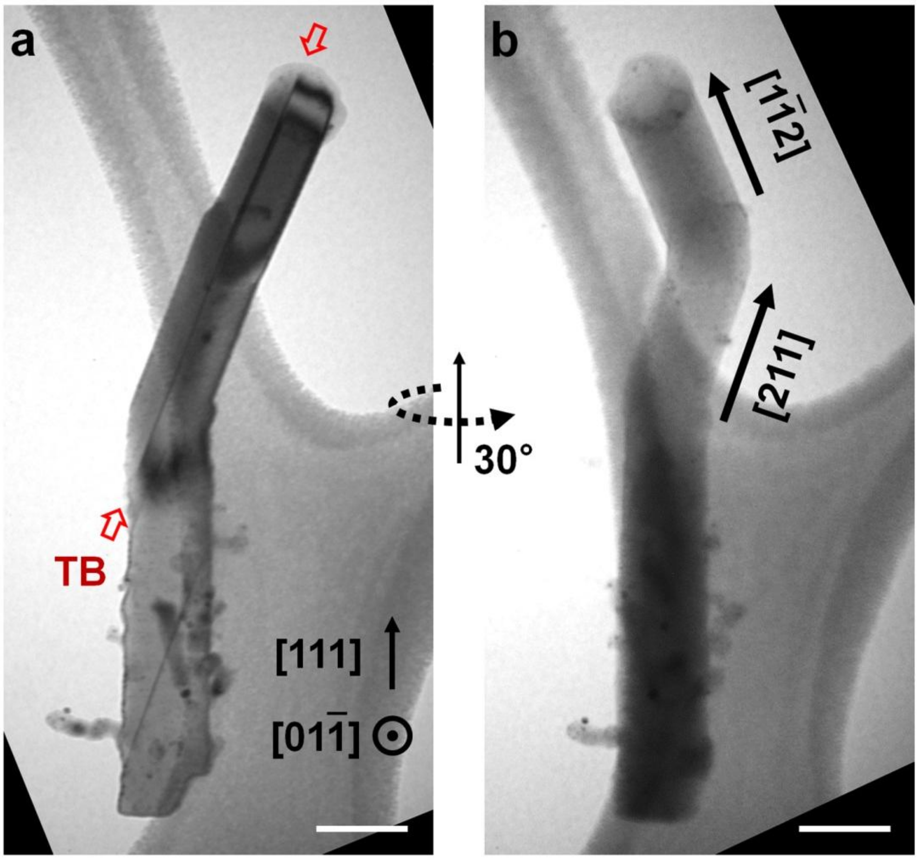

Figure 6.10: (a) Low magnification bright field TEM images along the [$0\bar{1}1$] zone axis of a Si nanowire kinking superstructure showing that the TB continues at a <112> → <112> kink. (b) Rotation of the same nanowire by 30° around the [111] direction confirms that two <112> segments, specifically [211] and [$1\bar{1}2$], are present. The Au catalyst tip likely detached during ultrasonication in preparation for TEM imaging. Scale bars: 100 nm.

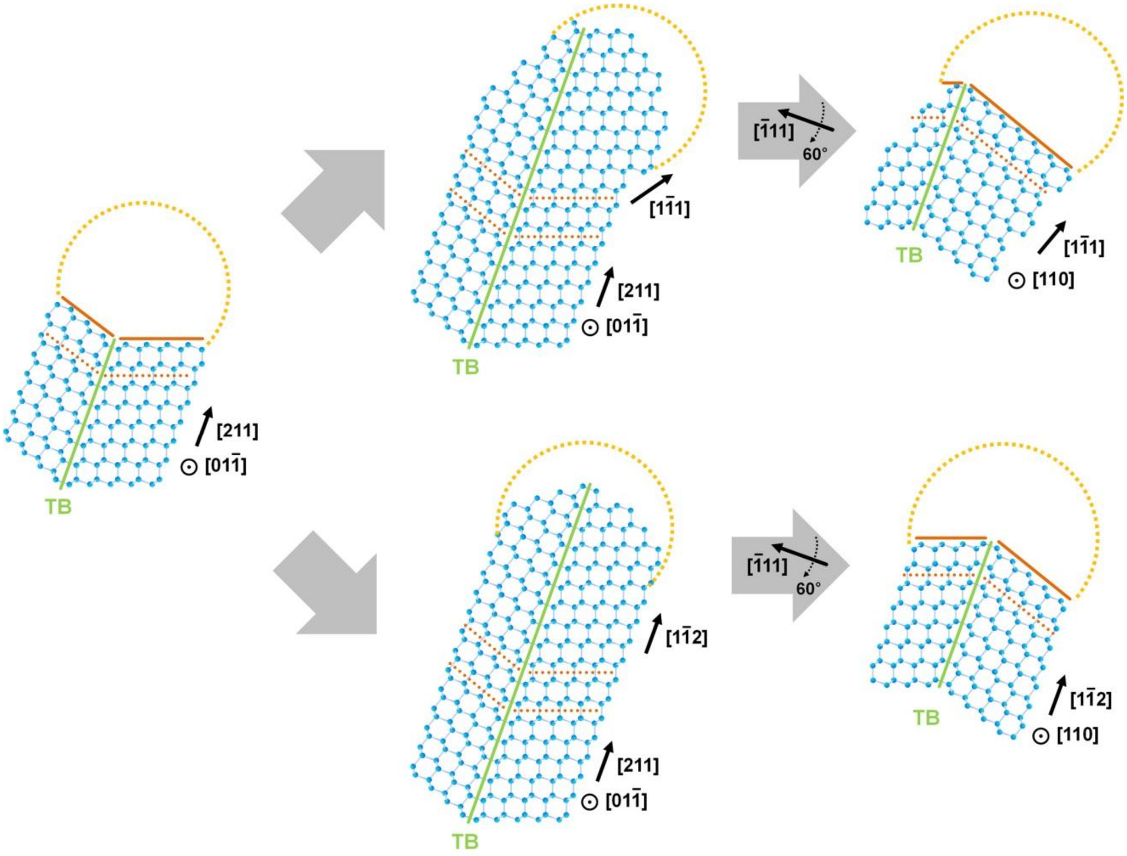

Figure 6.11: Schematic illustration of growth front morphology, particularly liquid-solid interface faceting, as a function of kink type and growth time. The liquid-solid interface of the first [211] segment exhibits two {111} facets oriented 141° with respect to each other. At a [211] → $[1\bar{1}1]$ transition, the liquid-solid interface front facet becomes flat, similar to traditional <111> growth, and the TB terminates. However, our data and proposed model indicate that a [211] → $[1\bar{1}2]$ transition results in a liquid-solid interface that is inverted with respect to the first [211] segment. Two {111} facets, oriented 219° relative to each other, are now present.

We propose a mechanism for [211] → $[1\bar{1}1]$ and [211] → $[1\bar{1}2]$ kinking, schematically illustrated in Figure 6.12, which is based on our observations of growth direction, adsorbed hydrogen, TB propagation, and sidewall faceting. The morphology, and thus mechanism of formation, for both kinks is initially similar. When the nanowire grows in the [211] direction, it is bounded by 4 {113} sidewalls, specifically $(11\bar{3})$, $(1\bar{3}1)$, $(11\bar{3})_t$, and $(1\bar{3}1)_t$, and 2 {111} sidewalls, specifically $(1\overline{11})$ and $(1\overline{11})_t$ (Figure 6.12a).

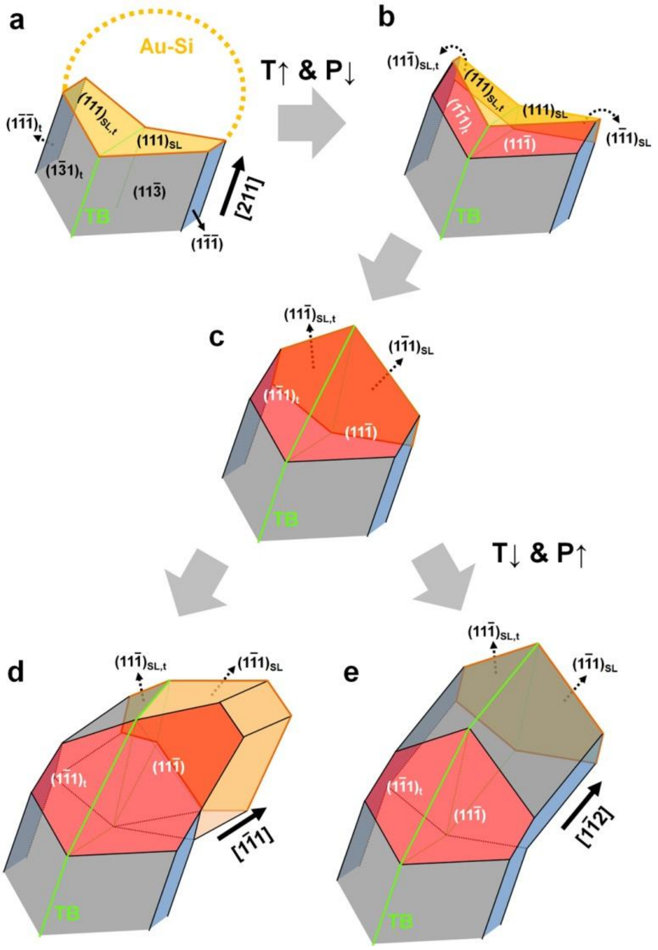

Figure 6.12: Proposed kinking mechanism. (a) The liquid-solid interface of [211] nanowires growing under condition II consist of $(111)_{SL}$ and $(111)_{SL,t}$ facets with an angle of 141° between them. (b) After transitioning to condition I, 4 {111} facets emerge from the {113} sidewalls, distort the triple-phase line, and cause the catalyst droplet to wet the $(11\bar{1})_{SL,t}$ and $(1\bar{1}1)_{SL}$ facets while the $(111)_{SL}$ and $(111)_{SL,t}$ facets shrink. (c) At a later time, the liquid-solid interface completes its transition to $(11\bar{1})_{SL,t}$ and $(1\bar{1}1)_{SL}$. (d) For nanowires that then grow in the $[1\bar{1}1]$ direction (continuation of condition I), the liquid-solid interface becomes $(1\bar{1}1)_{SL}$ and the TB terminates at the sidewall. (e) Nanowires that continue growth in the $[1\bar{1}2]$ direction (condition II reapplied after 1 min at condition I) exhibit $(11\bar{1})_{SL,t}$ and $(1\bar{1}1)_{SL}$ facets at the liquid-solid interface. These liquid-solid facets, which are angled 219° with respect to each other, are inverted relative to the case for the [211] segment shown in (c). Importantly, the TB is continuous between the [211] and $[1\bar{1}2]$ segments.

Reports of similar sidewall morphologies are consistent these results.[25] The liquid-solid interface consists of $(111)_{SL}$ and $(111)_{SL,t}$ planes and the TB intersects the edge between them. Since the TB is higher in energy than the $(111)_{SL}$ and $(111)_{SL,t}$ surfaces, nucleation is likely pinned here.[18, 19, 21, 32] Thus, for [211] growth, nucleation can occur at or near one of the two points where the TB intersects the triple-phase line. When reverting to growth conditions that favor <111> growth (i.e., I), $(11\bar{1})$ and $(1\bar{1}1)_t$ facets emerge from the $(11\bar{3})$ and $(1\bar{3}1)_t$ facets, respectively. On the opposite side of the nanowire, the $(1\bar{3}1)$ and $(11\bar{3})_t$ facets transition to $(1\bar{1}1)$ and $(11\bar{1})_t$ facets, respectively. A reduction of the liquid-solid interface area occurs as this process continues and eventually causes the catalyst droplet to wet the recently formed {111} facets. At this point, the liquid-solid interface consists of the original $(111)_{SL}$ and $(111)_{SL,t}$ planes as well as $(1\bar{1}1)_{SL}$ and $(11\bar{1})_{SL,t}$ planes (Figure 6.12b). The new $(11\bar{1})$ and $(1\bar{1}1)_t$ facets continue to elongate until only the $(1\bar{1}1)_{SL}$ and $(11\bar{1})_{SL,t}$ planes comprise the liquid-solid interface (Figure 6.12c). Such behavior is supported by *in situ* TEM measurements of nanowires kinking away from the <111> direction.[24] Importantly, our infrared data, which show that adsorbed hydrogen atom removal is coincident with $[211] \rightarrow [1\bar{1}1]$ kink formation, strongly indicates that hydrogen influences facet formation and catalyst wetting behavior.[13]

The mechanisms for $[211] \rightarrow [1\bar{1}1]$ and $[211] \rightarrow [1\bar{1}2]$ kinking diverge beyond this point due to the continuation of growth with condition I or by switching to condition II, respectively (*vide supra*). For a $[211] \rightarrow [1\bar{1}1]$ kink, the $(11\bar{1})_{SL,t}$ facet continues to shrink and the $(1\bar{1}1)_{SL}$ facet ultimately dominates the liquid-solid interface (Figure 6.12d). The TB is now propagating at a 19.5° angle relative to the new $[1\bar{1}1]$ growth direction, eventually meeting with and terminating at the nanowire sidewall. The situation is distinct for $[211] \rightarrow [1\bar{1}2]$ kinking. Since condition II', which favors <112> growth, is applied after 1 min, the TB is not able to reach the nanowire sidewall and it continues to propagate along the new $[1\bar{1}2]$ growth direction (Figure 6.12e). Here, the liquid-solid interface, analogous to the [211] segment, is comprised of $(1\bar{1}1)_{SL}$ and $(11\bar{1})_{SL,t}$ facets.

We now address the importance of this mechanism within the context of kinking superstructures specifically and nanowire growth in general. Foremost, our data indicates that the presence of a continuous TB at [211] → $[1\bar{1}2]$ kinks underlies high fidelity superstructure formation.[8] The TB, by virtue of the nucleation pinning associated with it, reduces to 2 (i.e. $[12\bar{1}]$ or $[1\bar{1}2]$) the number of available growth directions from as many as 23 possibilities. Therefore, <112> → <112> kinking superstructures always occupy the same plane as the continuous TB and exhibit a fixed kink angle of 120°, as previously reported.[8] However, in the event that the TB terminates, which occurs in [211] → $[1\bar{1}1]$ structures or in [211] → $[1\bar{1}2]$ structures with a sufficiently long step at condition I, fidelity is lost. Upon TB elimination, nucleation likely returns to the truncated facets on {112} sidewall (e.g. (121), $(\bar{2}\bar{1}1)$, and $(1\bar{1}\bar{2})$ sidewall facets of $[1\bar{1}1]$ segment).[33, 34] When another <112> segment is added, by again applying condition II, the next TB can initiate from any of these sidewalls, and thus propagate in 3 different orientations (Table 6.1 and 6.2). Thus, the superstructure will exhibit a reduced persistence length. This mechanism also predicts that the liquid-solid interface of the $[1\bar{1}2]$ segment will consist of $(1\bar{1}1)_{SL}$ and $(11\bar{1})_{SL,t}$ facets that intersect with an angle of 219° (Figure 6.11). This angle implies the [211] and $[1\bar{1}2]$ segments, despite their degeneracy, exhibit liquid-solid interfaces that are inverted with respect to each other. We are able to identify this inversion (Figure 6.13), which supports the proposed model.

Table 6.1: Possible orientations of the 3rd and 4th segments for a <111> → <112> → <111> → <112> Si nanowire kinking superstructure.

2nd segment - <112>	3rd segment - <111>	4th segment - <112>[a]
[211]	$[1\bar{1}1]$	$[2\bar{1}1]$
		$[1\bar{2}1]$
		$[1\bar{1}2]$
	$[11\bar{1}]$	$[21\bar{1}]$
		$[12\bar{1}]$
		$[11\bar{2}]$

[a] This configuration assumes the TB present in the 2nd segment (i.e., <112>) terminates in the 3rd segment (i.e., <111>).

Table 6.2: Possible orientations of the 3rd and 4th segments for a <111> → <112> → <112> → <112> Si nanowire kinking superstructure.

2nd segment - <112>	3rd segment - <112>	4th segment - <112>
[211]	$[1\bar{1}2]$	[211]
		$[12\bar{1}]$
	$[12\bar{1}]$	[211]
		$[1\bar{1}2]$

[a] This configuration assumes the TB present in the 2nd segment (i.e., <112>) does not terminate.

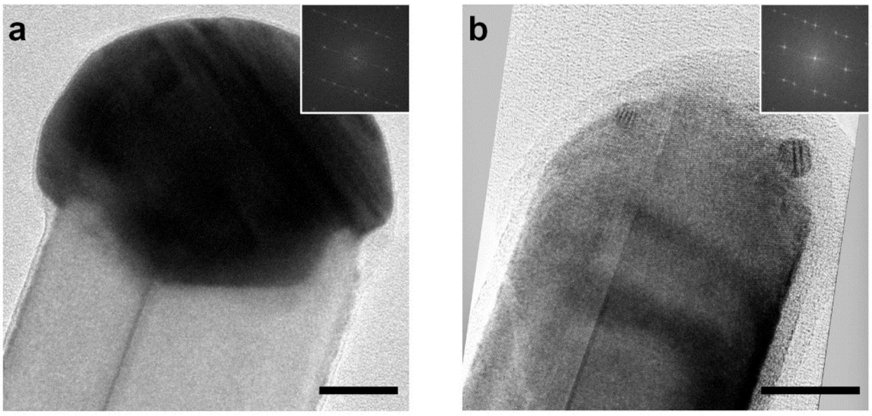

Figure 6.13: Bright field TEM images of the growth front for a Si nanowire after the (a) first and (b) second <112> segment. Note the inverted relationship of the liquid-solid interface. Inset: FFT diffraction patterns confirm the presence of a TB. Scale bars: 20 nm.

The above discussed morphological changes, when considered in conjunction with changes to surface hydrogen coverage, also provide insight into the processes that most impact nanowire growth. Foremost, the possibility of two different liquid-solid interface geometries and thus contact angles under the same growth conditions, as predicted by continuum modeling,[35] indicates that the liquid-solid and liquid-vapor interface energetics are unlikely to drive the kinking transition. The observed TB termination for [211] → $[1\bar{1}1]$ kinking, despite the favorability of nucleation at the TB, also indicates that the TB does not strongly influence growth energetics. Rather, it is likely that surface hydrogen strongly impacts the solid-vapor interface energy, modifies the force balance, and favors <112> oriented nanowires. While the TB may initially help overcome the kinetic barrier separating stable <111> and <112> growth modes, it does not appear essential for <112> growth. In fact, there are multiple of examples kinked nanowires without internal defects.[9, 36, 37]

6.5. Conclusion

We show that Si nanowire kinking superstructures comprised of <112> segments exhibit a continuous TB that lies in the same plane as the superstructure. We propose a mechanism by which nucleation pinning at this TB reduces the symmetry of the growth front, restricts the number of available growth directions, and results in high fidelity superstructures for this system. The presence of adsorbed hydrogen atoms only during <112> growth, in conjunction with the observation of multiple liquid-solid interface morphologies and TB elimination for <112> → <112> and <112> → <111> kinking, respectively, supports the importance of solid-vapor chemical bonding. Our data suggest that future attempts to engineer alternative, and simultaneously high fidelity, kinking superstructures should combine (1) novel chemistries, to favor different growth directions by modifying the force balance at the triple-phase line, and (2) a structural feature, for example a planar defect, to limit the number of nucleation points.

6.6. References

1. Tian, B. Z.; Cohen-Karni, T.; Qing, Q.; Duan, X. J.; Xie, P.; Lieber, C. M. *Science* **2010,** *329*, 830-834.
2. Jiang, Z.; Qing, Q.; Xie, P.; Gao, R. X.; Lieber, C. M. *Nano Lett.* **2012,** 12, 1711-1716.
3. Xu, L.; Jiang, Z.; Qing, Q.; Mai, L. Q.; Zhang, Q. J.; Lieber, C. M. *Nano Lett.* **2013,** *13*, 746-751.
4. Jiang, J. W.; Yang, N.; Wang, B. S.; Rabczuk, T. *Nano Lett.* **2013,** *13*, 1670-1674.
5. Jiang, J. W.; Rabczuk, T. *Appl. Phys. Lett.* **2013,** *102*, 123104.
6. Pevzner, A.; Engel, Y.; Elnathan, R.; Tsukernik, A.; Barkay, Z.; Patolsky, F. *Nano Lett.* **2012,** *12*, 7-12.
7. Chen, H. A.; Wang, H.; Zhang, X. H.; Lee, C. S.; Lee, S. T. *Nano Lett.* **2010,** *10*, 864-868.
8. Tian, B. Z.; Xie, P.; Kempa, T. J.; Bell, D. C.; Lieber, C. M. *Nat. Nanotechnol.* **2009,** *4*, 824-829.
9. Musin, I. R.; Filler, M. A. *Nano Lett.* **2012,** *12*, 3363-3368.
10. Cohen-Karni, T.; Casanova, D.; Cahoon, J. F.; Qing, Q.; Bell, D. C.; Lieber, C. M. *Nano Lett.* **2012,** *12*, 2639-2644.
11. Madras, P.; Dailey, E.; Drucker, J. *Nano Lett.* **2009,** *9*, 3826-3830.
12. Madras, P.; Dailey, E.; Drucker, J. *Nano Lett.* **2010,** *10*, 1759-1763.
13. Shin, N.; Filler, M. A. *Nano Lett.* **2012,** *12*, 2865-2870.
14. Lugstein, A.; Steinmair, M.; Hyun, Y. J.; Hauer, G.; Pongratz, P.; Bertagnolli, E. *Nano Lett.* **2008,** *8*, 2310-2314.
15. Dailey, E.; Madras, P.; Drucker, J. *Appl. Phys. Lett.* **2010,** *97*, 143106.
16. Wang, J.; Plissard, S. R.; Verheijen, M. A.; Feiner, L. F.; Cavalli, A.; Bakkers, E. *Nano Lett.* **2013,** *13*, 3802-3806.
17. Davidson, F. M.; Lee, D. C.; Fanfair, D. D.; Korgel, B. A. *J. Phys. Chem. C* **2007,** *111*, 2929-2935.
18. Dayeh, S. A.; Wang, J.; Li, N.; Huang, J. Y.; Gin, A. V.; Picraux, S. T. *Nano Lett.* **2011,** *11*, 4200-4206.
19. Dayeh, S. A.; Liu, X. H.; Dai, X.; Huang, J. Y.; Picraux, S. T.; Soci, C. *Appl. Phys. Lett.* **2012,** *101*, 053121.

20. Lopez, F. J.; Givan, U.; Connell, J. G.; Lauhon, L. J. *ACS Nano* **2011,** *5*, 8958-8966.
21. Jeon, N.; Dayeh, S. A.; Lauhon, L. J. *Nano Lett.* **2013,** *13*, 3947-3952.
22. Hocevar, M.; Immink, G.; Verheijen, M.; Akopian, N.; Zwiller, V.; Kouwenhoven, L.; Bakkers, E. *Nat. Commun.* **2012,** *3:1266* doi: 10.1038/ncomms2277.
23. Schwarz, K. W.; Tersoff, J. *Nano Lett.* **2011,** *11*, 316-320.
24. Hillerich, K.; Dick, K. A.; Wen, C. Y.; Reuter, M. C.; Kodambaka, S.; Ross, F. M. *Nano Lett.* **2013,** *13*, 903-908.
25. Hyun, Y.-J.; Lugstein, A.; Steinmair, M.; Bertagnolli, E.; Pongratz, P. *Nanotechnology* **2009,** *20*, 125606.
26. Dailey, E.; Madras, P.; Drucker, J. *J. Appl. Phys.* **2010,** *108*, 064320.
27. Gupta, P.; Colvin, V. L.; George, S. M. *Phys. Rev. B* **1988,** *37*, 8234-8243.
28. Cayron, C.; Den Hertog, M.; Latu-Romain, L.; Mouchet, C.; Secouard, C.; Rouviere, J. L.; Rouviere, E.; Simonato, J. P. *J. Appl. Cryst.* **2009,** 42, 242-252.
29. Ross, F. M.; Tersoff, J.; Reuter, M. C. *Phys. Rev. Lett.* **2005,** *95*, 146104.
30. Oehler, F.; Gentile, P.; Baron, T.; Ferret, P.; Den Hertog, M.; Rouviere, J. *Nano Lett.* **2010,** *10*, 2335-2341.
31. den Hertog, M. I.; Cayron, C.; Gentile, P.; Dhalluin, F.; Oehler, F.; Baron, T.; Rouviere, J. L. *Nanotechnology* **2012,** *23*, 025701.
32. Tang, W.; Picraux, S. T.; Huang, J. Y.; Gusak, A. M.; Tu, K. N.; Dayeh, S. A. *Nano Lett.* **2013,** *13*, 2748-2753.
33. Wen, C. Y.; Tersoff, J.; Hillerich, K.; Reuter, M. C.; Park, J. H.; Kodambaka, S.; Stach, E. A.; Ross, F. M. *Phys. Rev. Lett.* **2011,** *107*, 025503.
34. Gamalski, A. D.; Ducati, C.; Hofmann, S. *J. Phys. Chem. C* **2011,** *115*, 4413-4417.
35. Schwarz, K. W.; Tersoff, J. *Nano Lett.* **2012,** *12*, 1329-1332.
36. Meister, S.; Peng, H. L.; McIlwrath, K.; Jarausch, K.; Zhang, X. F.; Cui, Y. *Nano Lett.* **2006,** *6*, 1514-1517.
37. Jung, C. S.; Kim, H. S.; Im, H. S.; Seo, Y. S.; Park, K.; Back, S. H.; Cho, Y. J.; Kim, C. H.; Park, J.; Ahn, J. P. *Nano Lett.* **2013,** *13*, 543-549.

CHAPTER 7

CONCLUDING REMARKS

7.1. Conclusions

Throughout this thesis, we have presented the role of surface chemistry on controlling semiconductor nanowire structures, which have been previously underestimated in the nanowire growth kinetics. We have hypothesized that the change of solid-vapor interface energy via formation of chemical bonding is sufficient to change the nanowire morphology, and chosen Au catalyzed VLS grown Si nanowires as model system, to investigate surface hydrogen produced from Si_2H_6 precursor decomposition existing on the nanowire sidewalls. Since the traditional nanowire analysis has been relied on the microscopic measurement techniques such as TEM, which are not appropriate for the detection of short-lived surface hydrogen, we have developed a custom system composed of an ultrahigh vacuum chamber and *in situ* IR spectroscopy.

As the first result of this research, we have proven the existence of surface hydrogen on the sidewalls of Si nanowires in real-time during for the first time,[1] as described in Chapter 3. This result provides the insight of the sidewall facet change during the nanowire growth, and important correlation between the amount of surface hydrogen and nanowire growth orientation. Specifically, we observed the <111> oriented nanowires when there is low concentration of surface hydrogen, whereas <112> nanowires with larger amount of hydrogen. Since this correlation is based on the condition-dependent intrinsic change of hydrogen, we presented the direct proof of the role of surface hydrogen on the nanowire growth direction change, by introducing external hydrogen radicals under the intrinsic hydrogen-deficient growth condition. These results reveal the critical role of hydrogen near the triple-phase line and create new opportunities to control the structure and physical properties of semiconductor nanowires via surface chemistry. We also expect these findings are of general importance and can be utilized to advance the rational engineering of semiconductor nanowire systems.

In chapter 4, we demonstrated that user-defined changes to growth conditions permit the introduction of planar defects in Si nanowires.[2] Transverse TBs, which are rarely observed during Au-catalyzed Si nanowire growth, and SFs were rationally generated for the first time. Our data suggests that surface chemistry plays a role in the defect generation process. We determine a lower bound on the overall defect introduction efficiency between 60 and 65% and expect that judicious choice of catalysts and precursor species will improve this value. Rational selection of defect type (i.e. TB or SF), which still remains challenging in III-V nanowires, is not yet possible for Si nanowires and will require additional insight into defect introduction mechanism. We expect that these results will open new routes to engineer defect superstructure and materials properties in Si nanowires specifically, and all semiconductor nanowires in general.

On a similar subject, we showed that consecutive/multiple transverse TBs are possible in <111> oriented Si nanowires and that their spacing is controlled by sidewall morphology in Chapter 5.[3] As described in Chapter 4, the formation of first TB (TB_1) is driven by inward moving {111} facets that form following an abrupt increase in Si_2H_6 pressure and decrease of substrate temperature. However, another TB (TB_2) results from a different set of thin {111} facets that traverse the {110} sidewall. Both mechanisms, while distinct in their details, deform the triple-phase line and eventually favor TB nucleation. Detailed measurements of the sidewall show that {110} facet width determines TB_2 position and support the proposed model of nanowire morphology. Even though the introduction efficiency of TB_1 and TB_2 is still remained as low, we suggest that the stabilization of {111} facets (*i.e.* relative to {112}), possibly via surface functionalization or modification of catalyst droplet composition, will enable the fabrication of periodic defect superstructures similar to those seen in III-V nanowires.

In Chapter 6, we showed that Si nanowire kinking superstructures comprised of <112> segments exhibit a continuous TB that lies in the same plane as the superstructure. The presence of adsorbed hydrogen atoms only during <112> growth, in conjunction with the observation of multiple liquid-solid interface morphologies and TB elimination for <112> → <112> and <112> → <111> kinking, respectively, supports the importance of solid-vapor chemical bonding. Our data suggest that future attempts to engineer alternative, and simultaneously high fidelity, kinking superstructures should combine (1) novel chemistries, to favor different growth directions by modifying the force balance at the triple-phase line, and (2) a structural feature, for example a planar defect, to limit the number of nucleation points.

In overall, this study has shown the role of surface chemistry on the control of morphology and crystal structure of semiconductor nanowires. Our finding suggests that surface chemistry can explain various phenomena observed from VLS grown nanowire systems which have been remained as unclear. We also suggest further investigation on the surface functional groups other than hydrogen will enable the advanced engineering of nanowire structures in general, as several demonstrations using methyl groups (i.e. –

CH_3) have been made to control the kinking orientations and modulate the diameter of Ge nanowire system.[4,5]

7.2. References

1. Shin, N.; Filler, M.A. *Nano Lett.* **2012**, *12*, 2865-2870.
2. Shin, N.; Chi, M.; Howe, J. Y.; Filler, M. A. *Nano Lett*. **2013**, *13*, 1928-1933.
3. Shin, N.; Chi, M.; Filler, M. A. *ACS Nano* **2013**, *7*, 8206-8213.
4. Musin, I. R.; Filler, M. A. *Nano Lett*. **2012**, *12*, 3363-3368.
5. Musin, I. R.; Boyuk, D. S.; Filler, M. A. *J. Vac. Sci. Technol. B* **2013**, *31*, 020603.